UNIVERSITY OF CALIFORNIA, SAN DIEGO

Anisotropic Artificial Impedance Surfaces

A dissertation submitted in partial satisfaction of the requirements for the degree
Doctor of Philosophy

in

Electrical Engineering (Electronic Circuits and Systems)

by

Ryan Gordon Quarfoth

Committee in charge:

Professor Daniel F. Sievenpiper, Chair
Professor Eric E. Fullerton
Professor Vitaliy Lomakin
Professor Siavouche Nemat-Nasser
Professor Gabriel M. Rebeiz

2014

The Dissertation of Ryan Gordon Quarfoth is approved, and it is acceptable in quality and form for publication on microfilm and electronically:

_____

_____

_____

_____

_____
Chair

University of California, San Diego

2014

DEDICATION

To my parents Carin and Gary.

TABLE OF CONTENTS

LIST OF ABBREVIATIONS

FOM	Figure of merit
HFSS	High frequency simulation software
PEC	Perfect electric conductor
PMC	Perfect magnetic conductor
PML	Perfectly matched layer
SMA	Sub-miniature type-A
TE	Transverse electric
TM	Transverse magnetic
VNA	Vector network analyzer
Z	Impedance

LIST OF FIGURES

ACKNOWLEDGMENTS

I would first like to thank my advisor, Prof. Daniel Sievenpiper, for his guidance and insight throughout the entirety of my research. I feel lucky to have had the opportunity to work in his group, and my progress is testament to his vision, knowledge, patience, and support. I would like to thank my committee members, Prof. Eric Fullerton, Prof. Vitaliy Lomakin, Prof. Sia Nemat-Nasser, and Prof. Gabriel Rebeiz, for taking the time to be part of my committee and for their comments and suggestions. I would like to thank my parents, family, and friends, and especially everyone in the Applied Electromagnetics Group.

The material in this dissertation is based on the following papers which are either published, or under final process for publication.

Chapter 2 is based on and mostly a reprint of the following papers: R. Quarfoth, D. Sievenpiper, "Artificial Tensor Impedance Surface Waveguides", *IEEE Transactions on Antennas and Propagation*, vol. 61, no. 7, pp. 3597-3606 2013; R. Quarfoth, D. Sievenpiper, "Simulation of Anisotropic Artificial Impedance Surface with Rectangular and Diamond Lattices", *IEEE Antennas and Propagation Symposium Digest*, Spokane, WA, USA, pp. 1498-1501, July, 2011.

Chapter 3 is based on and mostly a reprint of the following paper: R. Quarfoth, D. Sievenpiper, "Broadband Unit Cell Design for Highly-Anisotropic Impedance Surfaces", *IEEE Transactions on Antennas and Propagation*, vol. 62, no. 8, pp. 1-10.

Chapter 4 is based on and mostly a reprint of the following papers: R. Quarfoth, D. Sievenpiper, "Non-scattering Waveguides Based on Tensor Impedance Surfaces", Submitted to *IEEE Transactions on Antennas and Propagation*; R. Quarfoth, D. Sievenpiper, "Artificial Tensor Impedance Surface Waveguides", *IEEE Transactions on Antennas and Propagation*, vol. 61, no. 7, pp. 3597-3606 2013.

Chapter 5 is based on and mostly a reprint of the following papers: R. Quarfoth, D. Sievenpiper, "Surface Wave Scattering Reduction Using Beam Shifters", *IEEE Antennas and Wireless Propagation Letters*, vol.13, pp. 963-966, 2014; R. Quarfoth, D. Sievenpiper, "Anisotropic Surface Impedance Cloak", *IEEE Antennas and Propagation*

Symposium Digest, Chicago, IL, USA, July 8-14, 2012.

The dissertation author was the primary author of the work in these chapters, and the coauthor (Prof. Daniel Sievenpiper) has approved the use of the material for this dissertation.

VITA

EDUCATION

2009	Bachelor of Science, Harvey Mudd College, Claremont, USA
2009 – 2014	Research Assistant, University of California, San Diego, USA
2011	Master of Science in Electrical Engineering, University of California, San Diego, USA
2014	Doctor of Philosophy in Electrical Engineering, University of California, San Diego, USA

PUBLICATIONS

R. Quarfoth, D. Sievenpiper, "Non-scattering Waveguides Based on Tensor Impedance Surfaces," Submitted to *IEEE Transactions on Antennas and Propagation*.

R. Quarfoth, D. Sievenpiper, "Broadband Unit Cell Design for Highly-Anisotropic Impedance Surfaces," *IEEE Transactions on Antennas and Propagation*, vol. 62, no. 8, pp. 1-10.

D. Gregoire, J. Colburn, A. Patel, R. Quarfoth, D. Sievenpiper, "An Electronically-Steerable Artificial Impedance Surface Antenna", IEEE Antennas and Propagation Symposium Digest, Memphis, TN, July 6-11, 2014.

R. Quarfoth, D. Sievenpiper, "Surface Wave Scattering Reduction Using Beam Shifters," *IEEE Antennas and Wireless Propagation Letters*, vol.13, pp. 963-966, 2014.

M. Huang, S. Yang, F. Gao, R. Quarfoth, D. Sievenpiper, "A 2-D Multibeam Half Maxwell Fish-Eye Lens Antenna Using High Impedance Surfaces," *Antennas and Wireless Propagation Letters, IEEE*, vol.13, pp. 365-368, 2014.

R. Quarfoth, D. Sievenpiper, "Artificial Tensor Impedance Surface Waveguides." *IEEE Transactions on Antennas and Propagation*, vol. 61, no. 7, pp. 3597-3606 2013.

R. Quarfoth, D. Sievenpiper, "Anisotropic Surface Impedance Cloak", *IEEE Antennas and Propagation Symposium Digest*, Chicago, IL, USA, July 8-14, 2012.

D. Sievenpiper, D. Dawson, M. Jacob, T. Kanar, S. Kim, J. Long, R. Quarfoth, "Experimental Validation of Performance Limits and Design Guidelines for Small Antennas", *IEEE Transactions on Antennas and Propagation*, vol. 60, no. 1, pp. 8-19,

January 2012.

R. Quarfoth, D. Sievenpiper, “Simulation of Anisotropic Artificial Impedance Surface with Rectangular and Diamond Lattices”, *IEEE Antennas and Propagation Symposium Digest*, Spokane, WA, USA, pp. 1498-1501, July, 2011.

R. Quarfoth, D. Sievenpiper, “Impedance Surface Waveguide Theory and Simulation”, *IEEE Antennas and Propagation Symposium Digest*, Spokane, WA, USA, pp. 1159-1162, July, 2011.

Md. Zakaria Quadir, Oday al-Buhamad, Kai D. Lau, Ryan Quarfoth, Lori Bassman, Paul R. Munroe, Michael Ferry, “The effect of initial microstructure and processing temperature on microstructure and texture in multilayered Al/Al(Sc) ARB sheets.” *Journal of Materials Research*, 100 (2009), p. 1705.

ABSTRACT OF THE DISSERTATION

Anisotropic Artificial Impedance Surfaces

by

Ryan Gordon Quarfoth

Doctor of Philosophy in Electrical Engineering (Electronic Circuits and Systems)

University of California, San Diego, 2014

Professor Daniel F. Sievenpiper, Chair

Anisotropic artificial impedance surfaces are a group of planar materials that can be modeled by the tensor impedance boundary condition. This boundary condition relates the electric and magnetic field components on a surface using a 2x2 tensor. The advantage of using the tensor impedance boundary condition, and by extension anisotropic artificial impedance surfaces, is that the method allows large and complex structures to be modeled quickly and accurately using a planar boundary condition.

This thesis presents the theory of anisotropic impedance surfaces and multiple applications. Anisotropic impedance surfaces are a generalization of scalar impedance

surfaces. Unlike the scalar version, anisotropic impedance surfaces have material properties that are dependent on the polarization and wave vector of electromagnetic radiation that interacts with the surface. This allows anisotropic impedance surfaces to be used for applications that scalar surfaces cannot achieve. Three of these applications are presented in this thesis. The first is an anisotropic surface wave waveguide which allows propagation in one direction, but passes radiation in the orthogonal direction without reflection. The second application is a surface wave beam shifter which splits a surface wave beam in two directions and reduces the scattering from an object placed on the surface. The third application is a patterned surface which can alter the scattered radiation pattern of a rectangular shape.

For each application, anisotropic impedance surfaces are constructed using periodic unit cells. These unit cells are designed to give the desired surface impedance characteristics by modifying a patterned metallic patch on a grounded dielectric substrate. Multiple unit cell geometries are analyzed in order to find the setup with the best performance in terms of impedance characteristics and frequency bandwidth.

Chapter 1 Introduction

Antennas have become a ubiquitous component of modern technology. Many consumer electronic devices now include multiple antennas for communication at different frequencies and for different protocols. Airplanes, ships, and various military platforms use antennas for radar, imaging, communication, and multiple other technologies. In all of these systems, antennas are often placed near other conductive objects and electronics, and also near other antennas. In order for these systems to work optimally, the currents generated on and near antennas must be controlled in order to maintain antenna patterns, prevent damage to electronics, and scatter radiation in the desired directions. These surface currents can be manipulated using impedance surfaces that control the propagation of surface waves.

1.1 Surface Waves

Surface waves are an electromagnetic wave mode that propagate bound to a surface. They can be excited by antennas or due to external radiation, and the field is peak on the surface and decays exponentially away from the surface. Surface waves can be excited on the planar region between two dielectrics as shown in Figure 1.1. Each material extends infinitely in the *y* direction, and the surface wave can propagate in any direction on the YZ plane. The fields decay exponentially away from the boundary in both the positive and negative *x* direction. The decay has a different rate in each material due to the different material properties.

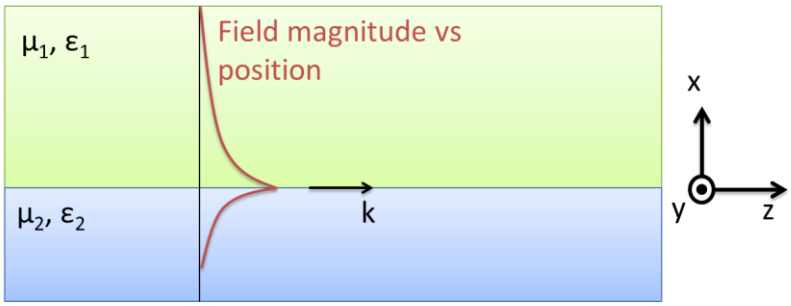

Figure 1.1: Surface wave mode on the boundary between dielectrics.

Grounded dielectric structures also support surface waves as illustrated in Figure 1.2. A thin substrate with thickness much less than the wavelength is placed above a ground plane. Above the substrate is vacuum. In this setup there is still exponential field decay above the substrate. The field varies sinusoidally within the substrate and multiple modes are supported depending on the order of this variation. The grounded dielectric supports surface wave modes down to zero-frequency. This affects multiple microwave structures including patch antennas, microstrip lines and printed circuits where surface waves generally degrade performance.

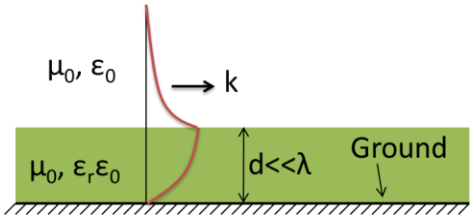

Figure 1.2: Surface wave mode on grounded dielectric slab.

An illustration of the degradation of the radiation pattern of a patch antenna is shown in Figure 1.3. A patch antenna can be constructed by placing a square or rectangular patch above a grounded dielectric slab. The main radiation lobe is normal to the patch. However, the structure will also excite surface waves in the dielectric substrate. These surface waves propagate away from the patch and can radiate at the edge of the substrate or at other discontinuities. This radiation can interfere with and degrade the desired radiation pattern of the patch. This interference can potentially be mitigated by patterning the substrate using impedance surfaces to control the

propagation of surface waves on the dielectric. Other antennas or components that are integrated to dielectric substrates such as microstrip lines or printed antennas can also be negatively affected by this phenomenon.

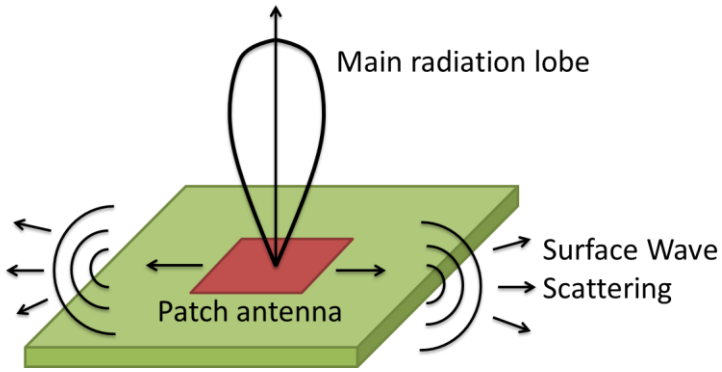

Figure 1.3: Surface waves excited on substrate near a patch antenna.

1.2 Impedance Surfaces

An impedance surface is an electromagnetic boundary condition that relates the electric and magnetic fields on a surface. Impedance surfaces are useful because they allow the simplification of nearly-planar structures whose thicknesses are small as compared to the wavelength. In Figure 1.4 an illustration is shown of a grounded dielectric slab which is modeled as an impedance surface.

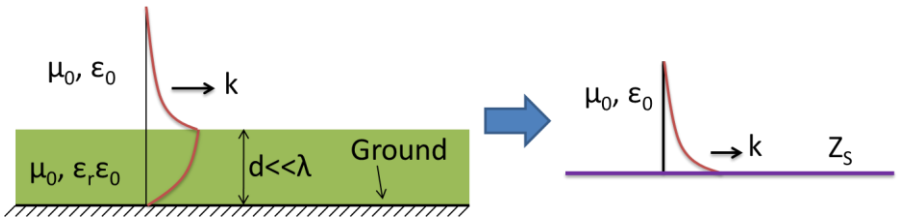

Figure 1.4: Grounded dielectric slab modeled as an impedance surface.

The slab, which has thickness *d*, is modeled instead by a planar boundary condition with a scalar impedance defined as Z_S. Isotropic surfaces have scalar surface impedance. The rate of field decay above the impedance boundary is the same as the decay above the grounded dielectric slab. Similarly, the phase velocity and group

velocity of surface waves on the impedance boundary are the same as those propagating within the dielectric slab. These similarities are what allow the grounded slab to be modeled more simply as an impedance boundary. More complicated structures can also be modeled in this manner and these are discussed further in Section 2.3 and Section 3.3. The advantage of this simplification is that it allows large structures to be accurately-modeled efficiently.

The surface impedance relates the electric and magnetic fields that are tangential to the surface. The surface impedance is a complex number whose real part represents loss. Therefore, lossless surfaces are purely reactive. Isotropic surfaces have the same surface properties for a wave traveling in any direction along the surface. Anisotropic surfaces have direction-dependent properties, and their properties are discussed in-depth in Section 2.2. The polarization of electric and magnetic fields is dependent on the type of surface mode. Transverse magnetic (TM) and transverse electric (TE) modes are both supported. The surface impedance of each of these modes is defined below.

$$Z_{S,TM} = \frac{E_{propagating}}{H_{transverse}}, \tag{1.1}$$

$$Z_{S,TE} = \frac{E_{transverse}}{H_{propagating}}. \tag{1.2}$$

TM modes have electric field in the propagating direction and magnetic field in the transverse direction. The reactance is positive for TM modes, and surfaces that support TM modes are sometimes called inductive. Conversely, TE modes have magnetic field in the propagating direction and electric field in the transverse direction. TE modes have negative reactance, and surfaces that support TE modes can be called capacitive. The TM mode is supported by grounded dielectric slabs (and other similar structures) down to zero-frequency. This is the mode that is predominantly used in this thesis. Depending on the structure of the material, multiple TM or TE modes can be supported simultaneously or at different frequencies. Along with TM and TE modes, anisotropic surfaces support hybrid modes which are a combination of both TM and TE. These hybrid modes are discussed in Section 2.2.

1.3 Applications

There are multiple applications for impedance surfaces which control surface wave propagation. As discussed in Section 1.1 and illustrated in Figure 1.3, impedance surfaces can be used to minimize the negative effects of surface waves on antennas. Impedance surfaces can also be used to alter the scattering characteristics of objects. An illustration of this is shown in Figure 1.5. Objects can have complicated scattering patterns of incident radiation due to their shapes. By patterning the exterior of the object with impedance surfaces, the scattering characteristics can be altered to a more desired pattern.

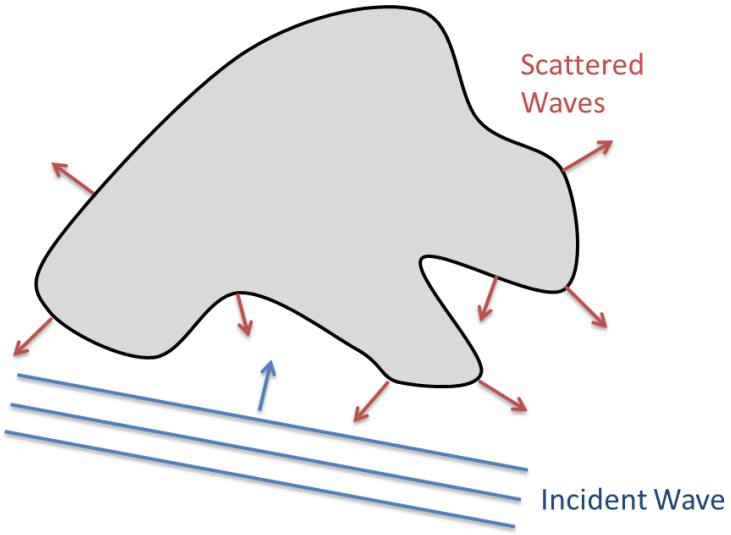

Figure 1.5: Objects scatter incident waves in many directions.

Surface waves can also be used to create antennas. Surface wave modes that are leaky do not propagate losslessly and instead radiate power away from the surface. Leaky wave antennas have been created by periodically modulating the surface impedance. This creates an effect similar to a diffraction grating and these antennas are also known as holographic antennas. In this thesis, multiple other applications will also be discussed including waveguides, beam shifters and splitters, and plane wave scattering. These applications, along with the rest of the thesis, are summarized in Section 1.4.

1.4 Scope of thesis

The thesis presents on details from multiple projects, with the common theme of anisotropic artificial impedance surfaces.

Chapter 2 covers background information on the fundamentals of anisotropic impedance surfaces. The mathematical description of impedance surfaces is first presented. This is followed by a discussion of periodic unit cells, which are used to create impedance surfaces. A description of the simulation method used to analyze the material properties of the unit cells is also presented.

Chapter 3 investigates of the properties of multiple unit cell geometries. The ring-mushroom unit cell geometry is found to have best performance in terms of bandwidth and impedance range. The effect of substrate height and permittivity on performance is also discussed.

Chapter 4 presents anisotropic surface impedance waveguides. In the first section, a theoretical analysis of the dispersion in these waveguides is discussed. A transparent waveguide application is also proposed and simulated. In the second section this transparent waveguide is fabricated in both straight and bent setups.

Chapter 5 studies a surface wave beam splitter. The device is created using two adjacent beam splitters which are transformation electromagnetic devices. The structure is fabricated and measured, and it is shown that it can reduce the scattering of surface waves from an object placed on a surface.

Chapter 6 demonstrates a structure that can be used to alter the scattering of plane waves from an object. An incident plane wave has a characteristic pattern of scattering when incident on a rectangular object. This pattern is altered by patterning a ground plane on top and bottom using anisotropic impedance surfaces. Measured results show that the effect can be achieved over a large bandwidth.

Chapter 2 Surface Waves on Anisotropic Impedance Surfaces

2.1 Overview

Artificial impedance surfaces are engineered, electrically-thin materials which can support surface waves in bound or leaky modes. Isotropic impedance surfaces have a scalar relation between the electric and magnetic fields tangent to the surface, and have the same properties for surface waves traveling in any direction. Isotropic impedance surfaces have been designed for various applications including a linear leaky wave antenna [1], spiral leaky wave antenna [2], Luneburg lens antenna [3, 4], and impedance surface waveguides [5]. Tensor impedance surfaces are a generalization of isotropic impedance surfaces where the relation between electric and magnetic field is a 2×2 tensor. Guided surface waves on tensor impedance surfaces have been characterized analytically [6]. A tensor impedance surface was used to make a circularly polarized antenna from a linear feed [7], and a circularly polarized isoflux antenna [8]. Tensor impedance surfaces were also used as a liner to create a hybrid-mode horn antenna [9, 10]. Metasurfaces have been used to create mantle cloaks by scattering cancellation [11-13]. Tensor surface impedance waveguides [5, 14] and a surface wave cloak using beam shifters [15] have also been studied on ideal boundary conditions.

In every experimental implementation mentioned above, a periodic unit cell was used to achieve the desired surface impedance properties. The size and thickness of the unit cell must be small as compared to the wavelength (generally around $\lambda/10$). Unlike constitutive properties such as permittivity and permeability which are effects of the atomic structure of a material, impedance surfaces and other metasurfaces derive effective material properties from macroscopic periodic inclusions that are artificially

added to a material [16]. Impedance surfaces can be created in many ways such as grounded dielectric slabs (e.g. [17]), corrugated surfaces [18, 19], pin-bed structures [20, 21], bump lattices [22], and variable dielectric height [23-25]. Currently the most common method to create impedance surfaces at microwave frequencies is with printed circuit boards. Printed circuit boards are popular because they have an established industry that provides quick manufacturing and low prices as compared to custom made materials. Printed circuit fabrication can include dielectric with planar metallic inclusions created by etching, and drilled, plated metal vias. Multi-layer structures can also be fabricated and a wide variety of substrates can be used. In this study, for simplicity, we limit the impedance surface design to a grounded dielectric with an etched top layer and plated vias. The design of printed circuit materials is limited by the manufacturing capabilities of the fabrication companies. These capabilities define minimum spacing of metal patches, and the minimum diameter of vias. Each design discussed in this paper can be manufactured using standard materials and processes.

Previous work has shown that a grounded dielectric slab with a printed anisotropic metal pattern on the top layer can be accurately modeled as an anisotropic impedance surface [7]. However, analysis has also shown that there are conditions where a grounded dielectric substrate with an anisotropic capacitive impedance deviates from the standard tensor impedance boundary condition [26, 27]. This analysis is only for printed circuit tensor impedance surfaces with no vias. Multiple other variations of printed circuit structures have also been studied. Un-patterned grounded dielectric slabs support surface waves from DC up to high microwave frequencies. Mushroom unit cells were shown to both suppress surface waves over a bandgap region and also reflect incident plane waves in phase [28]. Tunable, varactor diode loaded structures [29, 30], and reactively loaded vias [31] have also been studied. Lumped additions to the unit cell have not been considered in this study, although these components could potentially increase anisotropy or improve bandwidth and are a possible topic for future research.

This chapter presents the fundamental characteristics of impedance surfaces. Section 2.2 covers the mathematical background of tensor impedance surfaces. Section 2.3 introduces periodic unit cells which are used to realize impedance surfaces. Section

2.4 explains the methods used to analyze the unit cells and determine their material properties. Section 2.5 presents a simple study of the properties of rectangular and diamond unit cells.

2.2 Artificial Tensor Impedance Surfaces

Isotropic impedance surfaces have a single scalar parameter, Z_S, which relates the electric and magnetic fields as described by (1.1) and (1.2). Anisotropic impedance surfaces have direction-dependent impedance properties and must instead be modeled by a 2×2 tensor. For a surface on the X-Y plane, the tensor impedance matrix can be defined in general as

$$\mathbf{Z} = \begin{bmatrix} Z_{xx} & Z_{xy} \\ Z_{yx} & Z_{yy} \end{bmatrix}. \tag{2.1}$$

In this study we assume lossless, reciprocal surfaces where all tensor values must be pure imaginary and $Z_{xy} = Z_{yx}$ [21]. The boundary condition for the fields on the surface is defined as [1]:

$$\mathbf{E} = \overline{\overline{\mathbf{Z}}}.\hat{\mathbf{z}} \times \mathbf{H} = \overline{\overline{\mathbf{Z}}}.\mathbf{J}\,. \tag{2.2}$$

We can expand (2.2) to get a relation for the surface field components

$$\begin{bmatrix} E_x \\ E_y \end{bmatrix} = \begin{bmatrix} Z_{xx} & Z_{xy} \\ Z_{xy} & Z_{yy} \end{bmatrix} \begin{bmatrix} -H_y \\ H_x \end{bmatrix}. \tag{2.3}$$

Unlike scalar impedance surfaces which support pure TM waves, tensor surfaces support hybrid waves that contain both TM and TE field components. The TM and TE modes are transverse with respect to the direction of propagation. For a TM-like mode, both eigenvalues of the impedance tensor are inductive, the electric and magnetic fields can be split into their components as [7]

$$E = (1-\gamma)E_{TM} + j\gamma E_{TE}\,, \tag{2.4}$$

$$H = (1-\gamma)H_{TM} + j\gamma H_{TE}\,. \tag{2.5}$$

For the TM-like mode γ is the fraction of the TE field component in the wave and is less than 0.5 (at γ=0.5 there would be equal TM and TE power in the mode). Substituting (2.4) and (2.5) into (2.3) gives [7]

$$Z_0\begin{bmatrix} -j(1-\gamma)\dfrac{\alpha_z}{k_0}\cos\theta - j\gamma\sin\theta \\ -j(1-\gamma)\dfrac{\alpha_z}{k_0}\sin\theta + j\gamma\cos\theta \end{bmatrix} = \begin{bmatrix} Z_{xx} & Z_{xy} \\ Z_{xy} & Z_{yy} \end{bmatrix}\begin{bmatrix} -(1-\gamma)\cos\theta + \gamma\dfrac{\alpha_z}{k_0}\sin\theta \\ -(1-\gamma)\sin\theta - \gamma\dfrac{\alpha_z}{k_0}\cos\theta \end{bmatrix}, \quad (2.6)$$

where k_0 is the wave number in the medium, α_z is decay constant of the wave attenuating above the surface, Z_0 is the impedance of free space, and θ is the direction of wave propagation with respect to the X-axis. Assuming the values of the impedance tensor are known, we can solve (2.6) for α_z/k_0 and γ to get [7]

$$\begin{aligned} \frac{\alpha_z}{k_0} = \Big[& -j\left(Z_0^2 - Z_{xy}^2 + Z_{xx}Z_{yy}\right) \pm \Big\{ -\left(Z_0^2 - Z_{xy}^2 + Z_{xx}Z_{yy}\right)^2 + \\ & 4Z_0^2 \times \left(Z_{yy}\cos^2\theta - Z_{xy}\sin 2\theta + Z_{xx}\sin^2\theta\right) \\ & \times \left(Z_{xx}\cos^2\theta + Z_{xy}\sin 2\theta + Z_{yy}\sin^2\theta\right)\Big\}^{1/2}\Big] \\ & \times \left[2Z_0\left(Z_{yy}\cos^2\theta - Z_{xy}\sin 2\theta + Z_{xx}\sin^2\theta\right)\right]^{-1} \end{aligned}, \quad (2.7)$$

and

$$\begin{aligned} \gamma = \Big[& Z_0^2 + Z_{xy}^2 - Z_{xx}Z_{yy} + jZ_0\left(2Z_{xy}\cos 2\theta + \left(Z_{yy} - Z_{xx}\right)\sin 2\theta\right) \pm 2^{-1/2}\Big\{2Z_0^4 - Z_0^2\left(Z_{xx} + Z_{yy}\right)^2 \\ & + 2\left(Z_{xy}^2 - Z_{xx}Z_{yy}\right)^2 + 4Z_0^2 Z_{xy}\left(Z_{xx} - Z_{yy}\right)\sin 4\theta + Z_0^2\cos 4\theta\left(-4Z_{xy}^2 + \left(Z_{xx} - Z_{yy}\right)^2\right)\Big\}^{1/2}\Big] \\ & \times \left[2\left(Z_0^2 + Z_{xy}^2 - Z_{xx}Z_{yy}\right)\right]^{-1} \end{aligned}. \quad (2.8)$$

In each case, the negative sign corresponds to a TM-like mode and the positive sign to a TE-like mode. The α_z/k_0 ratio gives a normalized, θ-dependent, effective scalar surface impedance value for a tensor surface. For a TM-like mode the effective scalar surface impedance can be written as

$$Z(\theta) = jZ_0\frac{\alpha_z(\theta)}{k_0}. \quad (2.9)$$

From (2.9), we have obtained a scalar value from the impedance tensor that represents the effective impedance of a wave propagating in the θ-direction. A wave on an isotropic TM surface with this impedance will have the same phase velocity and field decay above the surface as a wave on the tensor surface. A plot of the effective scalar impedance $Z(\theta)$ is shown in Figure 2.1. The effective scalar impedance plot forms a peanut shape except at the isotropic limit where it becomes circular. For a tensor with Z_{xy}=0, the maximum and minimum effective scalar impedance values are oriented along

the *x*- and *y*- axes (as displayed in Figure 2.1).

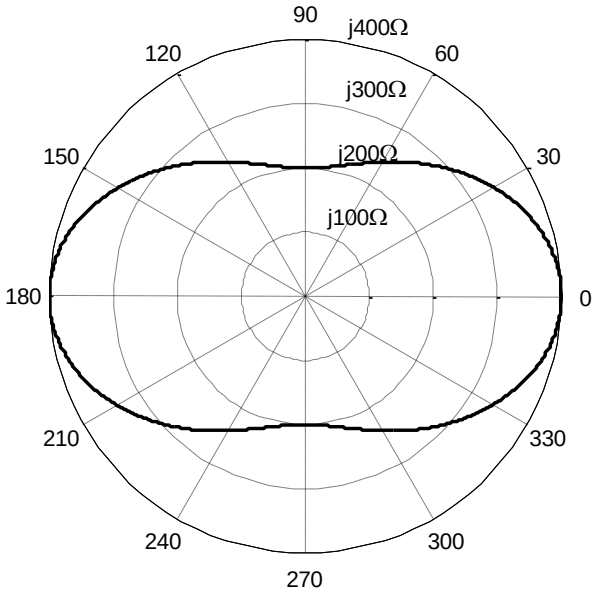

Figure 2.1: Effective scalar impedance vs. propagation direction. In this case the impedance tensor has values Zxx=j400Ω, Zxy=0, Zyy=j200Ω.

In general the magnitude and direction of the principal axes correspond to the eigenvalues and eigenvectors of the impedance tensor. The eigenvectors are always orthogonal and the peanut shape is symmetric across the two axes formed by the eigenvectors. Figure 2.2 shows a plot of γ as a function of propagation direction. For a lossless, reciprocal tensor surface, γ is purely real. Along the principal axes of the impedance tensor γ=0, and γ is maximized 45° away from the principle axes. Impedance tensors with larger amounts of anisotropy will have larger γ values. For an isotropic surface, γ=0 at all rotation angles. In the limit as Z_{xx} goes to j∞Ω and Z_{yy} goes to zero, γ=0.5 at all rotation angles

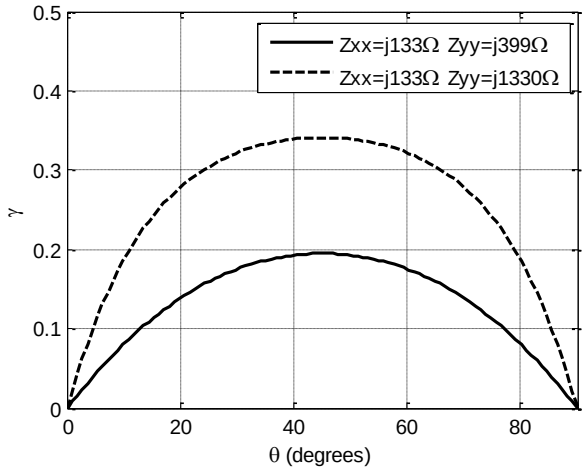

Figure 2.2: The fraction of the mode that is TE, γ, vs. propagation direction. For a lossless, reciprocal tensor impedance γ is real. In both lines plotted Zxy=0 which causes principal axes of the axes of the impedance tensor to be aligned with the X and Y axes, and γ=0 at θ=0° and θ=90°.

The effective refractive index can also be expressed with respect to propagation direction by relating it to the wave vector components or the surface impedance. The wave vector components are related as follows

$$k_x^2 + k_y^2 - \alpha_z^2 = k_0^2 . \tag{2.10}$$

For inductive surfaces, the index can be solved in two forms using equations (2.9) and (2.10):

$$n(\theta) = \frac{\beta}{k_0} = \sqrt{1 + \left(\frac{\alpha_z}{k_0}\right)^2} = \sqrt{1 - \frac{Z(\theta)^2}{Z_0^2}} , \tag{2.11}$$

where β is the propagating wavenumber: $\beta^2 = k_x^2 + k_y^2$. The index is greater than one for any inductive impedance. Figure 2.3 shows that the index is nearly elliptical for a tensor with principal indices of n_x=1.46 and n_y=1.03 (values that are realistically achievable). For a tensor with Z_{xy}=0 (as shown in Figure 2.1 and Fig. Figure 2.3), the simplified elliptical index is defined as:

$$n(\theta) = \sqrt{\frac{1}{\frac{\cos^2\theta}{n_x^2} + \frac{\sin^2\theta}{n_y^2}}} , \tag{2.12}$$

where n_x and n_y are calculated from (2.11) by replacing $Z(\theta)$ with Z_{xx} and Z_{yy} respectively. We defined this approximate elliptical index such that the index value matches (2.11) exactly along the principal directions of the tensor but assumes elliptical variation at intermediate angles. For larger surface indices, n>5, the effective surface index can deviate 5% or more from the elliptical shape and become peanut-like. However, this corresponds to an impedance Z>1,845Ω, which is quite large and hard to achieve with simple printed circuit structures.

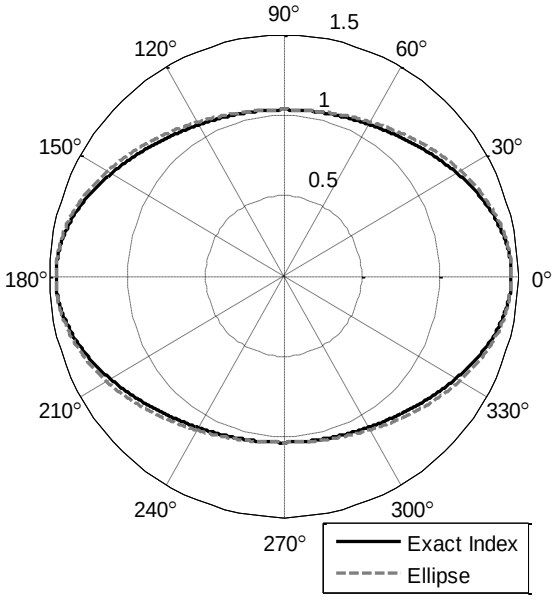

Figure 2.3: Index of refraction vs. propagation direction. In this case the corresponding impedance tensor has values Zxx=j400Ω, Zxy=0, Zyy=j100Ω. The principal index values are nx=1.46 and ny=1.03 at 0° and 90° respectively. An ellipse with these same principal values is also plotted.

2.3 Periodic Unit Cells and Dispersion

Impedance surfaces can be created by patterning periodic inclusions into a material [16]. Planar artificial materials can be called metasurfaces more generally. Printed circuit structures are commonly used because of the ease of fabrication of these materials. Previous studies have investigated the patterning of metal patches on a grounded dielectric substrate [7]. Isotropic impedance surfaces have been created using

square or hexagonal metal patches [28]. Creating anisotropic impedance surfaces requires some anisotropy of the unit cell shape. Examples of unit cells for anisotropic impedance surfaces are shown in Figure 2.4.

Figure 2.4: Unit cell examples. A square unit cell with a slit is shown on the left. Three different unit cells with two symmetry planes are shown on the right.

The anisotropic impedance can be represented as a 2×2 impedance tensor that has three independent terms (off-diagonal terms are equal) as shown in (2.3). Ideally a unit cell geometry can be constructed where each of the three independent terms in the tensor correspond to a specific geometrical parameter of the cell. The eigenvalues of this tensor give the maximum and minimum impedance values, and the eigenvectors give the direction of these values. To ensure that eigenvector directions match the lattice direction, unit cells must be chosen with two orthogonal mirror symmetry planes as shown in Figure 2.4. Because of a lack of symmetry, a square lattice geometry with a slit will not have equivalence between the slit angle and the major axis of the impedance tensor. When using symmetric cell types, the three independent impedance variables could be the cell length in each orthogonal direction and the cell rotation. Preferably the impedance along either of the orthogonal directions is only a function of the cell geometry in that direction. Properties of rectangular and diamond unit cells are analyzed in Section 2.4. Further analysis of unit cell geometries is performed in 0.

2.4 Eigenmode Simulation Method

Ansys HFSS is a commercial full-wave electromagnetic solver that was used for all simulations in this thesis. HFSS has multiple solvers which can be used for different

problems. Using the eigenmode solver, a single unit cell can be drawn and a solution is found for a mode propagating on an infinite lattice of this unit cell. In this section, the HFSS simulation setup is discussed. The properties of rectangular and diamond unit cells are simulated, and the results are presented in Section 2.5.

A series of aspect ratios for rectangular and diamond cell geometries were simulated using Ansoft HFSS software. In each case the dielectric simulated was Rogers RT/duroid 5880 (ε_r=2.2) with a thickness of 1.575mm. A vacuum of height 15mm was placed above the dielectric. In other studies, the vacuum height was chosen to be taller so that results at lower frequencies were more accurate. A metal patch was simulated using a perfect electric boundary condition, and a perfect electric boundary was also used on the top and bottom of the structure. The perfect electric boundary on the top was found to give equivalent results to the perfectly matched layer (PML) boundary. The PML boundary was not used because of longer solution times and less stable results. He PEC boundary is valid at the top of the structure as long as the surface mode has decayed sufficiently. A radiation boundary cannot be used with the eigenmode simulator. A gap of 0.4mm was implemented between the patch and the edge of the unit cell. An infinite lattice was solved using master-slave boundaries in the built-in eigenmode solver in HFSS.

Figure 2.5 shows a simulation structure for a diamond unit cell shape. By applying master-slave boundaries to the sets of parallel walls, an effective phase delay exists across the structure. Based on the distance between the walls, this phase delay corresponds to a wavelength. For rectangular structures, the delay is set only on one set of walls and the perpendicular walls have a delay of zero. For the diamond structure, both sets of parallel walls are assigned an equal (or opposite) delay. This defines a wave traveling in a tip to tip direction along the diamond. In the diamond case, the wavenumber is obtained based on the delay, the propagating length, and the angle of the diamond at the tip. The eigenmode solution gives the mode frequencies that satisfy the boundary conditions. We chose to solve for the first five modes of the structures. The results can be plotted as a dispersion curve as the delay value is swept.

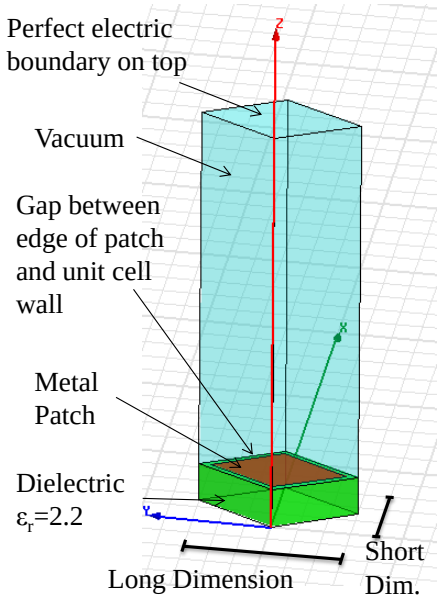

Figure 2.5: Example of simulation setup for diamond unit cell.

2.5 Rectangular and Diamond Unit Cell Results

2.5.1 Rectangular Cell

A series of rectangular unit cell geometries were tested. In each case, the length of the structure in the propagating direction was 6mm. The transverse length was varied to determine whether the non-propagating lattice dimension affects propagation. Figure 2.6 shows that the transverse length has a negligible effect on the dispersion characteristics of the structure. Each of the six cell sizes plotted has nearly identical values.

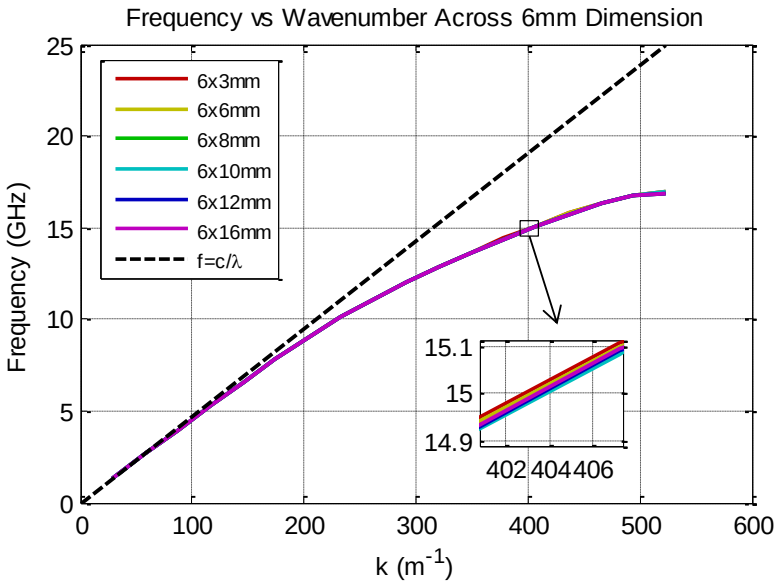

Figure 2.6: Dispersion of rectangular unit cells. Frequency vs. wavenumber for unit cells of constant propagating length and varying transverse length.

For TM surface waves, the impedance can be obtained from the dispersion relation as follows:

$$Z_{TM} = Z_0 \sqrt{1 - \left(\frac{k_{TM}}{k_0} \right)^2} \quad . \tag{2.13}$$

The reactance vs. frequency relation for each unit cell dimension is plotted in Figure 2.7. Since the dispersion relation showed negligible variation of properties based on transverse unit cell length, we get the expected result that the impedance characteristics do not vary with transverse unit cell length. This is important for patterning where setting the impedance independently in either direction significantly lowers the difficulty of making complex patterns.

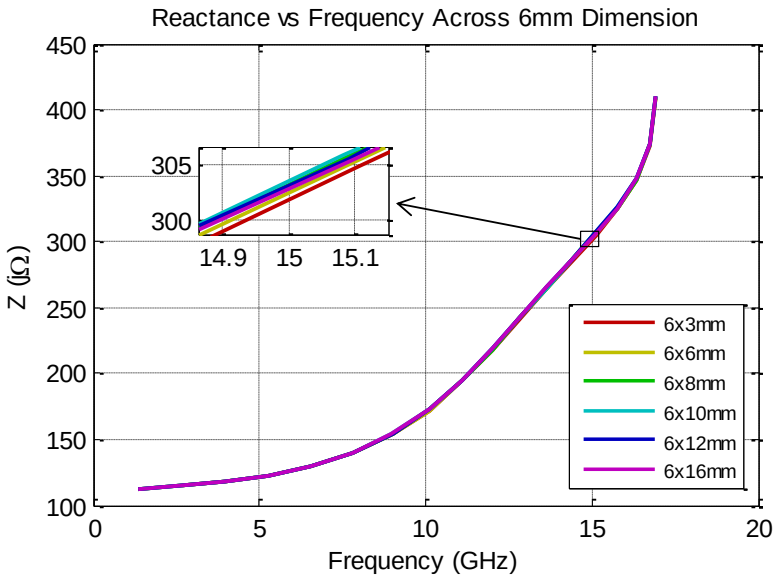

Figure 2.7: Reactance vs. frequency for rectangular unit cells. The unit cells have constant propagating length and varying transverse length.

2.5.2 Diamond Cell

A series of diamond-shaped unit cells were simulated for a propagating length of 6mm. In this case, 6mm corresponds to the tip-to-tip length of the diamond cell. Since the rectangular cells were defined by their side lengths, this convention implies that a 6x6mm diamond cell has the same area as a $3\sqrt{2}\times 3\sqrt{2}$mm square cell. Figure 2.8 shows the dispersion relation for each of the diamond cells along with the corresponding rectangular cell. For low k values the cells have similar characteristics. For high k values, the unit cells have diverging values.

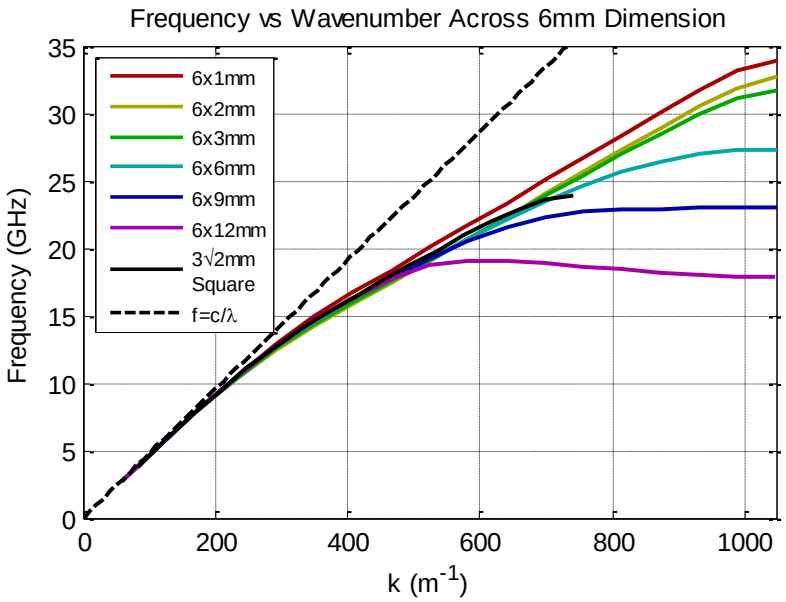

Figure 2.8: Frequency vs. wavenumber for diamond unit cells. The unit cells have constant propagating length and varying inverse length.

Figure 2.9 shows the reactance vs. frequency relation of the diamond cells. For the cells where the propagating dimension is longer than the transverse dimension we have similar impedance ranges and shapes. For cells where the propagating dimension is shorter than the transverse dimension, the impedance increases significantly at the highest frequencies. We can see in the 12×6mm cell that the dispersion relation has a negative slope for k from approximately 600 m^{-1} to 1050 m^{-1}. Theoretical regions with negative slope are often difficult to access experimentally, so the structure may not be useful in this range. In Figure 2.9 we can see that the impedance rapidly rises at the onset of the negative slope. The start of this rapid impedance increase corresponds to a value of approximately $Z=400j\Omega$ which is the same maximum value of the square or long-dimension diamond lattices. Thus, both structures have roughly the same useful impedance range, but the rectangular structure has the added advantage that impedance is independent of the transverse cell length.

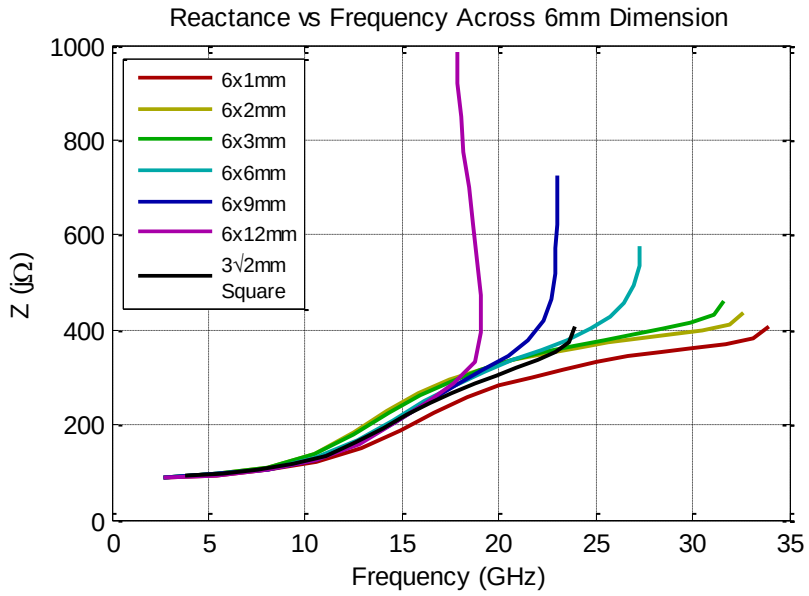

Figure 2.9: Reactance vs. frequency for diamond unit cells. The unit cells have constant propagating length and varying transverse length.

2.5.3 Variation of Lattice Length in Propagation Direction

The propagating unit cell dimension was varied to determine the effect it has on the impedance of the unit cell. The results of 14 rectangular unit cell simulations are shown in Figure 2.10. In all of the labels, the first value is the propagating length in mm, and the second value is the transverse length in mm. Multiple curves are not visible in the plot because they are blocked by another simulation that has an equal unit cell length in the direction of propagation. In every case, the impedance range is from 100jΩ to 400jΩ. The increase in unit cell length keeps a (somewhat) similar reactance vs. frequency shape, but with a reduced frequency range. For a single frequency, the increase in propagating length corresponds to an increase in reactance.

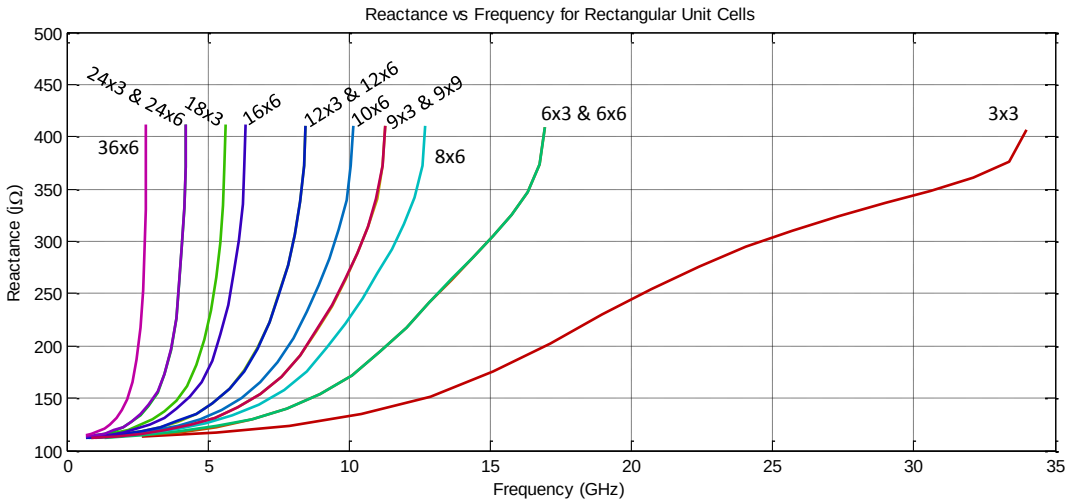

Figure 2.10: Reactance vs. frequency for multiple rectangular unit cell sizes. All dimensions are in mm. The first value is the length of the propagating dimension, and the second value is the length of the transverse dimension.

2.6 Conclusion

This chapter has presented the fundamental characteristics of anisotropic impedance surfaces. This has included the mathematical formulation of impedance surfaces, their physical realization using periodic structures, and the simulation method for analyzing unit cells.

Chapter 2 is based on and mostly a reprint of the following papers: R. Quarfoth, D. Sievenpiper, "Artificial Tensor Impedance Surface Waveguides", *IEEE Transactions on Antennas and Propagation*, vol. 61, no. 7, pp. 3597-3606 2013; R. Quarfoth, D. Sievenpiper, "Simulation of Anisotropic Artificial Impedance Surface with Rectangular and Diamond Lattices", *IEEE Antennas and Propagation Symposium Digest*, Spokane, WA, USA, pp. 1498-1501, July, 2011.

Chapter 3 Broadband Unit Cell for Highly-Anisotropic Impedance Surfaces

3.1 Overview

Impedance surfaces are built from periodic unit cells as described in Section 2.3. Isotropic impedance surfaces generally use square or hexagonal unit cells with patches that have this same shape. In order to create an anisotropic impedance surface, the unit cell must have some anisotropy. Unlike isotropic which only support pure TM and TE modes, anisotropic surface support hybrid modes. It is found that when multiple modes are supported at the same frequency these hybrid modes interfere with each other, and the unit cell can no longer be used. In this chapter, multiple unit cell geometries are analyzed to find which design has the best performance. The performance is quantified using a figure of merit that accounts for both frequency bandwidth and the magnitude of anisotropy.

3.2 Anisotropic Unit Cell Theory

3.2.1 Tensor Impedance Surfaces

The tensor impedance boundary condition specifies the field relation for a lossless reciprocal impedance surface in the XY plane as described by (2.3). the impedance tensor is a 2×2 matrix, and for a TM-like mode, all four values are purely imaginary, the diagonal terms are inductive, and the off-diagonal terms are equal [7, 32]. Tensor impedance surfaces support hybrid modes that are mixtures of TM and TE components. The fundamental mode on inductive surfaces is called “TM-Like” because the TM component accounts for a majority of the wave power (an equivalent TE-like

mode also exists) [7]. The proportion of TM and TE components in a TM-Like mode is dependent on the direction of propagation of the wave. In the principal directions of the impedance tensor the TM-Like mode is purely TM and has no TE component. If the XY coordinate system is aligned with these principal axes, the tensor will have no off-diagonal terms in this coordinate system, and the impedance can be written without loss of generality as follows:

$$\mathbf{Z} = \begin{bmatrix} Z_{xx}(\omega) & 0 \\ 0 & Z_{yy}(\omega) \end{bmatrix}, \tag{3.1}$$

where the impedance is explicitly defined to be frequency dependent. In this coordinate system, a wave traveling in the *x*- or *y*-direction will have an effective impedance of Z_{xx} or Z_{yy} respectively. Z_{xy} is 0 since we have aligned the XY coordinate system with the principal axis of the impedance tensor. At intermediate angles the impedance for TM-like modes is defined by (3.2) and will be some value between Z_{xx} and Z_{yy} [7]:

$$Z(\theta) = jZ_0 \frac{\alpha_z(\theta)}{k_0}, \tag{3.2}$$

where α_z is the exponential field decay of the mode above the surface as defined by (2.7). A wave traveling on this anisotropic surface in the direction defined by θ will have the same phase velocity and field decay as a wave on the scalar surface with an impedance specified by (3.2). Real unit cells, along with being dispersive, deviate from the theoretical impedance profile. In [26, 27], this discrepancy was characterized for structures with no via. In this study we verify that bounded surface waves are supported for any propagation direction, but accept that there will be some deviation from the ideal theory.

3.2.2 Ideal Unit Cell Dispersion

Figure 3.1 shows an example of surface impedance dispersion where the *x*-direction has high impedance and the *y*-direction has low impedance: $Z_{xx}(\omega) > Z_{yy}(\omega)$. Three intermediate angles are also plotted which represent surface waves traveling between the *x*- and *y*-directions. At any given frequency, the effective surface impedance varies gradually from Z_{xx} to Z_{yy}. Real impedance surfaces generally have

minimal anisotropy at low frequencies where impedance is also very small. As frequency increases, the magnitude of the impedance and the level of anisotropy both increase.

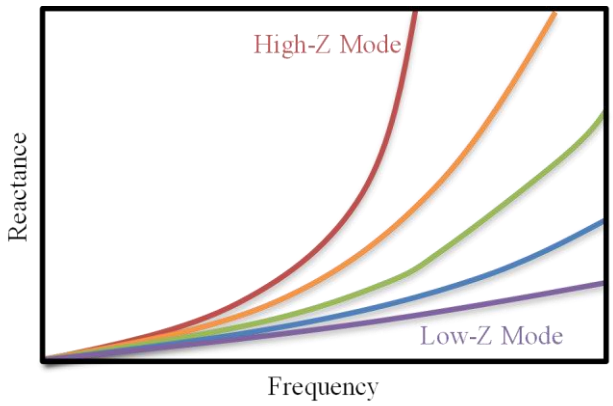

Figure 3.1: Impedance dispersion for an ideal tensor impedance surface. Each curve represents the expected impedance dispersion relation for propagation of a surface wave mode in a different direction. The high and low impedance modes propagate in orthogonal directions. At intermediate directions the impedance will gradually shift from the low to the high impedance value.

The wavenumber for a TM-like mode can be solved from the surface impedance as follows [28]:

$$k_{TM} = \frac{\omega}{c}\sqrt{1-\frac{Z^2}{Z_0^2}}, \tag{3.3}$$

where Z_0 is the impedance of free space. An example of an expected dispersion plot for a tensor impedance surface is shown in Figure 3.2. Under certain conditions, real unit cells do not have the correct directionally dependent dispersion and cannot be used as impedance surfaces.

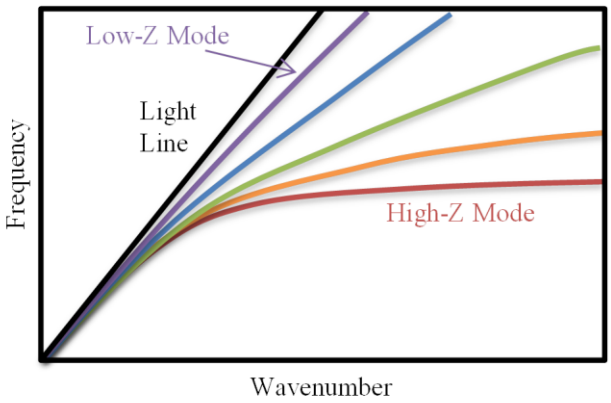

Figure 3.2: Dispersion diagram for an ideal tensor impedance surface. The relative locations of the curves correspond to the positions shown in Figure 3.1. The light line represents the dispersion relation of a plane wave in a vacuum. The low impedance mode is closest to the light line and the high impedance mode is the furthest from the light line. As the propagation direction is rotated from the low impedance direction to the high impedance direction the dispersion relation will gradually shift.

3.2.3 Higher Order Surface Modes

Printed circuit impedance surfaces support multiple bound surface modes. For isotropic impedance surfaces these modes are purely TM or TE, and a typical dispersion diagram for the lowest two modes of an impedance surface using a grounded dielectric substrate is shown in Figure 3.3. Figure 3.4 shows the field components of TM and TE modes traveling in the *x*- and *y*-directions. The field polarizations can be rotated by 90 degrees from the *x*-direction to obtain the *y*-direction components. However, Figure 3.4 has instead been drawn to show the similarities between the *x*-direction TM mode and the *y*-direction TE mode (and similarly the *y*- direction TM and *x*-direction TE modes). The in-plane electric and magnetic field polarizations are identical, and the difference is only in the out of plane component. Above the TE cutoff frequency both TM and TE modes are supported. In this region, for anisotropic structures, the ideal spatial dispersion (shown for the TM mode in Figure 3.2) does not occur. The ideal theory stipulates that the mode is purely TM on the principal axis, becomes TM-like as the direction of propagation is rotated away from the principal axis, and becomes purely

TM again at the orthogonal principal axis. In actuality, pure TM modes are supported along each principal axis, but the rotation between these pure TM modes does not occur. Instead, as the direction of propagation is gradually rotated from one principal axis to the orthogonal axis, the original TM mode gradually shifts to become a TE mode. The result of this phenomenon is that anisotropic unit cells cannot be used at frequencies where both TE and TM modes are supported because the surface does not support the desired TM-like mode in every direction. This will be shown explicitly in Section 3.3.

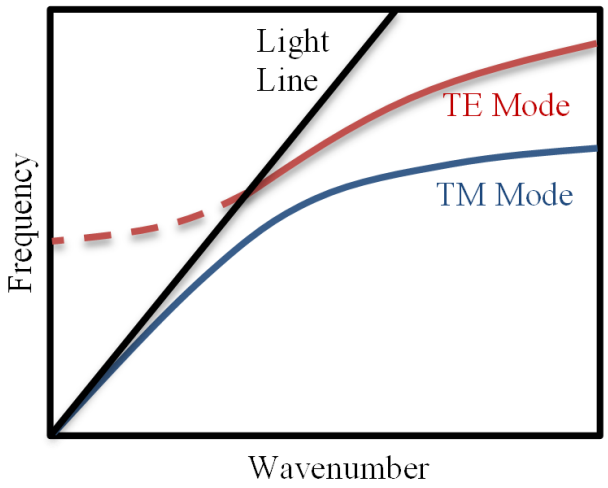

Figure 3.3: Typical dispersion diagram. The impedance surface is designed using a grounded dielectric substrate. The light line is the dispersion relation of a plane wave in a vacuum. The TM mode is the lowest order mode and remains below the light line. The TE mode starts above the light line as a leaky mode (marked as a dashed section) and becomes a bound surface wave above some cutoff frequency (marked as a solid line).

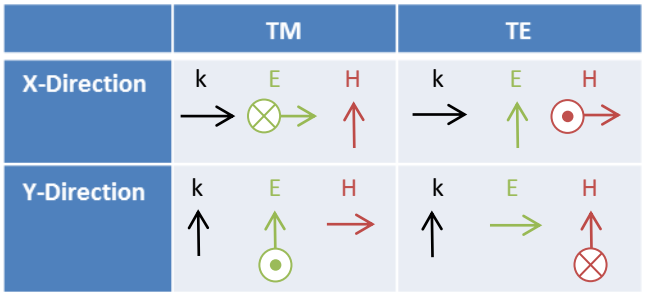

Figure 3.4: Vector field components for TM and TE modes. The surface waves are traveling in the *x*- and *y*-directions.

3.3 Unit Cell Designs

The goal of the unit cell design is to create a structure that has a large frequency bandwidth of highly anisotropic surface impedance. One stipulation for the design is that the unit cell must support bound surface waves in any direction along the surface. Corrugated surfaces and some printed circuit designs are highly anisotropic, but only support surface waves along a specific direction.

Three unit cell designs were studied. Each design used a grounded 1.575mm thick Rogers 5880 substrate ($\varepsilon_r = 2.2$), and the unit cell is square with lattice dimension a = 4mm. Diagrams of the three unit cells are shown in Figure 3.5. Figure 3.5a shows a patch design with no via. This design type, which includes a patch on a grounded dielectric substrate, has been published in multiple previous studies. These previous designs are illustrated in Figure 3.6, where Figure 3.6a shows a sliced patch structure [7], Figure 3.6b shows a sliced circular patch design [8], and Figure 3.6c shows a rectangular unit cell [33]. All three designs illustrated in Figure 3.6 have similar impedance ranges and anisotropy levels as the anisotropic patch unit cell in Figure 3.5a.

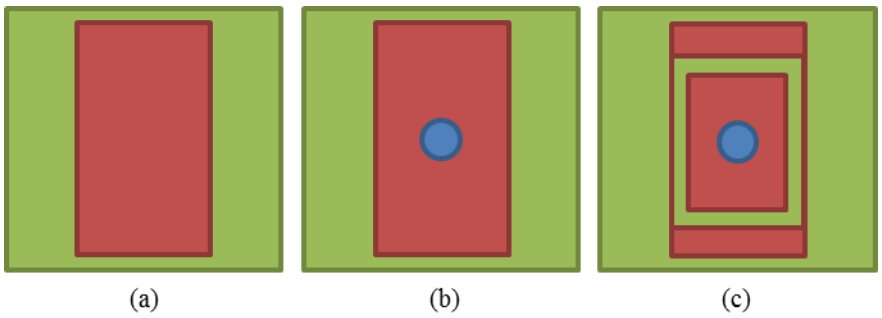

Figure 3.5: Anisotropic unit cells. (a) shows an anisotropic patch structure, (b) shows an anisotropic mushroom structure, and (c) shows an anisotropic ring-mushroom structure. In each case a top view is shown of the unit cell where the outer area is dielectric and the inner region is a metal patch on top of the dielectric. In (b) and (c) the circular region represents a metal via. The via has a diameter of 0.3mm. In each unit cell, the outer patch dimension is 2×3.75mm. In (c) the inner patch has dimension 1.4×2.4mm and the gap between the inner and outer patch is 0.15mm on all sides.

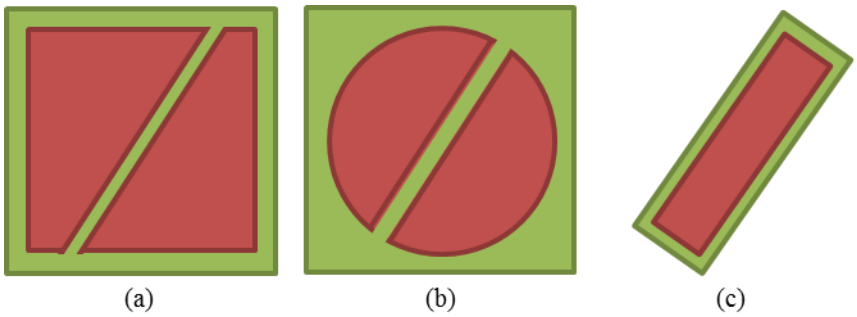

Figure 3.6: Previously published anisotropic unit cells. (a) shows a sliced patch structure, (b) shows a sliced circular patch structure, and (c) shows a rectangular patch and unit cell.

Figure 3.5b shows an anisotropic mushroom unit cell design. A traditional mushroom unit cell contains a square patch over a square unit cell [28], and an anisotropic mushroom cell has a rectangular patch. Figure 3.5c shows an anisotropic ring-mushroom unit cell. Figure 3.7 shows a perspective view of this ring-mushroom unit cell. The ring-mushroom structure has the same outer patch perimeter, but the interior region is sliced so that the via only connects to a smaller patch on the top plane. The total structure is a planar ring that surrounds a smaller mushroom. The result of the

decreased inner patch size is a decrease in the inductance of the unit cell as compared to the traditional mushroom structure. The inner patch size can be tuned so that at one extreme, the structure is identical to a mushroom, and at the other extreme, the structure is similar to a patch (with some deviation due to the via). The ring-mushroom structure has additional capacitance within the unit cell in series with the capacitance between unit cells. The additional series capacitance lowers the overall sheet capacitance of the structure. However, simulations of via-less structures show that the dominant effect on the dispersion relation is solely due to capacitance between unit cells which is identical for patch, mushroom, and ring-mushroom structures.

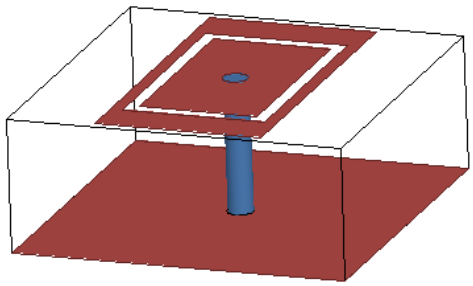

Figure 3.7: Perspective drawing of anisotropic ring-mushroom unit cell. Figure 3.5c is a top view of this structure. A ground plane is at the bottom of the unit cell and the dielectric is shown by the rectangular prism outline. A cylindrical via extends from the ground plane to the top of the dielectric. The patches are on the top surface of the dielectric.

Each unit cell was simulated using the eigenmode solver in Ansys HFSS version 15.0 (a full-wave, commercial software package). The unit cells were oriented so that waves traveling at 0° are in the high impedance direction waves traveling at 90° are in the low impedance direction (the *x*-axis is defined as 0°). Two intermediate angles were also simulated, and these were for phase velocity at 30° and 60° from the *x*-axis. The dispersion results of the patch unit cell are shown in Figure 3.8a. The TE cutoff for this geometry is at 14 GHz and below the cutoff only TM modes are supported by the structure. In this region below TE cutoff, the TM modes for all directions are nearly identical. However, despite being nearly isotropic, the impedance range shifts gradually from high to low as the wave propagation direction is rotated from 0° to 90°, as can be

seen in Figure 3.9a. Above the TE cutoff, the TM mode dispersion does not have the ideal form that is plotted in Figure 3.2. The TM dispersion curves for 0° and 90° are separated as desired, but the dispersion for 30° and 60° do not lie between the principal modes. Instead, the TM mode at 0° gradually shifts to become the TE mode at 90°. Similarly the TM mode at 90° gradually shifts into the TE mode at 0°. As discussed in Section 3.2, the TM and TE modes that travel in perpendicular directions have very similar field components. The simulations show that in the region above TE cutoff where both TM and TE modes are supported by the structure, the TM mode dispersion does not follow the ideal case and cannot be modeled as a tensor impedance surface. Therefore, the usable frequency range for this patch structure has very low and nearly isotropic surface impedance as shown in Figure 3.9a.

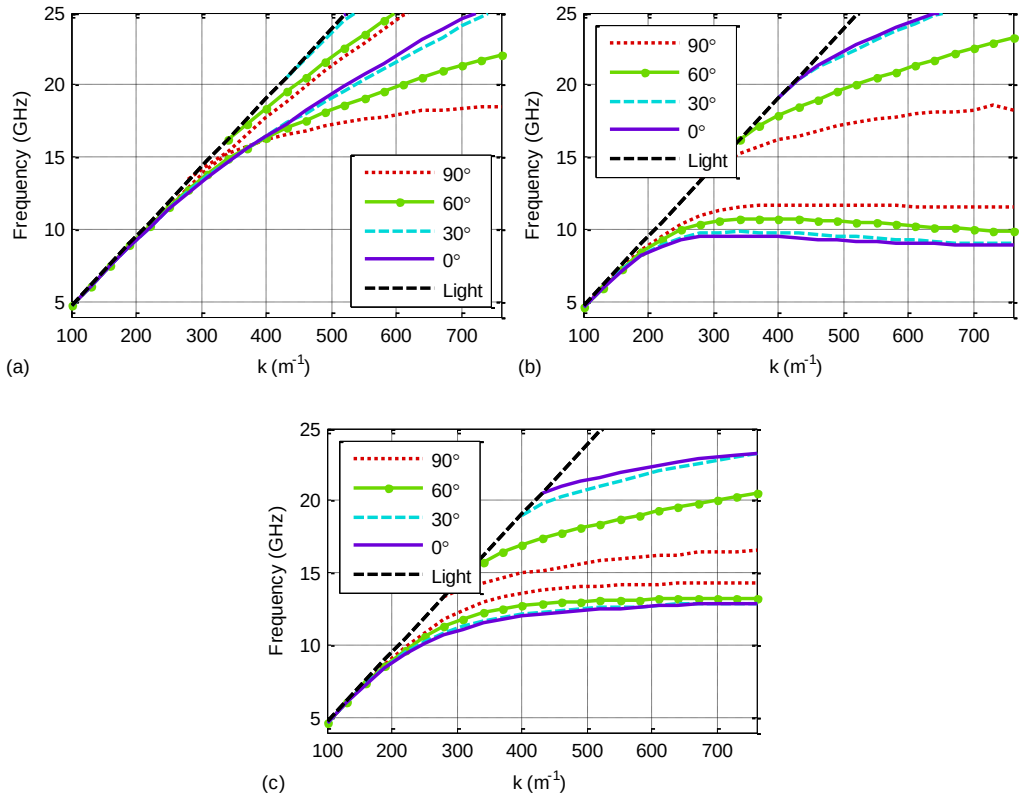

Figure 3.8: Dispersion diagrams. The plots show results for (a) patch, (b) mushroom, and (c) ring-mushroom unit cells. Four propagation directions are shown where 90° and 0° are the principal axes of the impedance tensor. The dispersion of light in a vacuum is shown as a black dashed line.

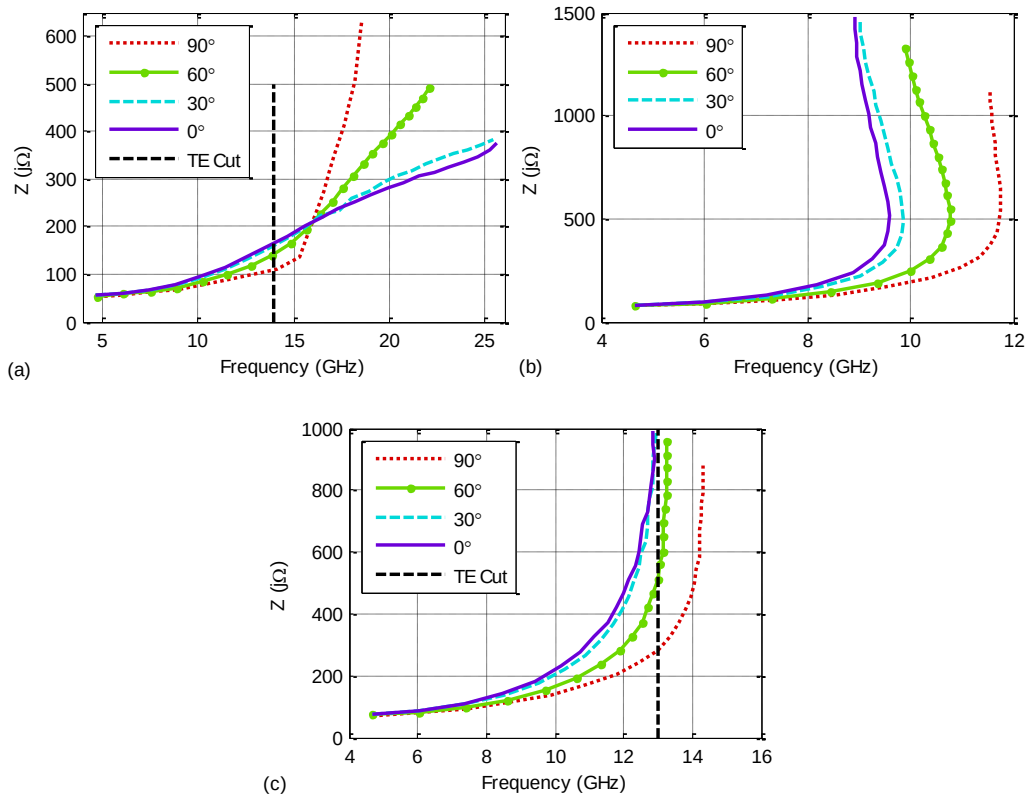

Figure 3.9: TM effective surface impedance. The plots show results for (a) patch, (b) mushroom, and (c) ring-mushroom unit cells. The cutoff frequency for the TE mode is shown in (a) and (c). In (b) the cutoff frequency lies at 14GHz. The impedance tensor has principal axes at 0° and 90°.

The patch unit cell is not usable as a tensor impedance surface above the TE cutoff. A mushroom unit cell avoids this issue by pushing the entire TM mode below the TE cutoff. Figure 3.8b shows the dispersion relation for an anisotropic mushroom structure. The TM mode now has a maximum frequency below the TE cutoff and there is a bandgap region between the TM and TE modes. Simulations of mushroom structures predict backward waves where phase and group velocity have opposite signs. However, to our knowledge, backward, bound, microwave-frequency, surface waves have never been measured. Experimental implementations have used volumetric 3D metamaterials [34, 35], transmission line modes [36-38], or leaky modes [39-41]. Along with being difficult to measure, backward waves also occur at frequencies where two

different TM modes are supported, and this could cause interference between the modes. Therefore, backward wave regions are not considered usable for the unit cell, and as seen in Figure 3.9b, the usable impedance range has a maximum value of Z_{xx} = j500Ω and Z_{yy} = j170Ω. Above this range only backward waves are supported on the surface.

The mushroom cell successfully suppressed the TM mode below the TE cutoff frequency, but it was suppressed so far that the backward wave region is dominant and the unit cell is not highly anisotropic over a broad bandwidth. The ring-mushroom structure suppresses the TM mode only enough to move it below the TE cutoff, but not so much that the mode becomes a backward wave. Figure 3.8c and Figure 3.9c show the dispersion and impedance relations of the ring-mushroom structure. The ring is tuned so that the TM mode peaks at the TE cutoff. For a fixed outer ring dimension, the tuning involved modifying the size of the inner patch. The ring-mushroom unit cell has a maximum anisotropy of Z_{xx} = j1000Ω and Z_{yy} = j280Ω. This is a significantly more anisotropic impedance than is obtainable with patch or mushroom structures.

In this paper the characteristics of the unit cell are determined by simulation as described above, and by experiment in Section 3.6. Multiple types of analytical models have also been created to study surface wave dispersion on similar structures. A transverse resonance method was used on an anisotropic patch geometry [26, 27], homogenization models were used with wire-medium slabs and mushroom structures [42], and a pole-zero matching method has been applied to patches on a grounded dielectric slab [43]. A potential topic for future study is to apply one of these methods, or another method, to create an analytical model for the ring-mushroom structure.

3.4 Performance Figure of Merit

The performance of the unit cells are compared using a figure of merit (FOM) that quantifies the anisotropy of the unit cell. The FOM is based on the effective surface index (henceforth referred to simply as “index”). The index for TM-like modes on a tensor impedance surface is direction dependent and can be related to the effective surface impedance, (3.2), as follows:

$$n(\theta)=\sqrt{1-\left(\frac{Z(\theta)}{Z_0}\right)^2}\,, \tag{3.4}$$

As with volume media, the index defines the phase velocity of the wave where $v_p=c/n$. The index for the ring-mushroom structure is shown in Figure 3.10, and it approaches one as surface impedance approaches zero. A FOM for anisotropy could use either the ratio of impedances or indexes for the modes propagating along the principal axes. However, the index ratio gives a more relevant measurement of anisotropy than the impedance ratio because at low surface impedances, high impedance ratios do not necessarily imply a highly anisotropic impedance surface. For example, a tensor surface with Z_{xx} = j20Ω and Z_{yy} = j10Ω has an impedance ratio of 2, but the corresponding index ratio is 1.001.

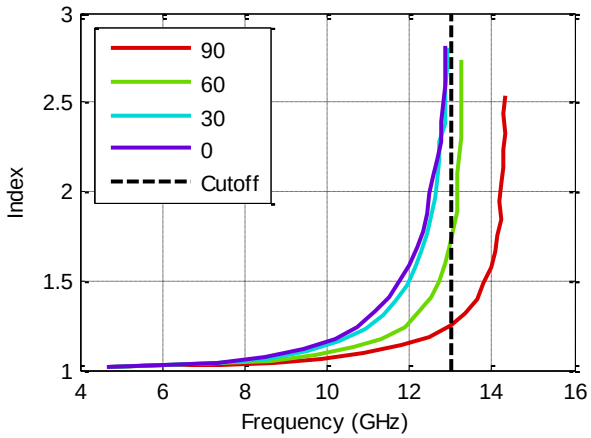

Figure 3.10: Effective surface index for ring-mushroom unit cells.

The FOM for highly anisotropic unit cells is designed to reward cells that have large index ratios over a large relative bandwidth. The FOM is defined below:

$$FOM = \int_{frequency} \frac{1}{f}\left(\frac{n_{high}(f)}{n_{low}(f)}-1\right)df\,, \tag{3.5}$$

where the range of the integral is the frequency range of the unit cell, f is frequency, n_{high} is the index of the high-impedance principal axis, and n_{low} is the index of the low-impedance principal axis. The ratio of the indexes is one for an isotropic material, and

this is subtracted off in the FOM so that the value only increases in anisotropic regions. The index ratio and the relevant integrated area are shown in Figure 3.11. The integral is scaled by inverse frequency so that the FOM is equal for equivalent relative frequency bandwidths (for example the FOM would be the same between 1-2GHz and 10-20GHz for appropriately frequency-scaled indexes).

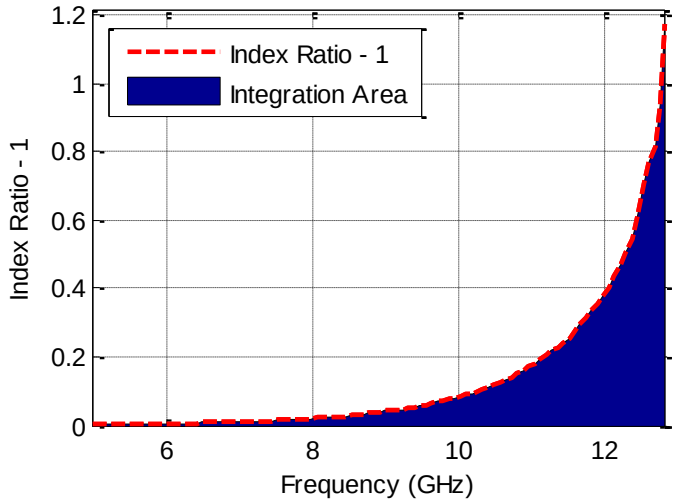

Figure 3.11: Index ratio and integration area of ring-mushroom unit cell. The index ratio, shown as a dashed line, is the ratio of the 0 and 90 degree curves shown in Figure 3.10 after subtraction by one. The integration area is the region which contributes to the FoM. In the FoM integral, each point is also divided by the frequency.

The FOM integral is over the entire frequency range of the mode which starts at DC and goes up to the maximum of the TM mode. The TM maximum is defined as whichever is lowest between the TE cutoff, the onset of the backward wave region, or the mode cutoff at $a = \lambda/2$. The integration method for determining the FOM is advantageous because it does not rely on any arbitrary performance cutoff. If a more traditional frequency bandwidth were used, some index ratio cutoff would need to be created which defined the threshold for a "highly anisotropic" material. For instance, an alternative bandwidth criterion could be the range of frequencies where the index ratio is greater than 1.1 (or any other arbitrary cutoff). This criterion was analyzed and gave qualitatively similar results to the FOM defined in (3.5). However, (3.5) is preferred

because it relies only on the fundamental characteristics of the unit cell and not a subjectively applied cutoff.

The patch, mushroom, and ring-mushroom unit cells analyzed in Section 3.3 have FOM values of 0.015, 0.062, and 0.112 respectively. This shows that the ring-mushroom structure significantly outperforms the patch and mushroom structures for this substrate. In the following section, the substrate is changed and the effect on the FOM is analyzed.

3.5 Variation of Substrate Height and Permittivity

Figure 3.8 and Figure 3.9 demonstrate the effects of altering the patch geometry and via presence on dispersion characteristics. The substrate permittivity and height also affect the properties of the unit cell. In Section 3.3 the substrate was Rogers 5880 (ε_r = 2.2) with a height of 1.575mm. In this section the substrate permittivity and height are varied independently.

In Figure 3.12, the unit cell has a height of 1.575mm, and ε_r is swept from 2.2 to 10.2, which is the range for commonly available, low-loss dielectrics. The other dimensions of the unit cell are held constant, along with the loss tangent. For the patch, the FOM increases with ε_r. The increased ε_r makes the substrate electrically thicker and pushes the TM mode to lower frequencies which have higher impedance. For the same wavenumber, lowering the frequency of a TM mode increases the surface impedance. This relation can be seen by rearranging (3.3):

$$Z_{TM} = Z_0 \sqrt{1 - \left(\frac{k_{TM} c}{\omega} \right)^2} \,. \tag{3.6}$$

Note that Z_{TM} is a positive imaginary number. Because of the significantly improved performance, practical designs consisting of patch unit cells generally use large dielectrics such as ε_r=10.2.

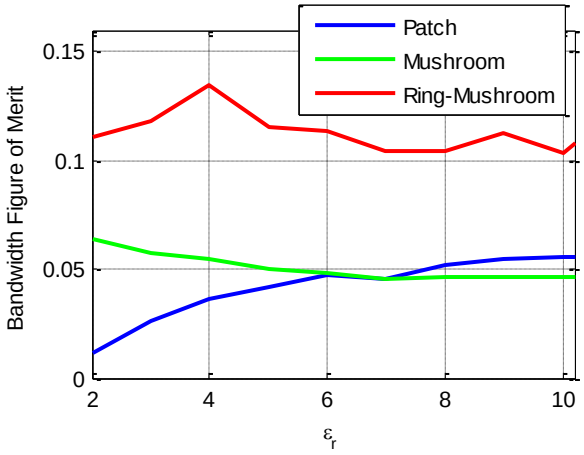

Figure 3.12: Unit cell performance vs. permittivity. The substrate permittivity is swept from ε_r=2.2 to ε_r=10.

The mushroom structure has a slight decline in FOM with ε_r. As with the patch, the increased ε_r causes the TM mode to lower in frequency. However, the mushroom, unlike the patch, has a backward wave region. For increasing ε_r, the onset of this backward wave region lowers in frequency further than the overall decrease of the mode. The result is the gradual decrease in FOM since backward wave regions are not included. The ring-mushroom structure increases in FOM initially but then falls and plateaus. In this case, the dimensions of the ring-mushroom structure are specifically tuned for ε_r=2.2. As the permittivity increases, the TE mode cutoff lowers and around ε_r = 4 starts to interfere with the TM mode, just as in the patch structure. Since integration region of the FOM stops at the onset of the TE mode, the result is the decrease in FOM for large ε_r. If the structure were tuned specifically for each ε_r value, the FOM would rise with permittivity.

In Figure 3.13a, the permittivity was fixed at ε_r=2.2 and the substrate height was swept from 0.5mm to 3.25mm. The FOM increases with substrate height for each unit cell design. For the patch, the increase in FOM is because the increased height, as with increased permittivity, lowers the frequency of the TM mode and thus raises the impedance as described by (3.6). The mushroom structure also shows FOM improvement with increased substrate height. For the mushroom structure, increased

substrate height, unlike increased substrate permittivity, lowers the overall TM mode frequency more significantly than it lowers the onset frequency of backward waves. The ring-mushroom structure has increased FOM, and in this case, the TM mode is lowered more quickly than the TE mode so there is no plateau as seen in Figure 3.12. The ring-mushroom structure performs the best at all heights except for very thin substrates where the mushroom structure performs better.

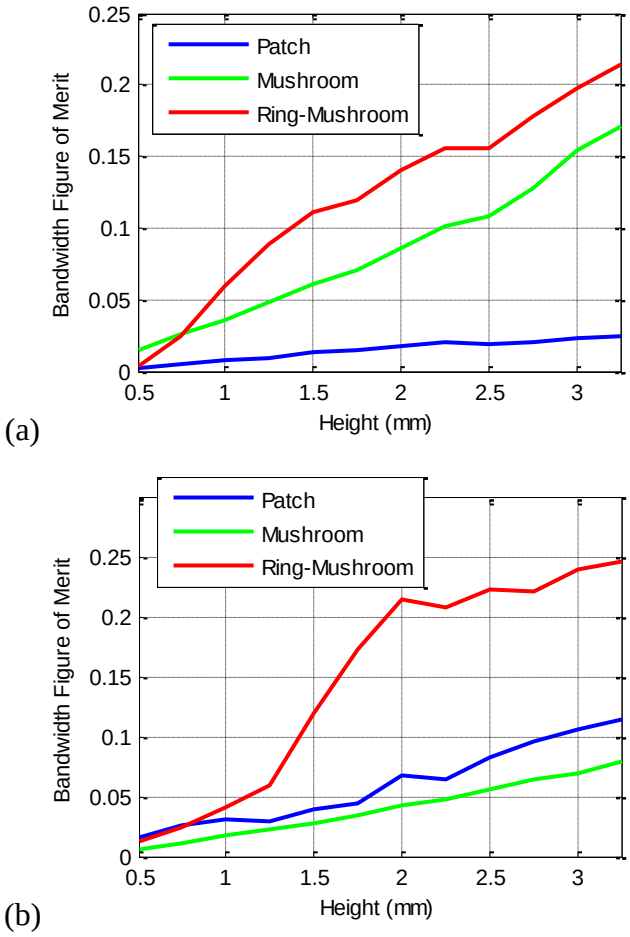

Figure 3.13: Unit cell performance vs. substrate height. The substrate height is swept from 0.5mm to 3.25mm for (a) ε_r=2.2 and (b) ε_r=10.2.

In Figure 3.13b the substrate permittivity is set to ε_r=10.2, and the substrate height is again swept from 0.5mm to 3.25mm. The patch unit cell now has a slightly higher bandwidth than the mushroom structure, which is consistent with the ε_r=10.2

region of Figure 3.12. All three unit cells again show bandwidth improvement as the substrate height increases. The ring-mushroom structure again has a bend in the curve which corresponds to the frequency at which the TM mode is suppressed completely below the TE mode. The FOM for the ring-mushroom unit cell is still significantly higher than either the patch or mushroom unit cells except for very thin substrates.

3.6 Experiment

Three surfaces were fabricated using printed circuit fabrication technology. The surfaces were each 10×16 inches with the high impedance direction along the 10 inch dimension. Photographs of zoomed-in sections of each surface are shown in Figure 3.14. The unit cells were designed identically to those simulated in Section 3.3: ε_r = 2.2, a = 4mm, outer patch dimensions of 2×3.75mm, inner patch dimensions of 1.4×2.4mm and gaps between the inner and outer patch of 0.15mm on all sides. The only difference between the experimentally fabricated surfaces and the simulated versions is a fabricated via diameter of 0.38mm instead of the desired 0.3mm simulated dimension (due to a larger-than-anticipated drill used in fabrication). Each surface was measured using a near field scanner. A surface wave was excited using a small triangular antenna, and a vertically polarized probe was scanned 2mm above the surface along a line. An Agilent E5071C vector network analyzer recorded the phase of the surface wave at 200μm increments. Magnetic radar absorbing material was placed at the edge of the surfaces to limit reflections. The phase velocity of the surface wave was obtained from the phase measurements, and this phase velocity was used to determine the dispersion relation. Each surface was measured along both principal axes and also at an angle bisecting the principal axes at 45°.

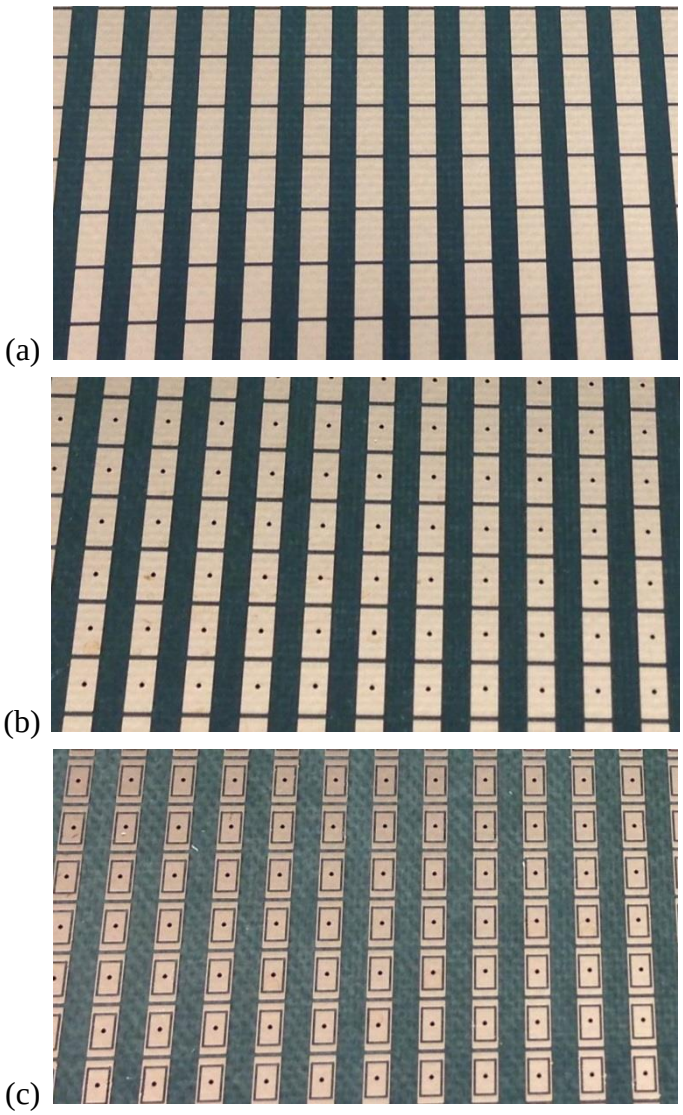

Figure 3.14: Photographs of each unit cell. The photographs show (a) patch unit cell, (b) mushroom unit cell, and (c) ring-mushroom unit cell.

For the principal axes, the measured dispersion is compared directly to the simulated versions comparable to those shown in Figure 3.8 (the High-Z and Low-Z principal axes are 0° and 90° respectively). The simulated response is slightly different than Figure 3.8 due to the increased via diameter. For non-principal axis measurements, simulation and experiment cannot be compared directly. In simulation, the unit cells are measured using the eigenmode simulator in which the phase across the unit cell is defined. In this way, the curves labeled as 30° and 60° in Figure 3.8 are defined with

respect to the direction of the phase velocity. For the measured response, a straight line in the physical space (not the phase space) was measured oriented 45° from the *x*-axis. This 45° angle represents the angle of power flow over the unit cell and not the angle of the phase velocity. For anisotropic materials, the direction of power flow is not the same as the direction of phase velocity, and this has been studied specifically for surface waves on structures with no via [44]. In order to relate phase velocity and power flow (and compare the simulated and measured results) we have assumed elliptical phase fronts on the surface. Real surfaces do not have perfectly elliptical phase fronts, but the assumption is good enough to give closely matching measured results. At a given frequency, the index in each principal direction is known, and each other direction is obtained by the assumption of elliptical phase fronts. For a point on the ellipse, the phase velocity is tangential to the ellipse, and the power flow is in the direction from the center of the ellipse to the point. The phase velocity was swept in simulation to find the modes where the angle of power flow was 45° as desired.

Measured and simulated dispersion curves are plotted in Figure 3.15. In Figure 3.15a, the dispersion of the patch structure is shown. As predicted by the simulated results in Figure 3.8a, surface waves along the principal axes are supported up to at least 20 GHz (the upper frequency limit of the VNA). The high-Z measurement had a region between 16.1 and 17.3 GHz where the measurement was extremely noisy and was removed from the plot. Simulation predicts that the mode is supported here, but it is also the frequency around which the TE mode crosses the TM mode. In the measurement, this region is most likely noisy due to coupling between the TM and TE modes. At 45 degrees, the measurement no longer shows a surface wave above 15 GHz. For the patch structure, simulation shows that the TE mode cutoff is at 13.8 GHz and the TE and TM modes cross at 15 GHz. For the measurement, the TM mode is never supported above 15 GHz, and this is matched by the simulation which shows a breakdown of the TE mode around this frequency.

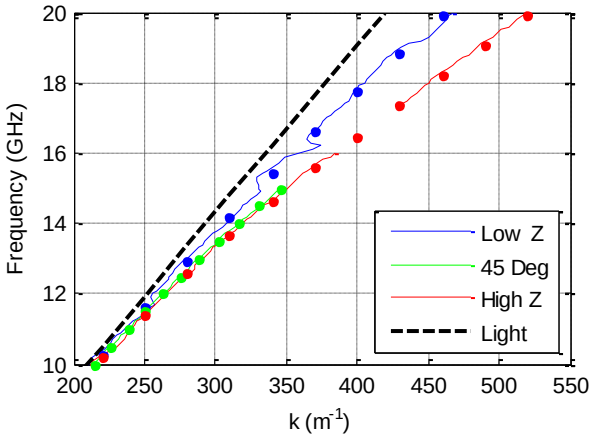

(a)

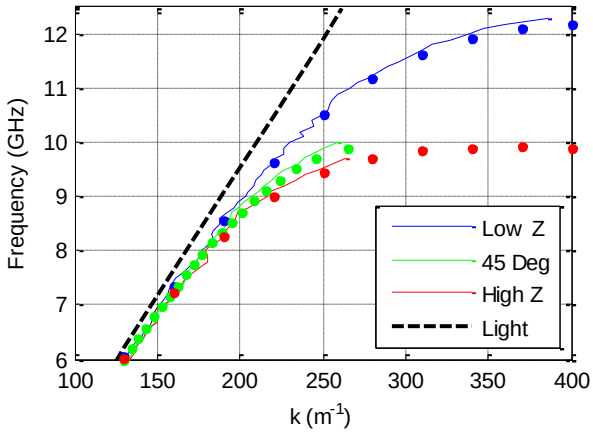

(b)

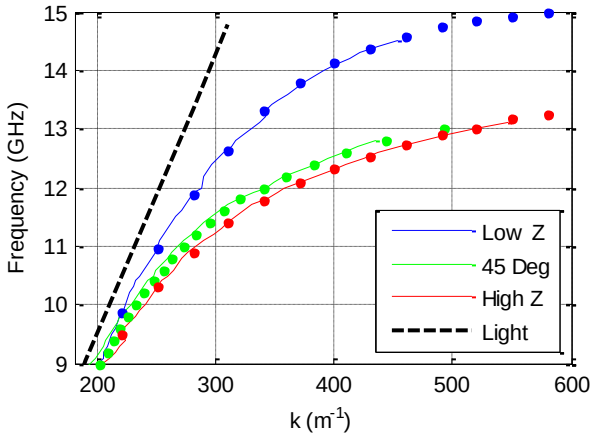

(b)

Figure 3.15: Measured and simulated dispersion curves. Results are for (a) patch unit cell, (b) mushroom unit cell, and (c) ring-mushroom unit cell. Measured curves are solid lines, and simulated are dots. The simulated dispersion curves uses a via diameter of 0.38mm to match the fabricated surfaces. The 0.3mm via diameter simulations shown in Figure 3.8 have very similar dispersion, although not identical.

Figure 3.15b shows the dispersion for the mushroom structure. Measurement and simulation show good agreement. The measurement curve tops out when the mode is too closely bounded to the surface to be picked up by the probe. In Figure 3.15c, the ring-mushroom structure also shows good agreement between measurement and simulation. The measurement again tops out in the region where significant wave power is located below the probe. Overall the measurement shows close agreement to simulated structures. The measured response demonstrates the fact that the ring-mushroom structure can obtain highly anisotropic surfaces beyond what is possible with equivalent patch or mushroom unit cells.

3.7 Conclusion

A unit cell with highly-anisotropic tensor surface impedance was presented. For structures using a grounded dielectric, the TM mode is fundamental and it is shown that highly-anisotropic unit cells can only operate below the cutoff frequency of the TE mode. Patch unit cells without vias do not operate fully below the TE mode. Mushroom unit cells operate below TE mode but have narrow bandwidth and a large backward-wave region which is difficult to excite experimentally. A ring-mushroom unit cell operates below the TE cutoff but does not have backward waves. This allows ring-mushroom unit cells to achieve highly-anisotropic tensor impedance. A figure of merit was created that demonstrates the improved bandwidth and anisotropy of the ring-mushroom unit cell. The unit cells were each fabricated experimentally and showed good agreement to simulation. In future work, the unit cell will be applied to practical structures which require large anisotropy.

Chapter 3 is based on and mostly a reprint of the following paper: R. Quarfoth, D. Sievenpiper, “Broadband Unit Cell Design for Highly-Anisotropic Impedance Surfaces”, *IEEE Transactions on Antennas and Propagation*, vol. 62, no. 8, pp. 1-10.

Chapter 4 Tensor Impedance Surface Waveguides

4.1 Overview

Waveguides have many applications in antenna and microwave design along with integrated circuits and other areas. Ideally these structures transmit electromagnetic waves over large distances with minimal loss. This study investigates the waveguide capabilities of a tensor impedance surface waveguide.

We have applied the tensor impedance surface theory to the problem of designing a planar waveguide using regions of different surface impedances as shown in Figure 4.1. We used a simple ray optics method to determine the approximate dispersion relation in the surface waveguide. Ray optics methods have been developed for uniaxial crystals [45, 46], and also biaxial crystal media [47, 48]. Similar to dielectric slab waveguides, a surface waveguide is formed if an interior surface has a larger effective index than its surrounding surfaces. Dielectric slab waveguides have been studied by multiple groups. Isotropic dielectric slabs are studied in many textbooks (e.g. [49]). Anisotropic slab waveguides have been studied using mode analysis [50] and also using ray optics [51]. By applying the ray optics model to a surface structure, we can predict the dispersion relation for a structure with arbitrary dimensions and impedances in either the guiding or exterior regions. We verify the theory by simulating the structure using HFSS. Results show agreement over a wide range of impedance values.

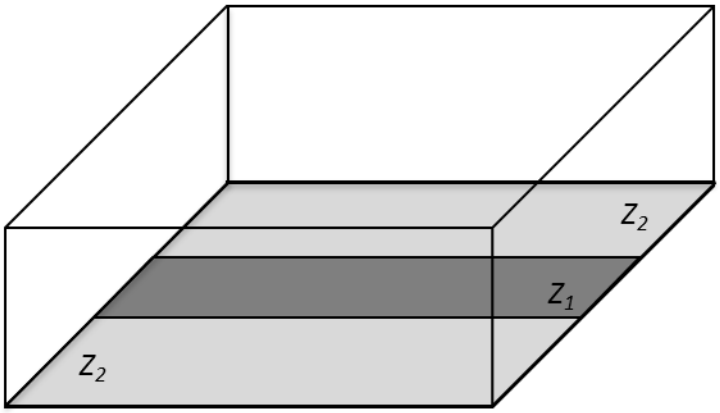

Figure 4.1: Impedance surface waveguide design. Surface waves are contained within an interior region of impedance Z_1. The region above the surfaces is a vacuum.

4.2 Ideal Artificial Tensor Impedance Surface Waveguides

In this section, waveguides constructed using ideal tensor impedance boundary conditions are theoretically modeled and simulated.

4.2.1 Surface Waveguide Theory

The surface waveguide consists of an interior high impedance strip surrounded by two low impedance areas as shown in Figure 4.2. Both the high and low impedance regions are planar with vacuum above the plane. The waveguide is aligned along the X-axis. Previous work has shown that the ray optics method can predict wave propagation in slab-shaped volumetric regions where an interior slab has a higher index of refraction than the adjacent regions [49]. A similar method is used here to predict wave propagation on a planar structure.

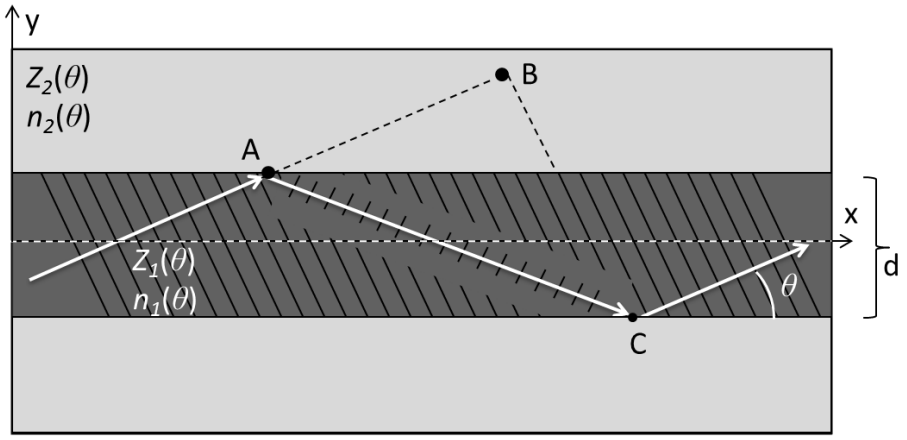

Figure 4.2: Ray optics model for surface impedance waveguide. Waves are guided losslessly if total internal reflection occurs at the boundary between the media. The Z-direction (out of the page) is a vacuum. To satisfy the self-consistency condition, a twice reflected wave must be in phase with a wave that does not reflect. At each reflection between media, the wave exhibits a phase shift.

In the ray optics method, the wave is assumed to be a single ray at an angle θ from the X-axis as shown in Figure 4.2. The wave is losslessly guided when it exhibits total internal reflection at the boundary between the high impedance region (values associated with this region have subscript 1) and low impedance region (values associated with this region have subscript 2). Using the convention that $k_1=n_1k_0$, where k_0 is the free space wave number, k_1 is the wavenumber along the surface in region 1, and n_1 is the effective index for surface waves in region 1, we can write k_x and k_y as

$$k_x = k_1 \cos(\theta), \tag{4.1}$$

$$k_y = k_1 \sin(\theta). \tag{4.2}$$

From equation (2.11) α_z can be solved as

$$\alpha_z = k_0 \sqrt{1-n_1^2}\,. \tag{4.3}$$

Along with the ray optics constraints, a traveling wave in the guide must satisfy the self-consistency condition. The condition requires that a twice reflected wave must be in phase with a wave that travels without reflection. The condition is shown geometrically in Figure 4.2 where the phase delay from point A to point B must be equal (± multiples of 2π) to the phase delay from point A to point C. For the twice reflected

path, point A to point C, there are also two phase shifts, one at each reflection. The self-consistency condition gives the following result:

$$k_y = \frac{\pi m + \varphi}{d}, \tag{4.4}$$

where φ is the phase shift at reflection, d is the width of the guiding region, and m is an integer greater or equal to zero which represents the mode number. Depending on the geometry, multiple modes can be supported because the phase delays can be different by integer factors of 2π.

To solve for the reflection phase shift, the well-known Fresnel equations can be modified for surface waves. In the plane of the tensor surface, waves have propagating and transverse components of both the electric and magnetic fields. Each of these field components must be continuous across the interface between the high and low impedance region. Using the structure as shown in Figure 4.3, the reflection coefficient can be solved as

$$\Gamma = \frac{n_1(\theta_i)Z_2(\theta_i)\cos\theta_i - n_2(\theta_i)Z_1(\theta_i)\cos\theta_t}{n_1(\theta_i)Z_2(\theta_i)\cos\theta_i + n_2(\theta_i)Z_1(\theta_i)\cos\theta_t}, \tag{4.5}$$

where Z_1, Z_2, n_1, and n_2 are dependent on θ as described by equations (2.7), (2.9), and (2.11). To solve for (4.5), we approximate each hybrid mode as a pure TM mode on a surface with the effective impedance given by (2.9). This method is much simpler than solving with the full tensor condition and has shown good agreement with simulation. In the isotropic case when $\gamma=0$ on both sides of the boundary, Z_1, Z_2, n_1, and n_2 are all constant with respect to the direction of propagation in θ_i.

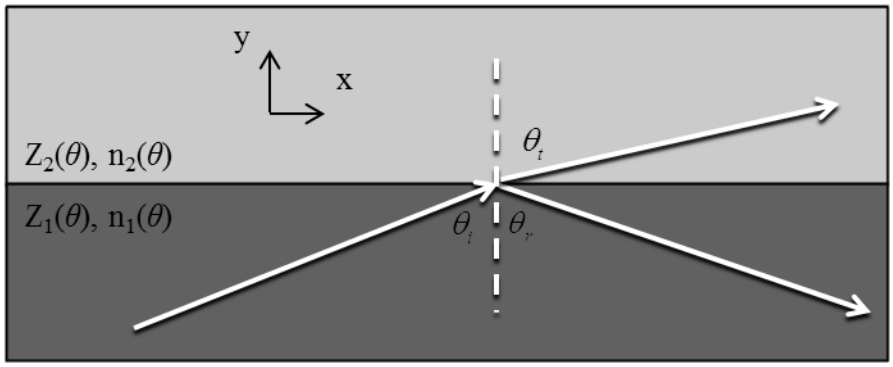

Figure 4.3: Geometry for Fresnel reflection. Each medium can have an angle dependent characteristic impedance. The incidence angle θ_i is the complement angle to θ of the ray optics method.

The phase change on reflection, φ, from (4.4) can now be expressed as

$$\varphi = angle(\Gamma). \tag{4.6}$$

The phase change, φ, also accounts for the Goos-Hänchen shift which occurs for waves reflected at the interface. If the impedance tensor is known, we now have enough information to solve numerically for a dispersion relation. Equations (4.1), (4.3), and (4.4) can be inserted into (2.10) to get a dispersion relation as

$$-\left(\frac{\pi m+\varphi}{d}\right)^2+\frac{n_1(\theta_i)^2\omega^2}{c^2}\sin^2\theta=0. \tag{4.7}$$

where c is the speed of light in a vacuum. We can solve (4.7) numerically to get the dispersion relation between the frequency and wavenumber of the surface wave k_1.

4.2.2 Tensor Impedance Simulation

In order to validate the waveguide theory through simulations, we designed a simulation structure that approximates a lossless, reciprocal tensor impedance boundary. HFSS version 14 has a built in anisotropic impedance boundary called "Screening Impedance". This boundary supports surface waves in the driven mode but it does not support for surface waves in the eigenmode simulator. We developed an alternative impedance boundary structure in order to simulate in the eigenmode simulator. This alternative structure also demonstrates a method for deconstructing a tensor impedance

surface into multiple scalar elements. A unit cell of our proposed model for a tensor impedance surface is shown in Figure 4.4. More recent versions of HFSS (starting with version 15) have implemented the tensor impedance boundary for the eigenmode solver. Therefore, these newer versions do not require a new unit cell to model tensor impedance surfaces. However, the following analysis shows that a tensor impedance surface can still be modeled using scalar boundary conditions.

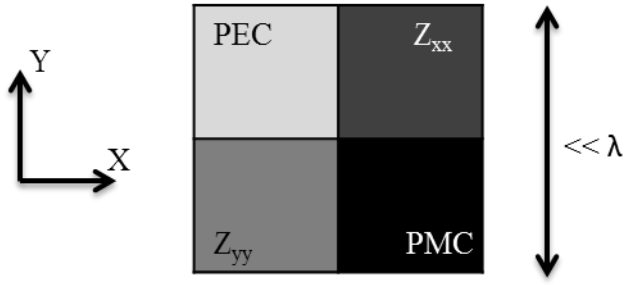

Figure 4.4: Checkerboard structure. The structure can be simulated to approximate a tensor impedance surface boundary. The structure has two isotropic impedance surface boundaries labeled Z_{xx} and Z_{yy}.

The unit cell consists of four ideal scalar boundaries: perfect electric conductor (PEC), perfect magnetic conductor (PMC), and two isotropic impedance boundaries which are labeled Z_{xx} and Z_{yy} in Figure 4.4. An arbitrarily large surface can be constructed by repeating the unit cell in two dimensions. The size of the cell must be small compared to the wavelength being tested. In the actual implementation, the PEC had to be replaced with a finite conductivity boundary because the HFSS eigenmode simulator does not allow a periodic boundary to be in contact with both an impedance and PEC boundary. The difference between the PEC and finite conductivity boundaries was a negligible decrease in conductivity from 1e30 S/m to 1e29 S/m.

For small cell sizes the checkerboard can be modeled in the long wave limit, and the effective surface impedance can be obtained by averaging over the cells for a specific wave direction. For a wave propagating in the x-direction, the PEC and Z_{xx} boundaries are in series and average to a surface of $Z_{xx}/2$ since the surface impedance of PEC is zero. The Z_{yy} and PMC boundaries are also in series and average to infinity since

the surface impedance of PMC is infinity. Averaging $Z_{xx}/2$ and infinity in parallel using the harmonic mean gives an X-direction impedance of Z_{xx}. For a wave propagating in the y-direction, the same analysis gives an impedance of Z_{yy}. Near field effects occur immediately above the checkerboard surface and result in a complicated field profile. Above the boundary at a length on the order of the unit cell size or greater, the ratio of the electric and magnetic fields equals the effective impedance that is solved from the previous description. This is a reason why the unit cell must be small with respect to the wavelength. There are two different impedances in the principal directions that can be obtained using the averaging method. Simulations are performed to verify that these principal-direction impedances are modeled correctly using the long-wave limit and to verify that hybrid modes are supported at intermediate angles.

A surface that correctly models a dispersion-free tensor impedance surface boundary must satisfy two conditions. First, the impedance on the surface must be constant with respect to frequency. Preferably for this surface, the impedances of the X- and Y-directed waves are equal to the input values of Z_{xx} and Z_{yy}. Second, the surface must have the correct impedance vs. propagation direction relation as defined by (2.9). To verify the two conditions, the checkerboard structure was simulated in HFSS using the structure as shown in Figure 4.5. The eigenmode simulator is used to solve for the dispersion of an infinite checkerboard lattice. Simulating over a single unit cell or multiple cells (Figure 4.5 shows an 8x8 lattice) has no effect on results. This is expected because regardless of the number of unit cells tested, the simulator models an equivalent infinite structure.

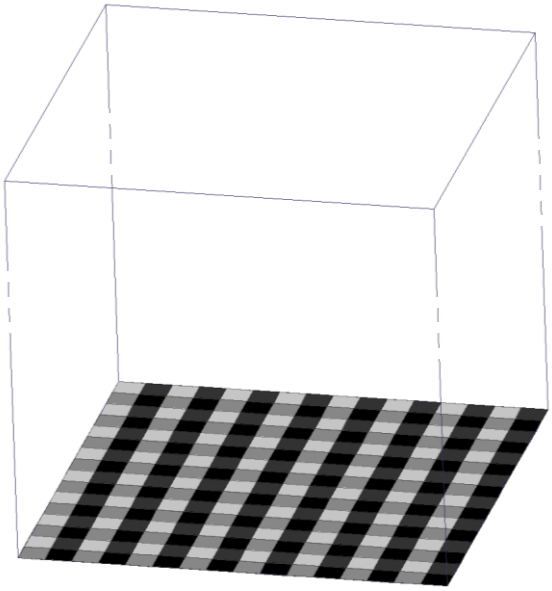

Figure 4.5: Simulation structure in HFSS for checkerboard surface. The lattice is repeated multiple times over two dimensions. The eigenmode simulator finds dispersion results for an infinite lattice. The height of the air box above the surface is not to scale.

Propagation along the principle directions of two lattices was simulated and the resulting wave impedances are shown in Figure 4.6. The simulated impedance is obtained from the ratio of the longitudinal electric field and the transverse magnetic field. For both lattices the wave impedance matches the input values over a wide frequency range. At higher frequencies the simulated surface impedance varies by approximately 2% from the desired value. If the lattice size is increased from 0.1mm (as shown) to 0.2mm, the maximum error rises to around 6% in this frequency range. In general, increasing the unit cell size causes increased dispersion. Arbitrarily small errors can be obtained by shrinking the size of the lattice, at the cost of increased simulation time. The Z_{xx} curve in Figure 4.6 shows that the impedance rises at low frequencies. This is due to the chosen height of the vacuum simulated above the impedance surface. We used PEC for the top boundary in this model to improve simulation convergence, but this can cause errors if significant wave power is present at the top of the structure. Increasing the box height eliminates the effect of the top boundary. In general, as the desired frequency range is lowered, a taller box is needed to properly determine the

impedance. Low impedance values also require a larger box because fields are more loosely confined. By choosing a sufficient box height and shrinking the unit cell to the necessary size, the effective scalar impedance of the checkerboard structure can be arbitrarily constant with respect to frequency.

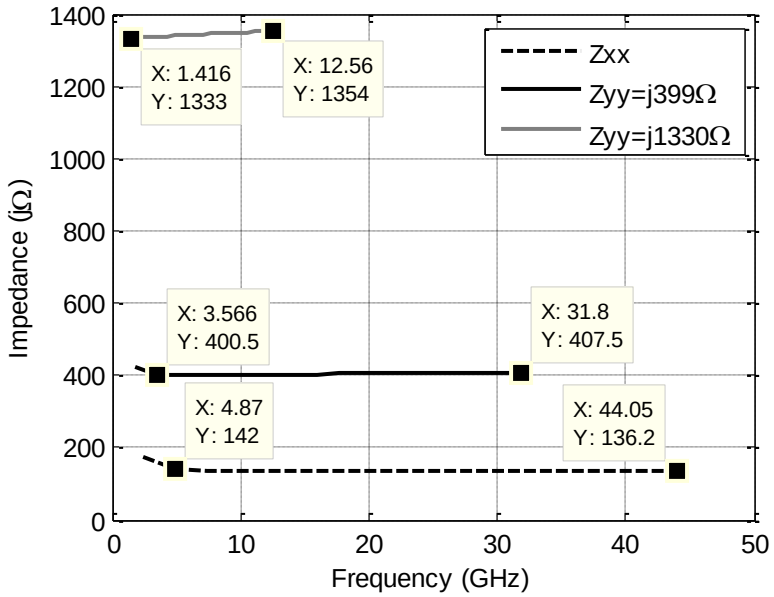

Figure 4.6: Impedance vs. frequency. The waves propagate in the X- and Y-directions. Two different Y (propagating) direction impedances were tested, Z_{yy}=j399 Ω and Z_{yy}= j1330 Ω. All other parameters were identical in both simulations: unit cell length=0.1mm, Z_{xx}= j133 Ω, and vacuum height=45mm.

Along with having dispersion free impedance, tensor impedance surfaces must respond correctly for wave propagation at any angle. Figure 4.7 shows the simulated and theoretical impedance as a function of propagation direction for the two lattices discussed above. For both cases in Figure 4.7, the theory and simulation match very closely. This shows that the propagation characteristics and field decay above the checkerboard matches the theory for hybrid TM-like modes. Therefore, we now have shown that an appropriately designed checkerboard structure correctly models a tensor impedance surface.

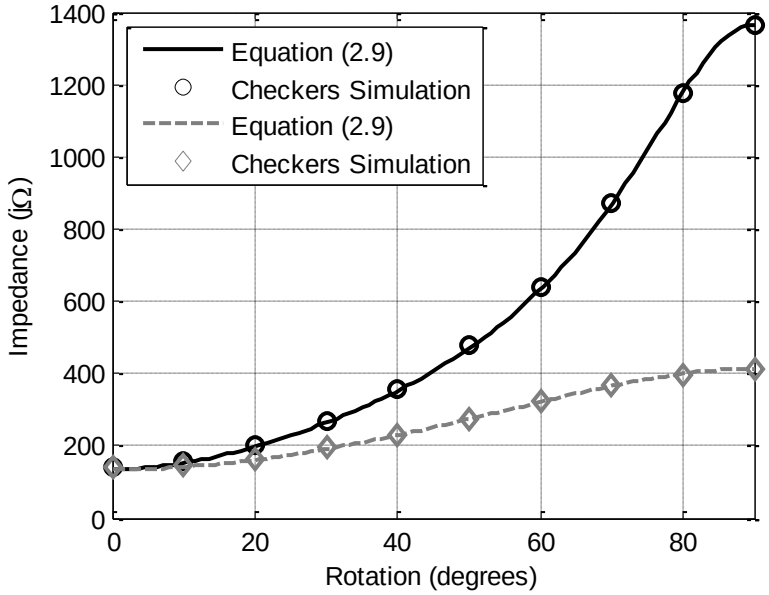

Figure 4.7: Effective scalar impedance vs. propagation direction. The simulation is from a checkerboard structure with dispersion results shown in Figure 4.6. Impedance was simulated for multiple rotation angles. The theoretical solution is obtained from (2.9). For the theory, Z_{xx} and Z_{yy} values at 10GHz from Figure 4.6 were used. For both anisotropy levels, the theoretical angle-dependence of impedance matched the simulated result.

4.2.3 Anisotropic Waveguide Results

We modeled anisotropic waveguides using the eigenmode solver in HFSS. An inner guiding section was constructed using the checkerboard structure discussed in the previous section. The outer region used an isotropic impedance boundary condition as shown in Figure 4.8. Periodic boundary conditions were used to solve for the dispersion relation of surface waves propagating along the guiding region.

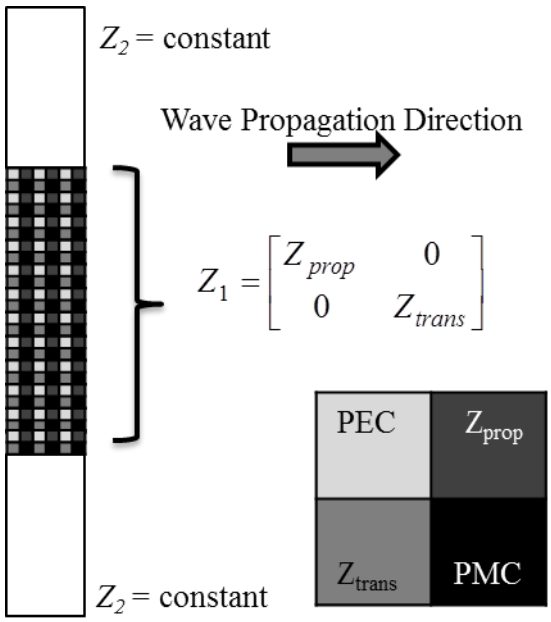

Figure 4.8: Simulation structure of the checkerboard guide. The guide interior is an anisotropic checkerboard surface. The exterior region is an isotropic scalar surface Z_2=j133Ω. The guide drawing is not to scale. The details of the checkerboard are re-plotted (another version is also shown in Figure 4.4). The vacuum height above the surface is 45mm, and the unit cell size is 0.1mm by 0.1mm. The width of each guide was set to 18mm which required 180 unit cells (only 12 unit cells are shown in the figure).

Two guides were tested, one with low anisotropy and another with higher anisotropy. Figure 4.9 shows the magnitude of the electric field for the lowest three modes in the lower anisotropy guide. Multiple modes can be supported in the guide as described in (4.4) and (4.7). Fields are bounded to the surface and concentrated within the guiding region. The fields have sinusoidal variation within the guide and decay exponentially outside and above the guide surface. No power leaks away at the guide edges, and the wave is transmitted without losses.

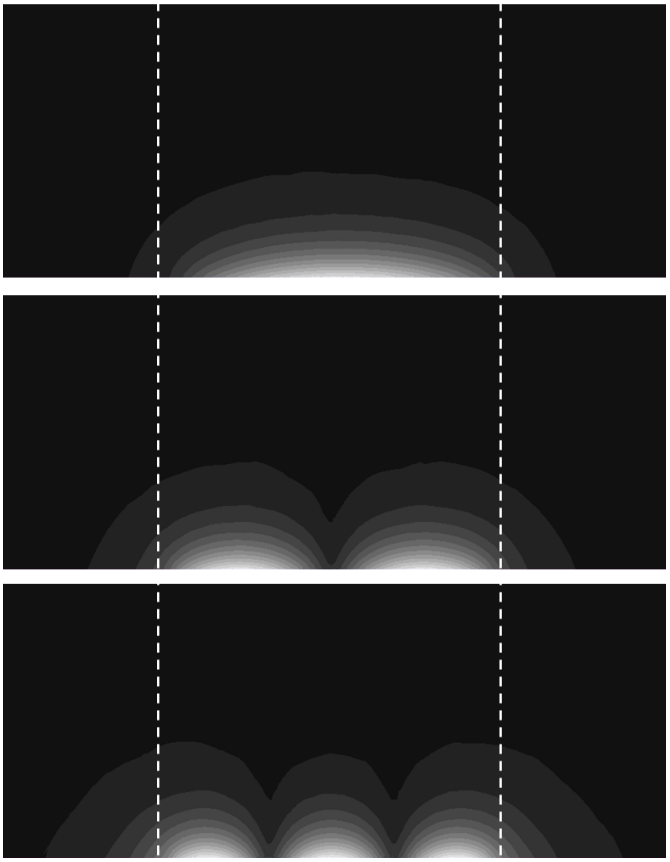

Figure 4.9: Magnitude of the electric field. The lowest three modes of the guide are shown (logarithmic scale). The structure is a checkerboard structure with Z_{prop}=j399Ω and Z_{trans}=j133Ω. The field has sinusoidal variation within the guide and exponential decay above and outside the guide. The high-impedance guiding region is bounded by the dotted line shown in each figure.

The dispersion relations for the two guides are shown in Figure 4.10. Figure 4.10a shows that in the low anisotropy case, the theory matches the simulation well for the lowest three modes of the guide. For any mode, the frequency must lie below the line labeled "Outer Region." This is the dispersion relation for a surface wave on a uniform surface with impedance equal to that of the region outside the guide. Since the outer region has a lower impedance than the interior, it represents the highest possible frequency-wavenumber ratio in the structure. For the higher anisotropy case shown in Figure 4.10b, the simulation and theory deviate somewhat, especially for the higher modes. The deviation is caused by the increased fraction of TE field components in the

mode on the high-anisotropy surface. Figure 2.2 shows the fraction of TE field in the mode for the low and high anisotropy cases. The TE component of the hybrid mode is not supported by the isotropic TM surface that bounds the guide. In order to simplify the theory, a single TM surface wave ray was used to match these components as shown in Figure 4.3 and described in Section 4.2.1. The single TM ray is set to the effective impedance of the tensor surface, but this does not perfectly model the interaction at the edge of the guide. In reality there is a discontinuity in the mode since the interior region contains a TM-TE hybrid mode and the exterior region is a pure TM mode. This discontinuity can induce plane wave scattering into the surrounding space and is difficult to model. However, the results show that the simple ray optics model is still sufficient to roughly predict the dispersion relation for a highly-anisotropic tensor impedance guide.

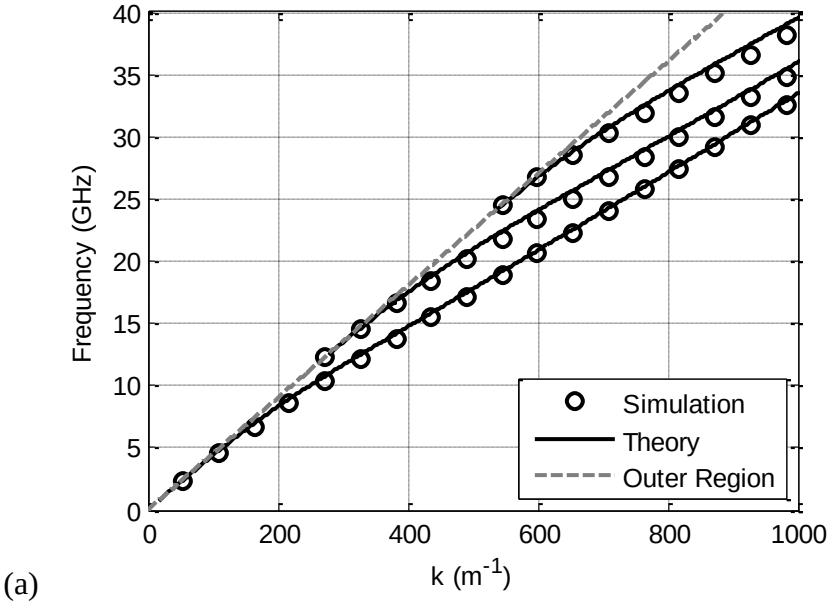

(a)

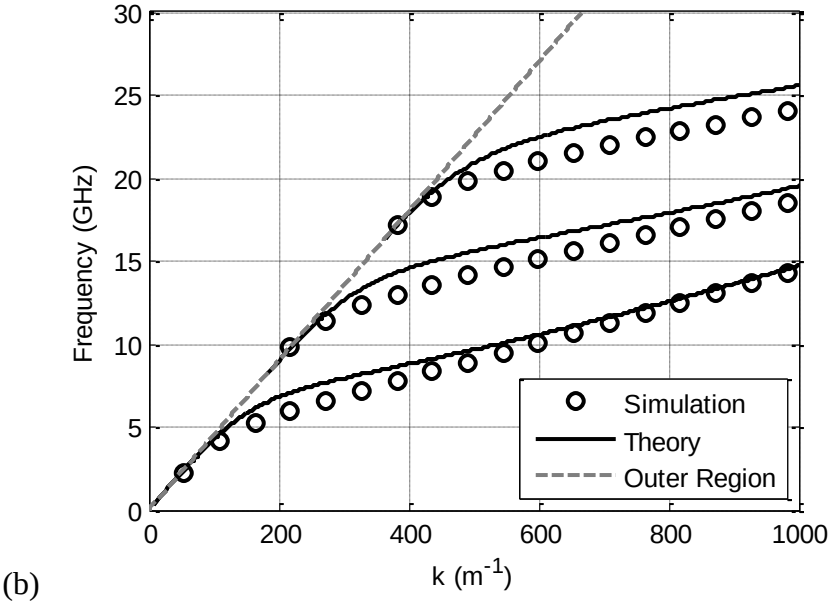

(b)

Figure 4.10: Frequency vs. wavenumber plot for a checkerboard guide. The tensor impedance is Z_{trans}=j133Ω and (a) Z_{prop}=j399Ω, (b) Z_{prop}=j1330Ω. The simulated points are shown as circles. The theory line is the response as predicted from the ray-optics method. The line labeled Outer Region represents the dispersion relationship of a surface wave on a uniform surface with Z_2=j133Ω. This is the (isotropic) impedance of the region outside the guide.

Scalar impedance waveguides were also simulated (not shown), and these isotropic guides also show matching results between theory and simulation. The theory can be simplified significantly for isotropic boundaries because only pure TM modes propagate on the surface and the impedance boundary condition is satisfied with a scalar value instead of a 2x2 matrix. For every level of anisotropy tested, waves were guided losslessly within the guiding region, and fields decayed exponentially outside and above the guide. In general, wider guides and high-impedance guides correspond to lower frequencies at a given wave number (and therefore, lower phase velocity).

4.2.4 Applications

Anisotropic waveguides have multiple applications that are not possible using isotropic guides. One advantage of anisotropic waveguides is that they can be designed to propagate surface waves in one direction while being invisible to surface waves incident from a perpendicular direction. This effect is demonstrated by Figure 4.11 and Figure 4.12. A scalar impedance Z_2=j133Ω is placed on the surface in the outer regions. In the inner guided region, the impedance in the propagating direction is Z_{prop}=j399Ω, and the impedance in the transverse direction is Z_{trans}=j133Ω (equal to the outer region). Waves can propagate losslessly along the guide (Figure 4.11). When a wave travels perpendicular to the guide (Figure 4.12), the transmission properties are not affected by the presence of the guide. In Figure 4.11 the fields present outside the guide are due to mismatch with the excitation source (not shown). When the excitation source is not perfectly matched to the guided mode, energy can leak into other modes on the surface, plane waves above the surface, or reflected waves back into the feed. However, none of the energy that enters surface modes in the guide leaks out.

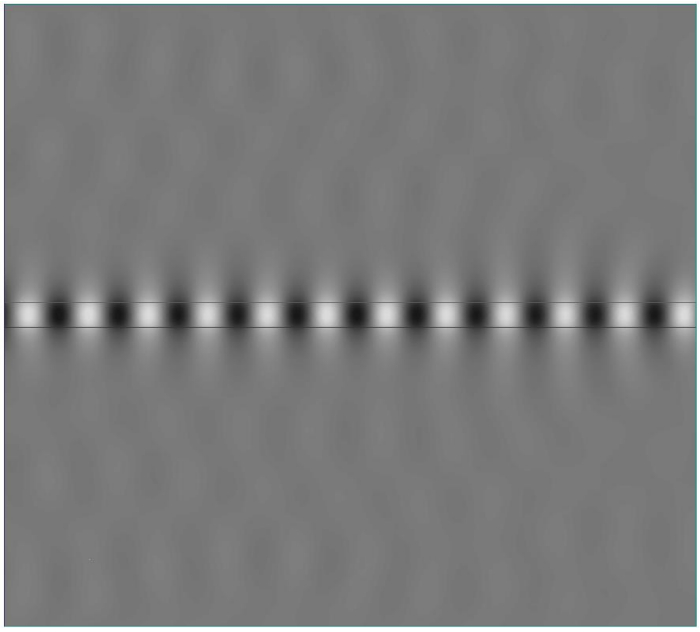

Figure 4.11: Anisotropic waveguide with wave propagating in the guide. Wave power outside the guide is due to mismatch between the feed mode and the guide mode.

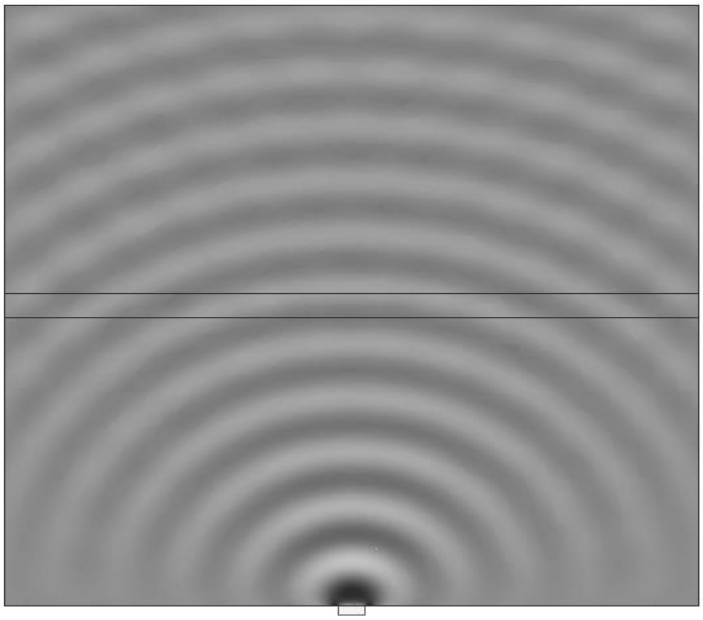

Figure 4.12: Anisotropic waveguide at orthogonal incidence. The wave does not interact with surface wave incident from a perpendicular direction. The guide structure is identical to that of **Figure** 4.11.

Next we will demonstrate the ability to arbitrarily set phase velocity, v_p, and group velocity, v_g, in an anisotropic surface waveguide. The phase and group velocities are defined as ω/k and $\partial\omega/\partial k$ respectively, where k is the surface wavenumber. For a given impedance tensor and guide width, v_p and v_g can be calculated numerically from the dispersion relation (4.7). Figure 4.13 shows that there are multiple impedance tensors to implement a desired v_p for a given frequency and fixed guide width. Each of these impedance tensors has different v_g. The guide is oriented along a major axis of the impedance tensor, and the tensor is therefore diagonal. Dispersion curves for the impedance tensors labeled in Figure 4.13 are shown in Figure 4.14. The dispersion curves cross at f_0=10 GHz, and v_p=0.8c at this point. Only one value of v_g can be obtained using an isotropic surface impedance. Anisotropy allows v_p and v_g to be set independently. Similarly, by using tensor impedances, v_p and v_g can be held constant as the guide width is swept.

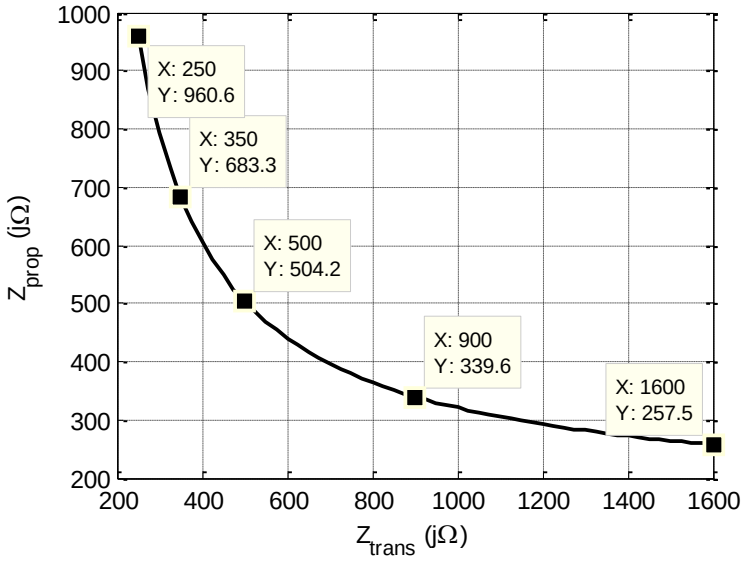

Figure 4.13: Impedance tensor values for constant phase velocity. The guide has width d=10mm, f_0=10GHz, outer region impedance Z_2=j133Ω, and desired phase velocity v_p=0.8c. Off-diagonal impedance tensor values are set to zero. The isotropic value of the curve is at Z_{prop}=Z_{trans}=j502.4Ω. Dispersion curves for the labeled tensors are plotted in Figure 4.14.

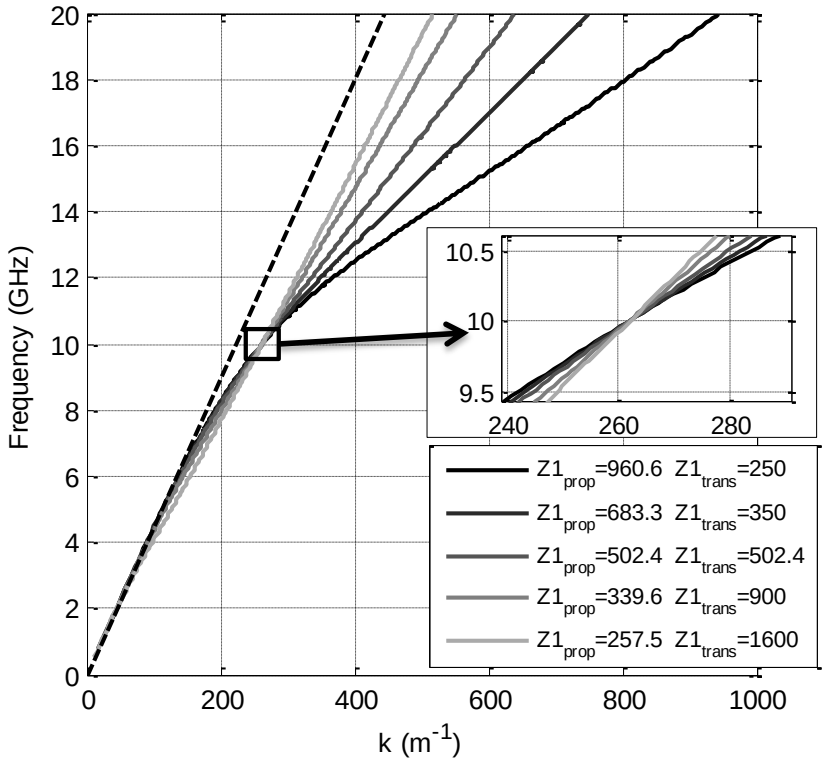

Figure 4.14: Dispersion plots for constant phase velocity. The guide has width d=10mm and outer region impedance Z_2=j133Ω. The impedance values give a phase velocity of 0.8c at 10GHz. The dispersion curves cross at 10 GHz giving identical phase velocities. The group velocity is the slope of the dispersion curve at this point.

Figure 4.15 shows the tensors that give a desired v_p and v_g for a range of guide widths. The propagating impedance remains fairly constant, and transverse impedance declines as the width of the guide increases. The dispersion curves for the tensors labeled in Figure 4.15 are shown in Figure 4.16. The dispersion curves are nearly identical for each tensor, and the plots lie overlaid on each other such that only one line is clearly visible over the entire range. Since the tensors have the same dispersion relation, each tensor will have equal v_p and v_g at any frequency. However, both v_p and v_g change with frequency.

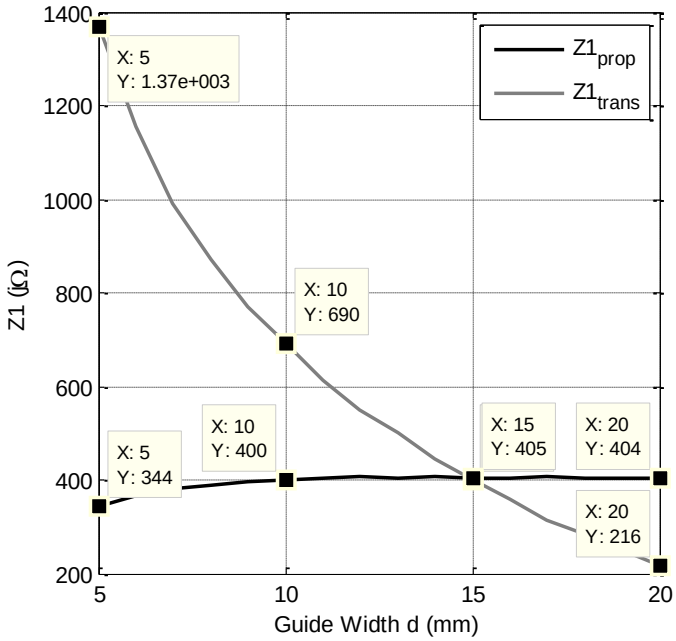

Figure 4.15: Impedance tensor values for v_p = 0.8c and v_g = 0.65c. The solution is for f_0=10GHz, and outer impedance Z_2=j133Ω. Dispersion plots for the labeled tensors are shown in Figure 4.16.

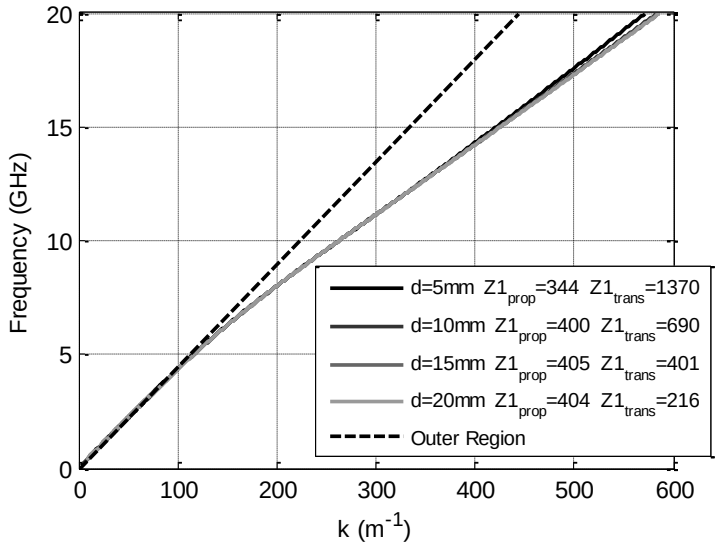

Figure 4.16: Dispersion plots for the tensors labeled in Figure 4.15. The tensors were solved such that v_p=0.8c and v_g=0.65c at f_0=10GHz and outer impedance Z_2=j133Ω. The tensors have nearly identical dispersion curves and the plots lie overlaid on each other. Therefore, these tensors will have equal v_p and v_g at any frequency (although the desired values of v_p = 0.8c and v_g = 0.65c will only occur at f_0=10GHz).

Using the theory, three surface waveguide structures were simulated in HFSS with the results shown in Figure 4.17. The left-most guide has a constant width of 20mm. The center guide has a varying width from 5-20mm in an hourglass shape. The impedance of this guide is varied so that the phase and group velocity remains constant and identical to the constant-width guide. The far right guide has the same hourglass shape but with a constant impedance identical to the straight guide. Figure 4.17 shows the electric field component normal to the surface where light is positive values and dark is negative values. Black lines are added in order to compare the phase fronts in each guide. We can see that the constant width guide and the hourglass guide with correctly chosen impedance have the same phase fronts over the entire length of the guide. The hourglass guide with constant impedance has phase fronts different from the others. The impedance of the left guide is set so that v_p=0.8c and v_g=0.65c. In the center guide, the range of v_p is from 0.798-0.802c, and the range of v_g is from 0.62-0.68c. Errors are caused by approximations in the theory and simulations as described below.

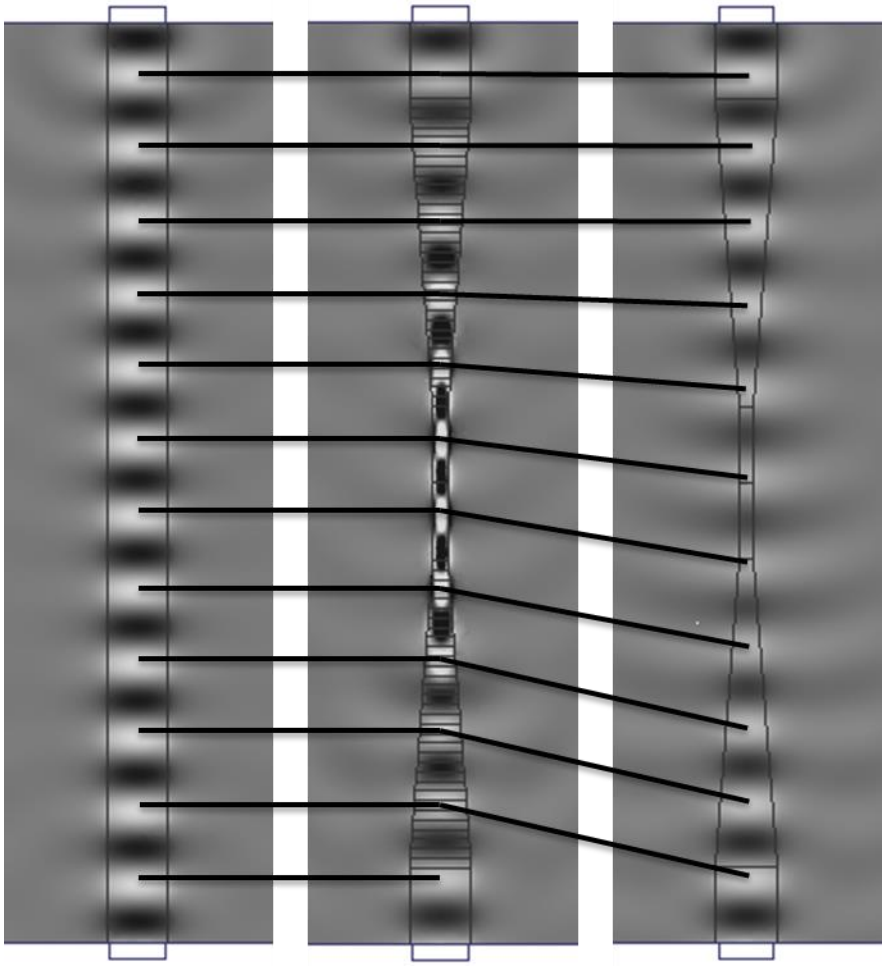

Figure 4.17: Anisotropic waveguides with propagating waves in the guides. In each case the outer impedance is Z_2=j133Ω, the guiding region is 300mm, the air height is 100mm, and the width outside is 100mm (not shown to scale).

The impedance values in the simulation were adjusted from the theory in order to obtain optimal simulated results. These adjustments account for errors in ray optics theory and assumptions made to simplify the waveguide dispersion equations. The narrow waveguide sections required the largest modifications. The theoretical impedance tensor values for these structures are plotted in Figure 4.15. Impedances were adjusted from their theoretical values to ensure that v_p=0.8c. By focusing specifically on v_p, v_g deviates from its desired value of 0.65c. However, an exhaustive search of impedance tensors would allow arbitrarily accurate v_g solutions.

4.2.5 Conclusion

A simple theoretical model for an impedance surface waveguide was developed using a ray optics method and tensor impedance surface theory. A unit cell was also designed in HFSS that can model tensor impedance surfaces. This unit cell was used to simulate a novel tensor surface impedance waveguide structure. The simulations matched the theory over a wide range of tensors and over multiple propagation modes. Two applications of anisotropic waveguides were investigated. In one example, an anisotropic waveguide was able to guide waves in one direction and let them pass through in another. In a second example, a guide had its width changed but it maintains constant phase velocity and group velocity. In future work we plan to extend surface waveguide theory to real tensor impedance surfaces formed from metal patches patterned on grounded dielectric substrates. In these structures, the theory still applies, but frequency dependent surface impedances must be accounted for. Waveguides with TM guiding regions and TE exterior regions could be investigated as well.

4.3 Realized Artificial Tensor Impedance Waveguides

In this section, a tensor impedance surface waveguide, as analyzed in Section 4.2 is realized. An idealized illustration of a transparent waveguide is shown in Figure 4.18. The impedance surface is built as a printed circuit. These structures are created by patterning metal on the top layer of a grounded dielectric slab. The waveguide is designed with square and rectangular unit cells as shown in Figure 4.19. These unit cells have been analyzed along their principal axes [33]. Further analysis of printed circuit tensor impedance surfaces has also been performed, and it was found that tensor impedance boundaries do not always accurately model printed structures, and more-accurate models have been proposed [26, 27, 44]. However, currently these methods can only be applied to individual unit cells, and not large structures like waveguides. In order to confirm the accuracy of the ideal tensor impedance model, we have compared this ideal model to simulations of printed circuit structures and measurement.

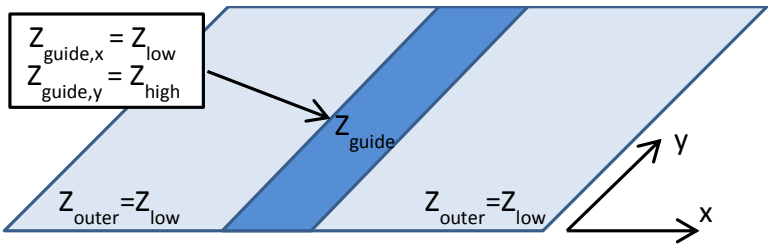

Figure 4.18: Model of transparent surface impedance waveguide. A high impedance region is surrounded by two lower impedance regions. Guided surface wave modes can propagate along the higher impedance region. In the opposite direction the impedance of the guiding and outer regions match.

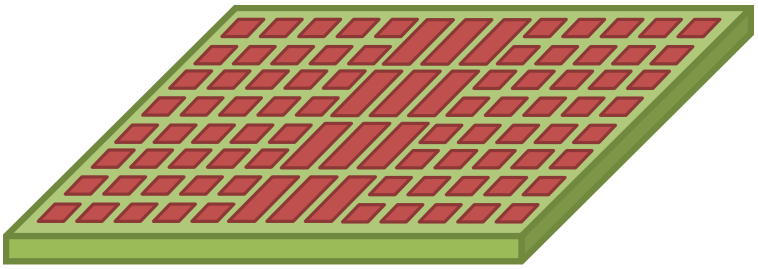

Figure 4.19: Physical representation of surface wave waveguide. A grounded dielectric substrate is patterned with rectangular and square patches. Higher impedance is achieved using the elongated rectangular patches.

4.3.1 Theoretical Dispersion of Realized Waveguide

In Section 4.2.1 the theoretical dispersion was solved for an ideal tensor impedance waveguide using planar boundary conditions. In this analysis the impedance surface was assumed to be dispersion free. Realized impedance surfaces have dispersion and the theory must be generalized to allow frequency-dependent impedance as shown below:

$$-\left[\frac{\pi m+\varphi(\theta,\omega)}{d}\right]^2+\frac{n_1(\theta,\omega)^2\,\omega^2}{c^2}\sin^2\theta=0\,. \tag{4.8}$$

where m is the mode number, $\varphi(\theta,\omega)$ is the phase shift on reflection of the rays in the guide, d is the width of the guide, $n_1(\theta,\omega)$ is the effective surface impedance of the interior region, ω is the angular frequency of the mode, θ is the direction of propagation, and c is the speed of light. The phase shift depends the index, $n(\theta,\omega)$, and impedance,

$Z(\theta,\omega)$, of the interior and exterior regions of the guide. The surface impedance is frequency dependent, but when applying the theory, a harmonic excitation is assumed. Therefore, the dispersion relation is solved independently at each frequency, and single impedance tensor is used for each solution.

To apply the theoretical model, the frequency dependent impedance, $Z(\theta,\omega)$ must be known ahead of time, along with the corresponding index $n(\theta,\omega)$. In this paper, the rotation and frequency dependence of the unit cells are determined by simulation and these values are applied to the theoretical model. These simulations are described below in Section 4.3.2. Along with frequency dispersion, realized impedance surface exhibit spatial dispersion. This phenomena has been analyzed for patch-type unit cells with no vias [26, 27]. Spatial dispersion implies an inconsistency between the predicted anisotropy as defined by (2.9), and the actual anisotropy of the unit cell. This inconsistency causes errors in $Z(\theta,\omega)$ and $n(\theta,\omega)$, but it will be shown in Sections 4.3.2 and 4.3.3 that ideal theory can still accurately model the waveguide dispersion.

4.3.2 Unit Cell Analysis

The unit cells for the waveguide used a 1.27mm thick Rogers 3010 substrate (for simulations we used the design dielectric constant ε_r = 11.2). This substrate has the highest dielectric constant of commonly available printed circuit board materials, and the largest standard thickness. Higher dielectric constants and larger thickness have been shown to allow broader bandwidth anisotropy [52]. The dimensions of the rectangular unit cell for the guiding region are shown in Figure 4.20a, and the isotropic unit cell for the outer region is shown in Figure 4.20b. Both unit cells have gaps between the metal patch and the edge of the unit cell that are identical on all four sides.

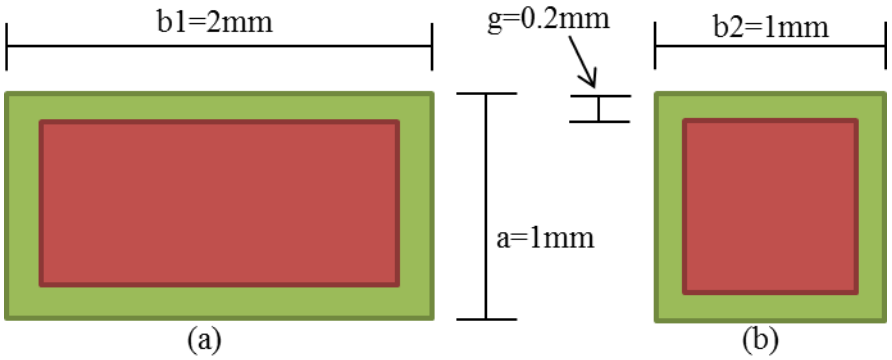

Figure 4.20: Unit cell dimensions. The illustrations are for (a) anisotropic unit cell and (b) isotropic unit cell. For both unit cells the substrate is a grounded dielectric with a metal patch. The patch is represented by the inner rectangle, and the distance between the patch and the unit cell edge is g=0.2mm on all sides. The anisotropic unit cell is of 2x1mm and the isotropic unit cell is 1x1mm.

Figure 4.21 shows the dispersion relation of each unit cell for waves traveling along the principal axes of the cell. The dispersion was simulated using the eigenmode solver of Ansys HFSS version 15. Surface impedance curves are shown in Figure 4.22. For the isotropic 1x1mm unit cell, the impedance along the two principal axes is identical because the unit cell is square. The 2x1mm unit cell has different impedance for each axis. The impedance along the 1mm dimension of the rectangular cell is nearly-identical to the 1x1mm unit cell (as also demonstrated in [33]). The fact that the square unit cell and the short direction of the rectangular unit cell have the same surface impedance is what allows the waveguide to be transparent in orthogonal directions. The larger impedance along the propagating direction of the rectangular unit cell allows waveguide modes to be confined to the interior region

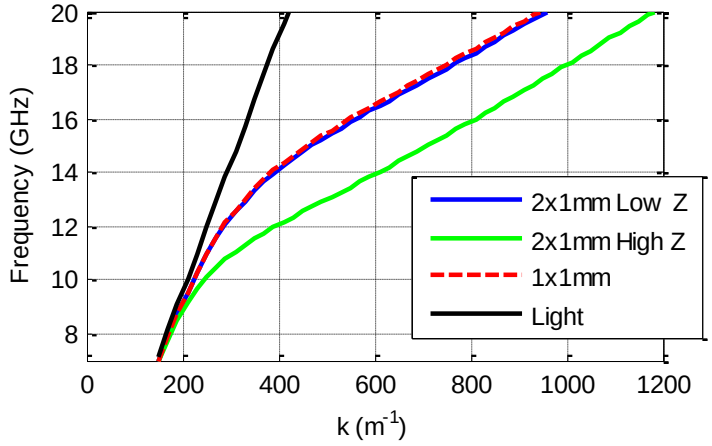

Figure 4.21: Dispersion relation for anisotropic and isotropic unit cells. The low impedance direction of the anisotropic unit cell has nearly identical dispersion to the isotropic unit cell. In the high impedance direction is lower in frequency at any given wavenumber.

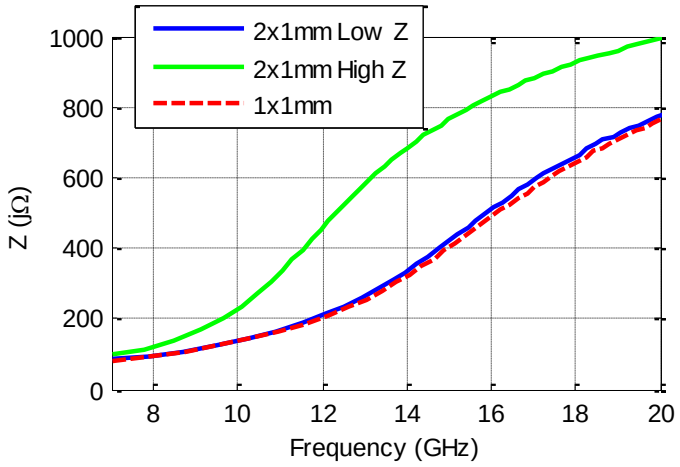

Figure 4.22: Surface impedance vs. frequency. The results are for the principal directions of anisotropic and isotropic unit cells. The low impedance direction of the 2x1mm unit cell has the same impedance relation as the 1x1mm unit cell.

Figure 4.21 and Figure 4.22 show anisotropic behavior for the principal axes of the 2x1mm unit cell, but it is also necessary to verify the performance of the unit cell for waves propagating at directions between the principal axes. For ideal tensor impedance boundary conditions the dispersion for the principal axes is sufficient to calculate the dispersion at any other angle. However, on realized surfaces, spatial dispersion [26, 27],

and mode interference [52], can distort propagation between the principal axes. The dispersion relation for multiple propagation directions has been simulated for both isotropic and anisotropic unit cells. Isofrequency index contours for the isotropic unit cell are shown in Figure 4.23a. For the isotropic unit cell the contours are circular because the index has the same value for any propagation direction.

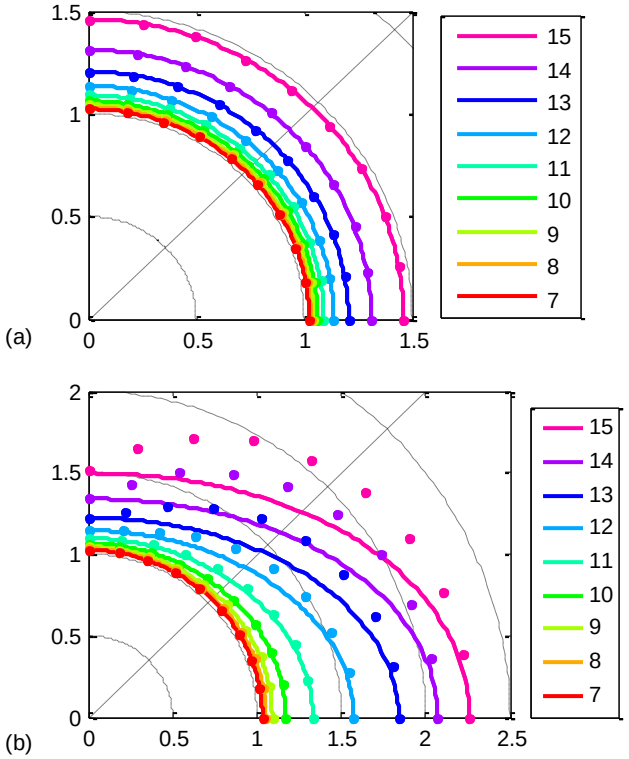

Figure 4.23: Isofrequency impedance contours. The results are for (a) isotropic unit cell and (b) anisotropic unit cell. The radial direction is effective index and the theta direction is the direction of propagation. Theoretical curves are shown as solid lines and simulations are the dots. The legend labels different frequencies with units of GHz. The contours are symmetric across the x- and y-axis so only the first quadrant is plotted. Ten rotations from 0-90° are simulated.

Isofrequency contours for the 2x1mm unit cell are shown in Figure 4.23b. Results from simulation are plotted as dots. Theoretical curves are shown as solid lines, and are calculated using the results of the principal axis simulations at each frequency. The principal axes are oriented along the *x*- and *y*- axes where the *x*-axis (high impedance) corresponds to a wave propagating along the 2mm dimension of the unit

cell and the *y*-axis (low impedance) corresponds to the 1mm dimension. At low frequencies the ideal theory and simulation match but as frequency increases the simulation deviates from the theory. The cutoff of the TE mode is at 12.3 GHz, and it has been shown that this is where the ideal tensor impedance theory is no longer valid [52]. Above the cutoff frequency the simulation rapidly deviates from the theory with the worst estimation generally occurring around a propagation angle of 45°. At 12 GHz, 13GHz, 15 GHz, the index is off by 6%, 12%, and 15% respectively for a wave propagating at 45°. This error is similar at higher frequencies but other angles begin to have large error also due to mode distortion.

Although the unit cell dispersion curve deviates from the simple single-mode theory, especially above the TE cutoff at 12.3GHz, the guide is oriented along the principal axis of the unit cell. In this orientation, the wave is propagating along the direction that does not deviate as significantly from the theory. In Section 4.3.3, it is found in both simulation and experiment that the waveguide operates above 12.3 GHz consistently with impedance surface theory.

4.3.3 Waveguide Dispersion and Fields

The dispersion of a waveguide is tested using measurement, simulation, and the theoretical model. For each case, the width of the waveguide is set to d=10mm. In general, wider guides bend the dispersion relation to lower frequencies, and lower the cutoff frequency of higher order waveguide modes.

A. Measured Dispersion Setup

A surface wave waveguide was constructed using the unit cells analyzed in Section 4.3.2. The total size of the board was 16×10 inches and the waveguide was 16 inches long centered on the board with a 10mm wide guiding region (10 unit cells wide). A photograph of a section of the waveguide is shown in Figure 4.24. A near field scanner was used to make the dispersion measurement. The dispersion was obtained from the phase velocity of the mode in the waveguide. The measurement setup is shown in Figure 4.25. The feed is a trapezoidal sheet of Rogers 5880. An end-launch SMA

adapter is attached to the back of the feed and leads to one port of an Agilent E5071C Vector Network Analyzer (VNA). The second port of the VNA is attached to a probe that is scanned across the surface. The probe tip is 5mm long and oriented vertically approximately 2mm above the surface. For dispersion measurements the probe is scanned along the center of the guide at 200μm increments. At each position, S21 phase is measured by the VNA, and this data is used to calculate phase velocity. The effective surface index is calculated from the phase velocity, and this index is used to derive the dispersion of the waveguide

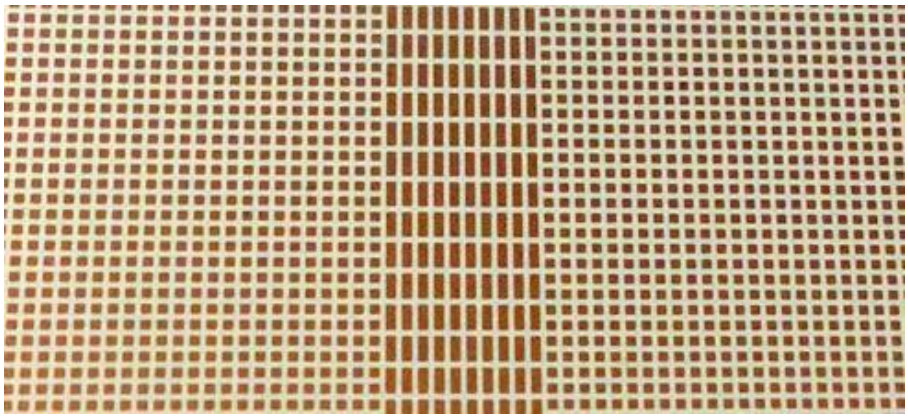

Figure 4.24: Photograph of tensor impedance surface waveguide.

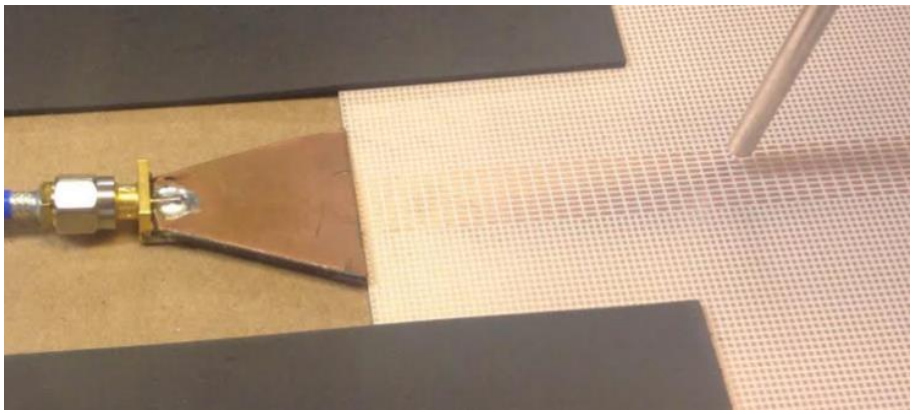

Figure 4.25: Measurement setup for waveguide. Magnetic absorbers are place to the sides of a trapezoidal feed. A vertical probe is located in the upper right side of the photograph. Photograph of tensor impedance surface waveguide.

The feed does not couple perfectly into the guided surface mode and some power

is reflected or launched as surface waves in the outer region. However, waves excited into a guided mode do not spill outside the guiding region, and the feed is designed so that minimal fields are excited outside of the waveguide mode at the center of the operating region. For printed circuit structures, other surface wave excitations have been used such as a Yagi-like surface wave launcher [26, 27], and a flared microstrip line [4, 28]. These could allow better coupling efficiency into the waveguides. However, for this study, the discrete trapezoidal surface wave launcher allowed the convenience of moving the feed to launch a guided wave, or to launch waves at other positions or angles on the surface. Two sheets of magnetic absorber (Arc-Tec DD11006) were placed on either side of the feed to limit the amount of power reflected back into the guide from the outer region. Both TM and TE modes are absorbed, and the modes are dissipated both above and within the substrate. Magnetic absorber is also used to terminate the guided mode and prevent reflections back into the guide. A well-matched surface wave launcher could also be used to terminate the mode into a 50Ω load.

B. Simulated Dispersion Setup

The dispersion of the waveguide was simulated using the eigenmode solver in Ansys HFSS version 15. The model used ideal tensor impedance boundary conditions. Because of dispersion in the realized surface, the impedances are set differently for each frequency as stipulated by Figure 4.22. The simulation setup is described in Section V of [14], except this paper uses the anisotropic impedance boundary condition (instead of the checkerboard structure), which has been implemented in the HFSS eigenmode solver in the time since the previous publication. The waveguide simulation was performed over the range where the unit cell was simulated: 7-20 GHz (as seen in Figure 4.22). The impedance data was interpolated to obtain the values at 1 GHz increments.

C. Theoretical Dispersion

The theoretical dispersion relationship is described by 4.8 and fully derived in [14]. As noted in Section 4.3.1, the impedance of the unit cell must be solved before the theoretical dispersion can be solved, and this impedance is dependent on both frequency

and propagation direction. The impedance relation for the principal axes is shown in Figure 4.22. Even though the guided wave travels along the principal axes of the impedance tensor, the impedance at intermediate angles must be known to correctly apply the ray optics theory. For intermediate angles, the impedance values were obtained using two different methods (each are plotted in Figure 4.23). The first method used simulated impedances for the principal directions and derived other angles by assuming an ideal tensor impedance boundary. The second method used simulated values from each of the intermediate angles exactly. Both methods are compared to measurement and simulation in the following section.

D. Dispersion Results

The results for each dispersion method are shown in Figure 4.26. The measured dispersion closely matches simulation and theory. Only the lowest mode can be measured, and the results stop at 15 GHz. Above this frequency data is difficult to obtain. At higher frequencies, the impedance of the unit cells go up and waves are more tightly bound to the surface. The measurement probe is scanned 2mm above the surface, and if significant wave power is located below this height it becomes difficult to obtain an accurate measurement. Also, at higher frequencies, higher order guided modes are supported and dual mode operation occurs. In the fabricated structure, the 2^{nd} order mode is predicted by theory at 14.5 GHz. When two (or more) modes are present, it becomes difficult to determine the phase velocity of any single mode due to interference between the modes. In simulation and theory single mode operation can be strictly enforced, and the dispersion curves can be extended to higher frequencies than can be measured experimentally.

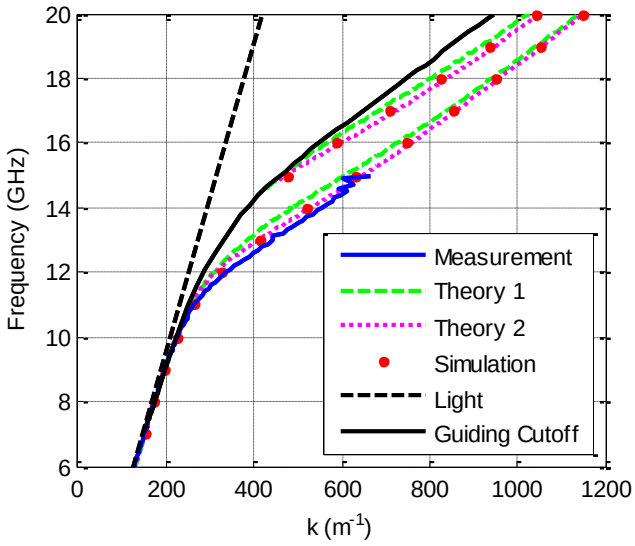

Figure 4.26: Dispersion of guided modes in tensor impedance surface waveguide. Only the lowest mode can be measured and this is shown as a solid line. The first two modes are shown as dashed lines for the theoretical solutions, and as dots for simulation. The first theory curve uses ideal tensor impedance theory to obtain impedance at intermediate angles and the second theory curve uses simulation to get these values. A black dashed line is the dispersion of light in a vacuum. Guided modes must lie below the dispersion relation of the outer region, and this is shown as a black line.

Simulated and theoretical curves are shown up to 20 GHz for the first two guided modes. The second mode has a cutoff when it intersects the dispersion curve of the outer region. The outer region dispersion represents the highest phase velocity that can be achieved in the guide, as this outer region has lower index than the interior region. Two theoretical methods were used as described in the previous section. The maximum difference in frequency between the two theories is less than 0.4GHz for either mode (<3%). Therefore, results show that the simplified theory assuming an ideal tensor impedance boundary is sufficient to predict the approximate dispersion relation. The second method using the simulated impedances is slightly more accurate but requires many more simulations

E. Field Profile of Guided Mode

The fields for the guided mode were measured and compared to simulation. The

fields for ideal impedance boundary conditions were shown in [14]. A dispersive structure using the rectangular unit cells is analyzed here. The model is constructed identically to the experimental model with 10 unit cells across guiding region and 50 unit cells on across the isotropic region on each side. The electric field magnitude is shown for the first two guided modes in Figure 4.27. The guiding region is marked as a dashed line, and the mode is propagating into the page. The fields are most highly concentrated between the patches. For both modes the field has sinusoidal variation across the guiding region and exponential decay to the sides away from the guide. Field decays exponentially above the substrate across the entire width of the structure.

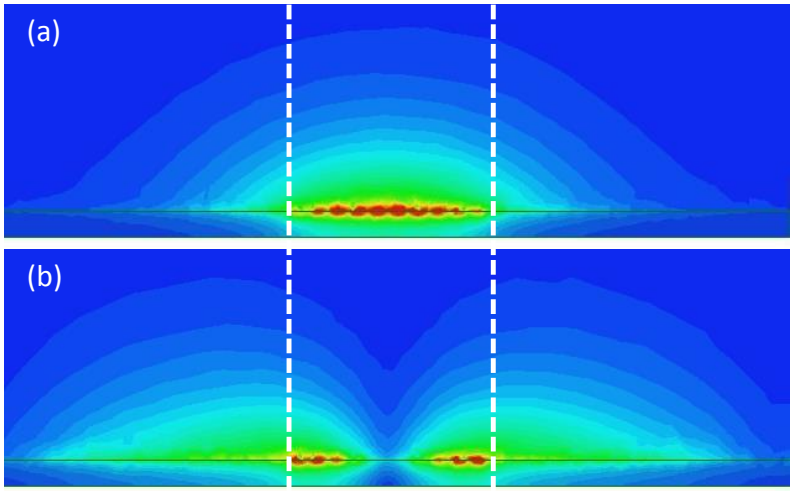

Figure 4.27: Normalized electric field magnitude. The plots show (a) 1st mode, and (b) 2nd mode for a simulation of a surface waveguide.

Using the same experimental setup as for dispersion, a probe was scanned across the guide orthogonal to the direction of propagation. The probe was again placed 2mm above the surface and measurements were taken at 200μm increments. The power at each point was measured at 12 GHz and this was transformed to a normalized field magnitude which is plotted in Figure 4.28. An equivalent line from the simulation was also plotted in Figure 4.28, and the normalized fields can be compared. Within the guided region the simulated and measured responses are nearly identical and have a sinusoidal profile. Outside the guide the field decays exponentially with distance. The minor differences in field magnitude are likely due to the energy excited outside the

guide. Only the first mode can be measured in this manner because a pure second mode cannot be experimentally excited. The impedance contrast between regions effects the confinement of the mode with larger contrasts more closely confining modes to the guiding region. Wider guides also have more mode confinement.

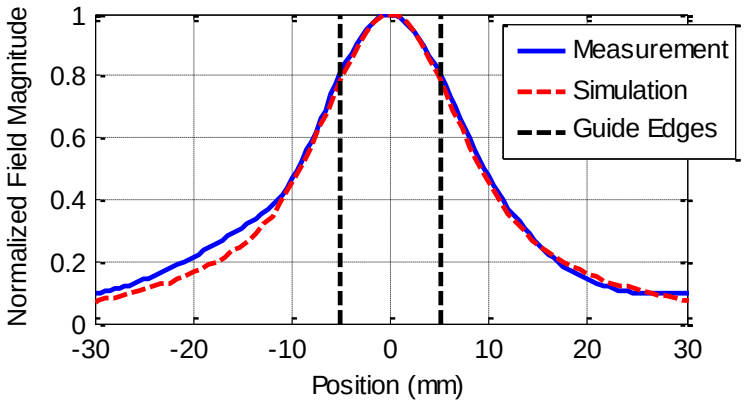

Figure 4.28: Normalized electric field magnitude above waveguide.

4.3.4 Near Field Measurements

Two-dimensional near field measurements were obtained using the setup described in Section 4.3.3. The total size of the surface was 10×16 inches. The measured area is slightly smaller than the total board size to allow space for the feed and absorbers around the edge of the surface. The excitation source, shown in Figure 4.25, does not couple perfectly into guided modes at all frequencies, and some power is excited directly to the outer region. A vertical probe was swept 5mm above the surface along a 2mm grid. The probe was scanned higher above the surface for two-dimensional field measurements because the surface was not completely flat and scanning lower could cause contact between the probe and surface at the edges. Each measurement contains about 25,000 points, and normalized field results at 11 GHz are shown in Figure 4.29.

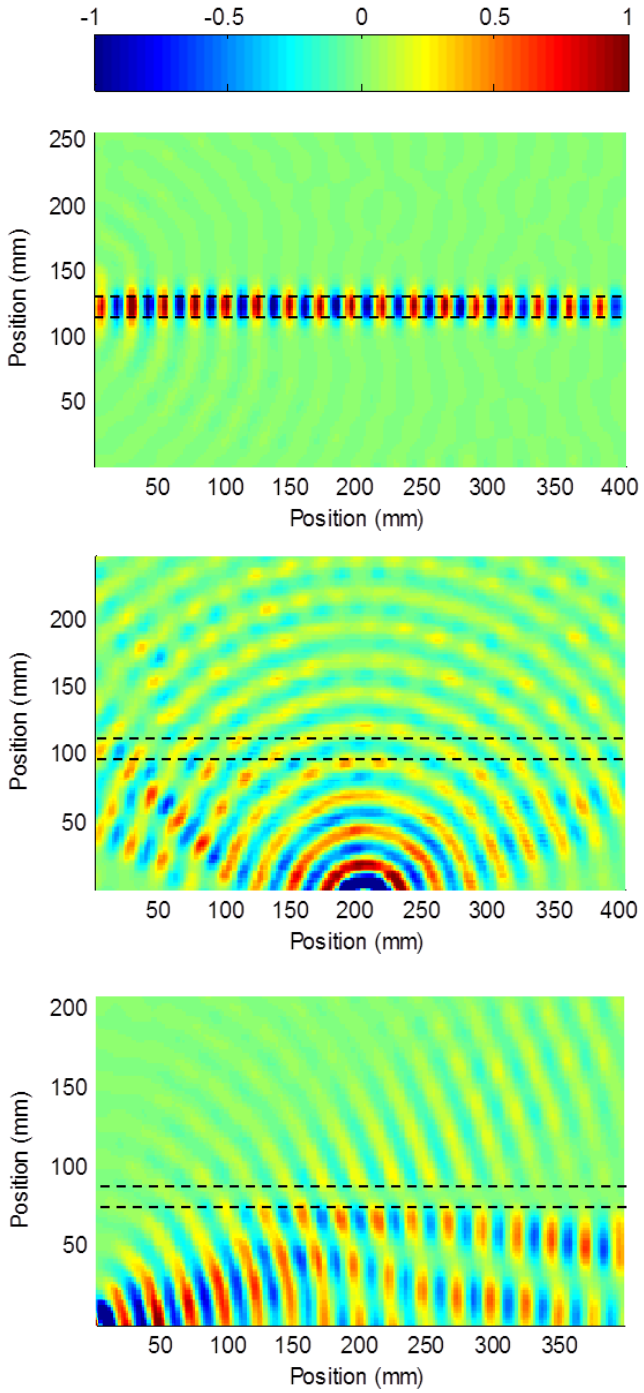

Figure 4.29: Measured fields. The plots show normalized vertical (out of page) electric field at 11 GHz for (a) guided mode, (b) orthogonal mode, and (c) angled mode. Fields in (a), (b), and (c) are not plotted to the same scale.

A guided mode is displayed in Figure 4.29a. The mode is bound near the guide and does not leak to the outer region. The measured bandwidth for guided modes is from 9.4-15.2 GHz. Below 9.4GHz the measured mode is a regular surface wave (not confined to the guiding region) because the impedance inside and outside the guide is almost identical. At 11 GHz, as shown in Figure 4.29a, almost all of the fields are in the waveguide mode and minimal fields are present in the outer region. Above 14 GHz, the source excites more measurable fields in the outer region than as a guided mode. This is because higher frequency modes have high impedance. High impedance modes are tightly bound to the surface, and this is difficult to measure because the probe is scanned 5mm above the surface (in order to avoid scratching the material). At higher frequencies, modes excited in the outer region (which still has lower impedance) are measured much more easily because they are not as tightly bound. These outer-region modes can reflect off the edges of the board and travel back across the waveguide making it difficult to isolate the guided mode which exists mostly below the probe. However, power that does enter as a guided mode does not leak away from the guide.

Figure 4.29b shows a two-dimensional field plot for a surface with a feed located in the exterior region. The feed was a vertically-oriented monopole that excited semi-circular phase fronts on the surface. The guiding and outer regions have identical surface impedance for surface waves incident normal to the guide. Therefore, as seen in Figure 4.29b, waves at normal incidence pass through the guide as if it were not present, and transparency is confirmed. In this case, the wave front is only orthogonal directly above the source. At off-normal angles, some reflections and distortion can be seen off the guide. In Figure 4.29c the trapezoidal feed is used to launch a surface wave toward the waveguide at a small grazing angle. In this case, the higher-impedance guiding region reflects a significant portion of the incident power.

4.3.5 Curved Waveguide

A transparent curved waveguide was designed and measured, and Figure 4.30a illustrates a schematic diagram for the surface. The outer region has small isotropic surface impedance, analogous to Figure 4.18, and the guiding region is curved around a

point located at the corner of the structure. The guiding region has anisotropic impedance with the radial direction equal to the outer region. The high impedance direction is along the angular dimension of the guide. The design supports guided waves along curve, and waves traveling from a point source at the center of curvature pass across the guiding region without reflection or alteration.

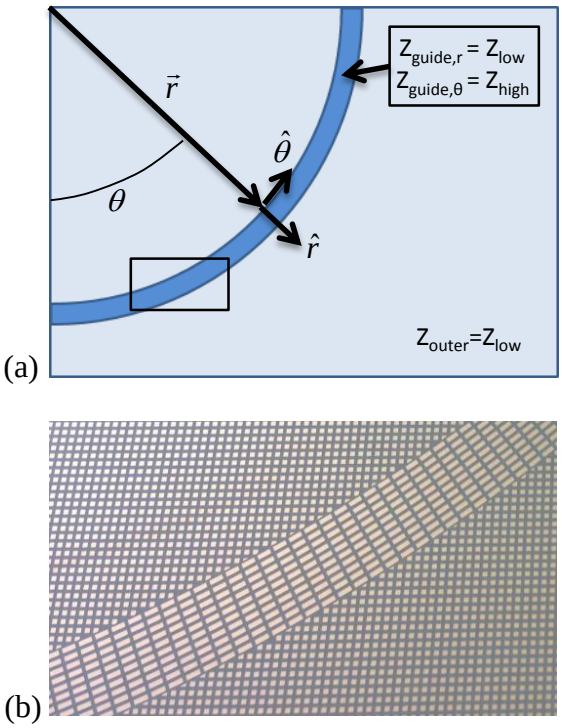

Figure 4.30: Curved waveguide diagrams. A schematic of the waveguide dimensions and impedance is shown in (a). A photograph of the fabricated waveguide is shown in (b). The rectangular box in (a) is the location of the photographed region shown in (b).

A photograph of a section of the fabricated guide design is shown in Figure 4.30b. The outer region unit cells are identical to those in the straight design (shown in Figure 4.20). The anisotropic unit cells are distorted slightly due to the curvature. The design stipulates 2mm unit cell length along the guiding direction. The unit cells are constructed such that they all have the same angular length, and the unit cell length at the radial center of the guide is set to exactly 2mm. On the inner edge of the guide, the side length is 1.98mm. Similarly, on the outer edge, the side length is 2.02mm. Below

20 GHz, simulation shows that the deviation from the surface impedance of a 2mm-long unit cell is less than 1%. All unit cells are exactly 1mm in the radial direction. For the outer region, the unit cells form a 1x1mm grid. These unit cells are removed in the region where the guiding region intersects. As seen in Figure 4.30b, unit cells near the edge of the guide are cut so there is no overlap between unit cells.

The width of the guiding region is 10mm, as was the case for the straight waveguide. The radius from the center of curvature to the center of the waveguide was 8 inches. The substrate material and dimensions are the same as before, and near field measurements were obtained from the same system used for the straight waveguides. The guided mode was fed using the straight waveguide as a source. The trapezoidal feed shown in Figure 4.25 fed the straight waveguide on one end, and the opposite was pressed up to the curved waveguide. Figure 4.31a shows a guided mode at 11 GHz. This was the frequency that had the best match between the trapezoidal feed and straight waveguide mode. However, for the curved case the guided mode leaks into the outer region. Figure 4.31b shows the same structure at 12 GHz. In this case there is minimal leakage from the guided mode. The measured bandwidth for guiding without leakage is from 11.7-15 GHz. Bending losses are analyzed in Section 4.3.6.

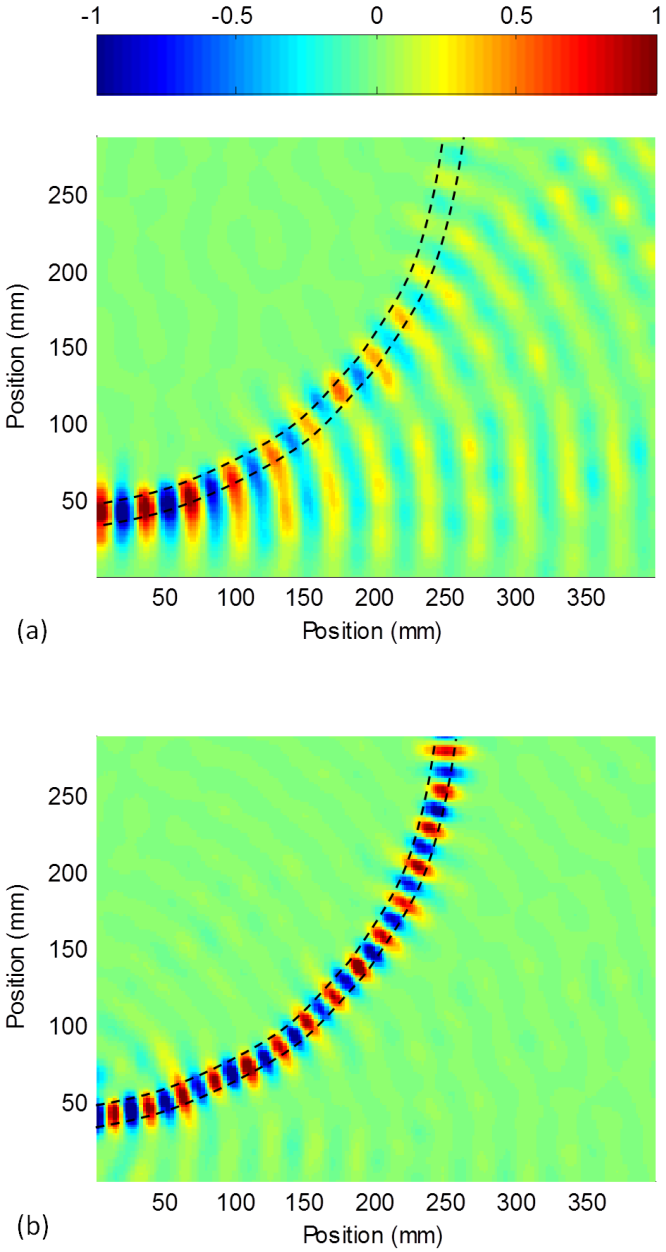

Figure 4.31: Measured fields of curved waveguide. The plots show normalized electric field for guided mode at (a) 11 GHz , and (b) 12 GHz. Fields in (a) and (b) are not plotted to the same scale.

The curved waveguide was also measured at an orthogonal direction. A vertical probe was set at the center of curvature of the guide which is located at the corner of the surface. Magnetic absorber is placed along the edges of the surface to ensure that there

are no reflections back into the surface. The source radiates circularly from the center of curvature of the guide such that the wave is incident normally to the guide across the entire structure. The field plot at 12 GHz is shown in Figure 4.32. The wave passes through without reflection again confirming the transparency of the guided region. The fields along the edges are reduced because magnetic absorber is placed along these sides.

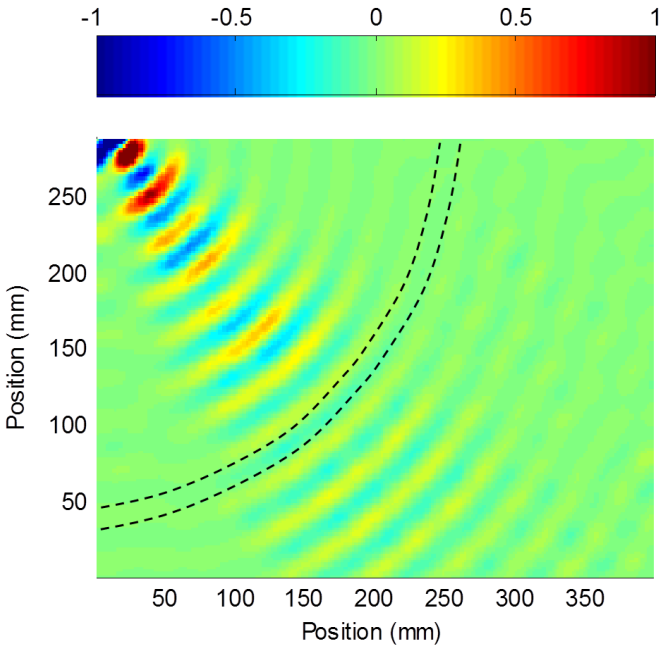

Figure 4.32: Measured field of orthogonally incident mode. The plot shows normalized vertical electric field at 12 GHz.

4.3.6 Analysis of Bending Loss

As mentioned in Section 4.3.5 and seen in Figure 4.31, the curved waveguide exhibits bending loss that depends on the frequency, waveguide dimensions, and surface properties. This phenomena also occurs for bending of dielectric slab and fiber structures [53]. Leakage occurs at bends because the mode on the exterior of the curve must travel faster than at the center in order to stay in phase. Leakage occurs where this speed is larger than what can be supported by the materials. Ray optics has been used to analyze dielectric slab waveguides and fibers to determine the bending loss of a

multimode structure [54-57]. This method can be adapted for the surface wave waveguide in order to predict the bending loss due to radiation from a curved waveguide.

For straight waveguides, the ray optics guiding condition dictates that the rays exhibit total internal reflection at the interface between the guiding region and the outer region. This total internal reflection is frustrated by bending and curved waveguides never exhibit total internal reflection [56]. However, the bending loss can be negligible depending on the setup of the waveguide. The setup for the curved waveguide analysis is shown in Figure 4.33. A straight waveguide of width 2ρ feeds a curved waveguide with the same width and surface properties. The dispersion relation of this straight waveguide is solved using (4.8), and the incidence angle of the ray in the straight waveguide, θ, is obtained from this equation. The curved waveguide has a center radius of R. The height of the ray crossing between the straight and curved sections is r. The incidence angle at the inner and outer dimensions can be obtained geometrically as follows [57]:

$$\theta_i = \cos^{-1}\left(\frac{r}{R-\rho}\cos\theta\right), \tag{4.9}$$

$$\theta_o = \cos^{-1}\left(\frac{r}{R+\rho}\cos\theta\right). \tag{4.10}$$

The incidence angle on the outer surface is always larger than on the inner surface. Rays only lose power on the outer surface, and losses on the inner surface are negligible [56]. The angular dimension of the guide is ϕ, and $\Delta\phi$ is the angular length between successive reflections on the outer diameter.

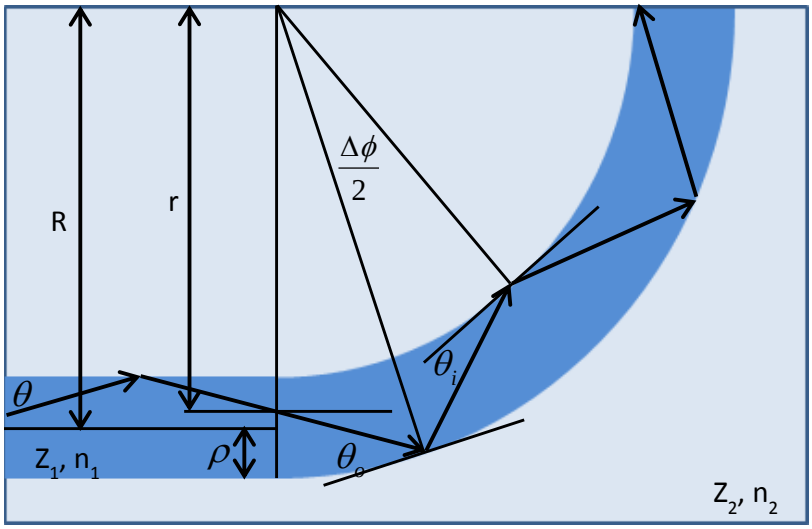

Figure 4.33: Setup for ray optics analysis of curved waveguide.

Power dissipates exponentially as a function of the angular size of the waveguide. The dissipation is calculated by integrating over each incidence height *r*:

$$P(\phi) = \int_{R-\rho}^{R+\rho} P_0 \exp(-\gamma\phi) dr \,, \tag{4.11}$$

where P_0 is the initial power, and γ is the attenuation coefficient. In multimode fibers, solved in [56], the incident angle, θ, must also be integrated. This is not necessary for surface wave waveguides because we assume a single mode whose incident angle can be calculated from (4.8). The attenuation coefficient is the amount of power transmitted, *T*, per unit angle between transmissions: $\gamma = T/\Delta\phi$. θ_c is the complement to the critical angle, and the transmission values for refracting rays ($\theta_o > \theta_c$) and tunneling rays ($\theta_o < \theta_c$) are shown below [57]:

$$T_R = 4\frac{\sin\theta_o}{\sin\theta_c}\sqrt{\frac{\sin^2\theta_o}{\sin^2\theta_c} - 1}\,, \tag{4.12}$$

$$T_T = 4\frac{\sin\theta_o}{\sin\theta_c}\sqrt{1 - \frac{\sin^2\theta_o}{\sin^2\theta_c}} \times \exp\left(\frac{4\pi}{3\lambda} n_1 (R+\rho)\left(\theta_c^2 - \theta_o^2\right)^{3/2}\right), \tag{4.13}$$

$$\theta_c(\theta,\omega) = \cos^{-1}\left(n_2 / n_1(\theta,\omega)\right). \tag{4.14}$$

Note that the critical angle, θ_c, is explicitly defined to be angle- and frequency-dependent due to the angle- and frequency-dependent index in the guiding region. For

refracting rays, T_R is the standard Fresnel relation. For tunneling rays, T_T is solved using a local plane wave analysis [56]. In [14] it was found that a true surface wave Fresnel equation gave improved results for the phase on total internal reflection because it was necessary to calculate the exact reflection phase shift (4.6). For losses due to bending we have found that local plane wave analysis adequately predicts losses for the curved surface wave waveguide.

Figure 4.34 shows the results for bending loss in the fabricated structure. The measured data is calculated from the fields above the waveguide. The simulated curve uses ideal tensor impedance boundaries with impedances as shown in Figure 4.22. The theory curved is solved numerically from (4.11). Results show similar characteristics for all three methods. In each case, minimal power is transmitted at low frequencies. At high frequencies there is nearly-full power transmission for the simulated and theory cases. The measured version shows some losses between 14-15 GHz. These losses are due to bending loss of the second waveguide mode (which has a theoretical cutoff of 14.2 GHz and is not included in the theory), and material loss. Bending loss of the first mode does not occur in this frequency range. This lossy section is also in the range where the TM mode is distorted by the presence of TE modes. The theoretical model closely predicts the frequency at which the structure no longer has nearly-complete-guiding at 12.5GHz. However, the theory shows a steeper drop-off from nearly-complete-guiding towards increased bending loss at lower frequencies.

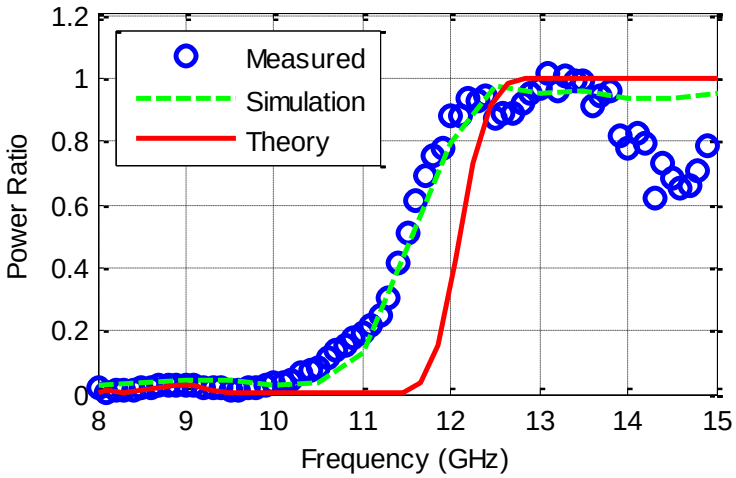

Figure 4.34: Power loss over 90 degree bend on fabricated structure.

The theory was used to predict the bending loss for different waveguide radii using the same unit cells, and the results are shown in Figure 4.35. The half power frequency is the frequency where the guide delivers half the power around the bend. The theory predicts this location at 12.09 GHz for the fabricated structure as seen in Figure 4.34 and labeled explicitly in Figure 4.35 (note 20.32cm = 8 inches). As the center radius, *R*, decreases the half power frequency increases. This is because higher frequencies have larger impedance contrast, and *R* is electrically larger. On the right *y*-axis the maximum transmitted power is plotted for each *R*. For $R<0.75$cm the waveguide does not propagate 50% of the power at any frequency. The maximum power output occurs about 0.5GHz above the half power frequency as seen in Figure 4.34.

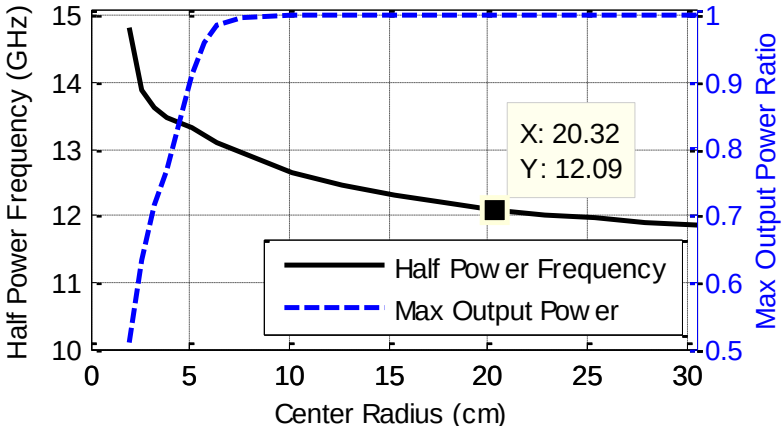

Figure 4.35: Frequency of half-power loss vs. center radius of the waveguide. The right axis shows the maximum power output from the waveguide.

In the realized structure the impedance of the unit cell is dependent on frequency. In order to show the effects of impedance and radius on propagation independently, the theory was applied to a waveguide using ideal impedance boundary conditions. The setup had guide width of 10mm, and outer region n=1.1. The index of the inner region was swept from 1.2 to 2 (isotropic) for multiple radii. The results are shown in Figure 4.36. For any given index value, increasing the radius decreases the frequency where half the power is transmitted. Similarly, for a specific radius, increasing the index decreases the frequency of half-power transmission.

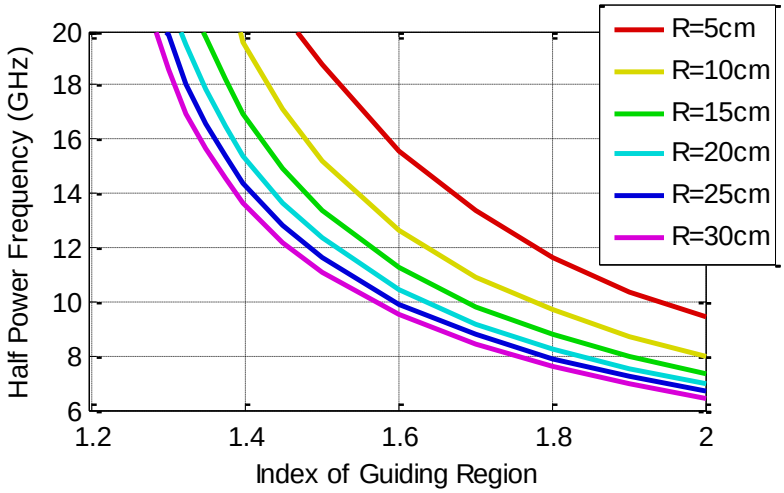

Figure 4.36: Half power frequency vs. index of guiding region. Plots for multiple center radii are shown. The index of the outer region is 1.1, the guide width is 10mm, and the bend angle is 90 degrees.

4.4 Conclusion

We have demonstrated a simple application of tensor impedance surfaces in the form of a waveguide that is transparent to surface waves in the orthogonal direction. This can be extended to enable new applications such as antennas with reduced scattering or nulls in a given direction, or that produce different radiation patterns depending on the feed location.

Chapter 4 is based on and mostly a reprint of the following papers: R. Quarfoth, D. Sievenpiper, "Non-scattering Waveguides Based on Tensor Impedance Surfaces", Submitted to *IEEE Transactions on Antennas and Propagation*; R. Quarfoth, D. Sievenpiper, "Artificial Tensor Impedance Surface Waveguides", *IEEE Transactions on Antennas and Propagation*, vol. 61, no. 7, pp. 3597-3606 2013.

Chapter 5 Surface Wave Beam Splitter

5.1 Overview

Surface waves can be controlled to prevent damage to objects on the surface or to minimize interference with other antennas or systems. One method to control propagation in volume media is by transformation electromagnetics. It will be shown that some transformation methods cannot be implemented for surface wave structures. However, a beam shifter and beam splitter can be implemented for surface waves. These structures are first used to create a surface impedance cloak on ideal boundaries. Subsequently a surface wave beam splitter is realized that is created using two adjacent beam shifters built with tensor impedance surfaces. The beam shifters are oriented in opposite directions so that an incident beam is split into two directions. The fabricated that splits an incident beam, and it is shown that the scattering from an object on the surface is significantly reduced as compared to a homogeneous isotropic surface.

5.2 Surface Waves and Transformations

Tensor impedance surfaces have been patterned to create a holographic antenna [7]. In volume media, transformation methods have been shown that give impressive control over wave propagation in a region [58-62]. In transformation electromagnetics, the permittivity and permeability tensors of an initial medium (usually vacuum) are transformed into complex, spatially-dependent tensors. A beam shifting material was originally solved in three dimensions by using a finite embedded coordinate transformation [60]. Volume media have been proposed as a method to shift surface plasmon polaritons [61, 62]. At microwave frequencies a beam shifting slab using tensor transmission-line (TL) metamaterials was constructed [63]. TL metamaterials have also

been used for other planar applications including a hyperbolic structure [64], and a demonstration of a full-tensor effective medium [65]. A surface wave implementation is advantageous as compared to three-dimensional or TL methods because surface waves can affect antenna patterns, scattering characteristics, and radar cross section of a system. Transformation methods for volume media often require highly anisotropic values for ϵ and μ. In this study we have investigated the applicability of transformation techniques to surface structures. Limitations on the constitutive properties that can be set in-surface prevent some of the most complex transformational structures from being achieved on a surface. A seminal work in transformation techniques involves the cloaking of a cylindrical region using an annulus shaped volumetric cloak [59]. An illustration of this setup is shown in Figure 5.1.

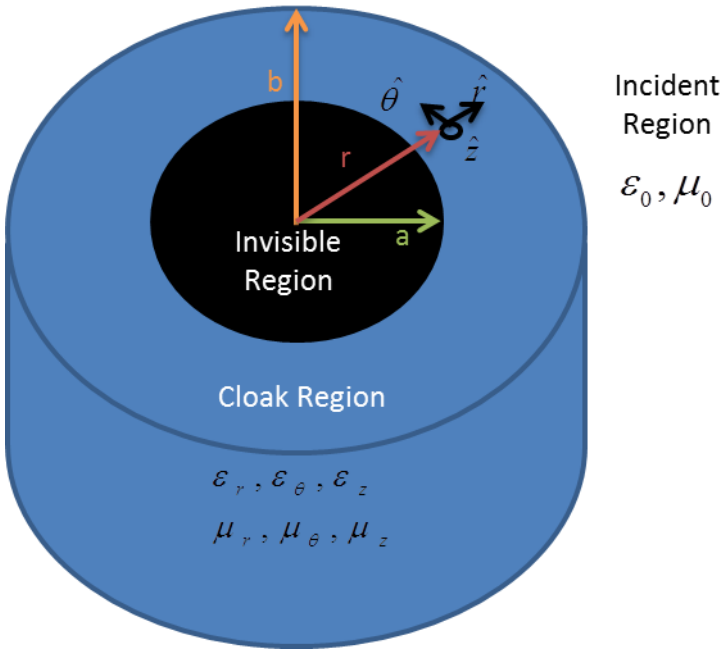

Figure 5.1: Illustration of microwave cloak.

The invisible region is a volume where any material may be place without affecting the scattering characteristics of the volume. The material properties of the cloak in cylindrical coordinates were solved as [59]:

$$\varepsilon_r = \mu_r = \frac{r-a}{r}, \quad \varepsilon_\theta = \mu_\theta = \frac{r}{r-a}, \varepsilon_z = \mu_z = \left(\frac{b}{b-a}\right)^2 \frac{r-a}{r}, \tag{5.1}$$

where a and b are the inner and outer radii of the annulus respectively. These constitutive properties can be implemented using metamaterials, but in general this is only possible over narrow bandwidths. A plot of the material properties of the cloak as a function of position is shown in Figure 5.2. The incident region is vacuum.

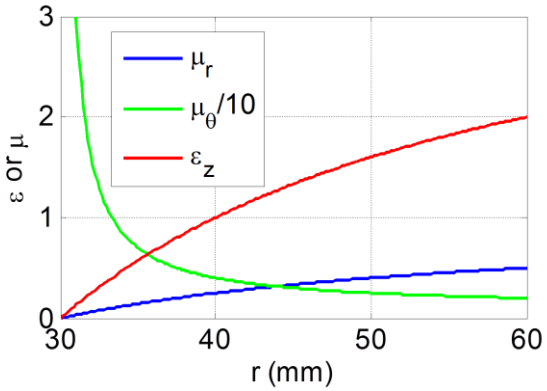

Figure 5.2: Material properties of microwave cloak.

However, unlike volumetric materials where full tensor solutions of ε and μ can be set, within a surface, only three independent variables can be set, Z_{xx}, Z_{yy}, Z_{xy} as seen below in the tensor impedance boundary condition:

$$\begin{bmatrix} E_x \\ E_y \end{bmatrix} = \begin{bmatrix} Z_{xx} & Z_{xy} \\ Z_{xy} & Z_{yy} \end{bmatrix} \begin{bmatrix} -H_y \\ H_x \end{bmatrix}. \tag{5.2}$$

Furthermore, in volumetric materials it is possible to independently set the impedance and index in the material. This is not possible in surface implementations where the impedance and index are linked as described below for TM modes:

$$n_S = \sqrt{1 - \left(\frac{Z_S}{Z_0}\right)^2}. \tag{5.3}$$

Additionally, metamaterials allow regions with index below one, as is required by the cloak in (5.1). Such a surface would allow leaky waves and thus actually increase scattering. The relation between n_S and Z_S is such that a surface of zero-impedance would correspond to an index of one, as seen in (5.3).

Therefore, surface transformations can be anisotropic in-surface only, and must have n>1. One application is a beam shifter which can be created using an embedded coordinate transformation [60], with material properties as follows:

$$\varepsilon = \mu = \begin{bmatrix} 1 & a & 0 \\ a & 1+a^2 & 0 \\ 0 & 0 & 1 \end{bmatrix}, \tag{5.4}$$

where a=tan(φ), and φ is the shift angle. This material tensor can be approximated for surface structures using only the first two dimensions:

$$n = \begin{bmatrix} 1 & a \\ a & 1+a^2 \end{bmatrix}. \tag{5.5}$$

However, (5.5) is only an approximation because it assumes that the air above also has this value. A full solution for surface beam shifting on tensor impedance surfaces is given in [66] (where the impedance is obtained by solving a system of equations (20) and (28) in [66]). The full analysis will be shown to be significantly more accurate than the approximate analysis given in (5.5). Despite being less accurate, the method has the advantage of being very simple, and it was used to demonstrate the ability of an impedance surface to cloak an incident surface wave.

5.3 Ideal Tensor Impedance Surface Wave Cloak

A cloak for an incident surface wave beam was created by implementing a beam splitter and combiner in series as shown in Figure 5.3a. Isotropic impedance is shown as blue regions while shifting regions are shown in green and red depending on the shift direction. A PEC region shown in black is also placed to prevent scattered surface waves from forming in the cloaked region. These scattered waves are inherent to propagating waves and have been noted for plane waves by other groups [60]. The shift angle was set to φ=20°. The impedance of the incident region was j400Ω. Figure 5.3b shows the vertical electric field component as it avoids the center region and recombines in phase. This cloaking effect will only work on surface waves incident vertically as shown. The magnitude of the electric field is shown in Figure 5.3c.

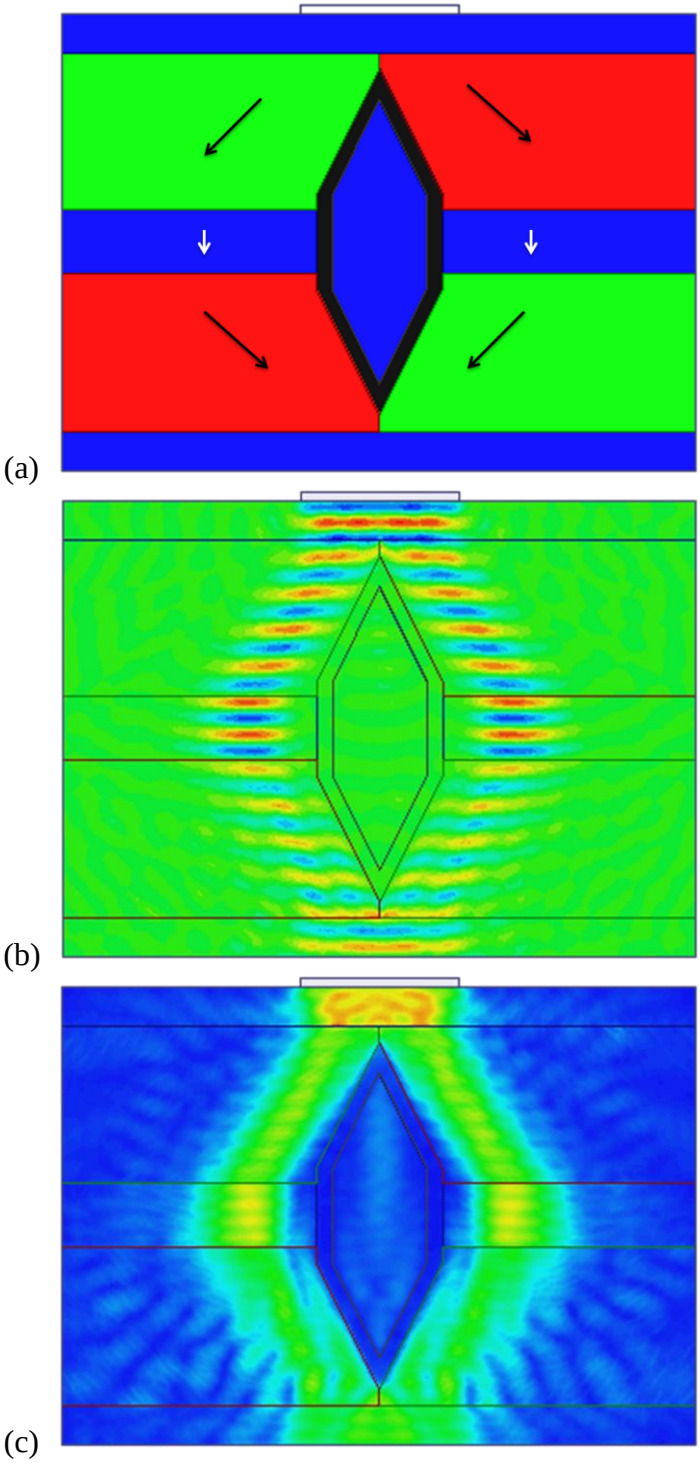

Figure 5.3: Cloaking simulation setup and results. (a) shows the simulation setup, (b) shows the electric field normal to the surface, and (c) shows the magnitude of the electric field.

Wave scattering causes some power in the cloak region and outer regions, but the power mainly moves around the inner region as desired. An uncloaked structure is shown in Figure 5.4. Figure 5.4a shows the setup for the uncloaked version where the entire area is patterned with isotropic impedance except for the PEC shell that surrounds the interior. The vertical electric field is shown in Figure 5.4b, and the electric field magnitude is shown in Figure 5.4c. In this case the PEC reflects the surface waves and they do not recombine on the far side of the structure. We can also see that a larger fraction of power enters the cloaked region inside the PEC shell.

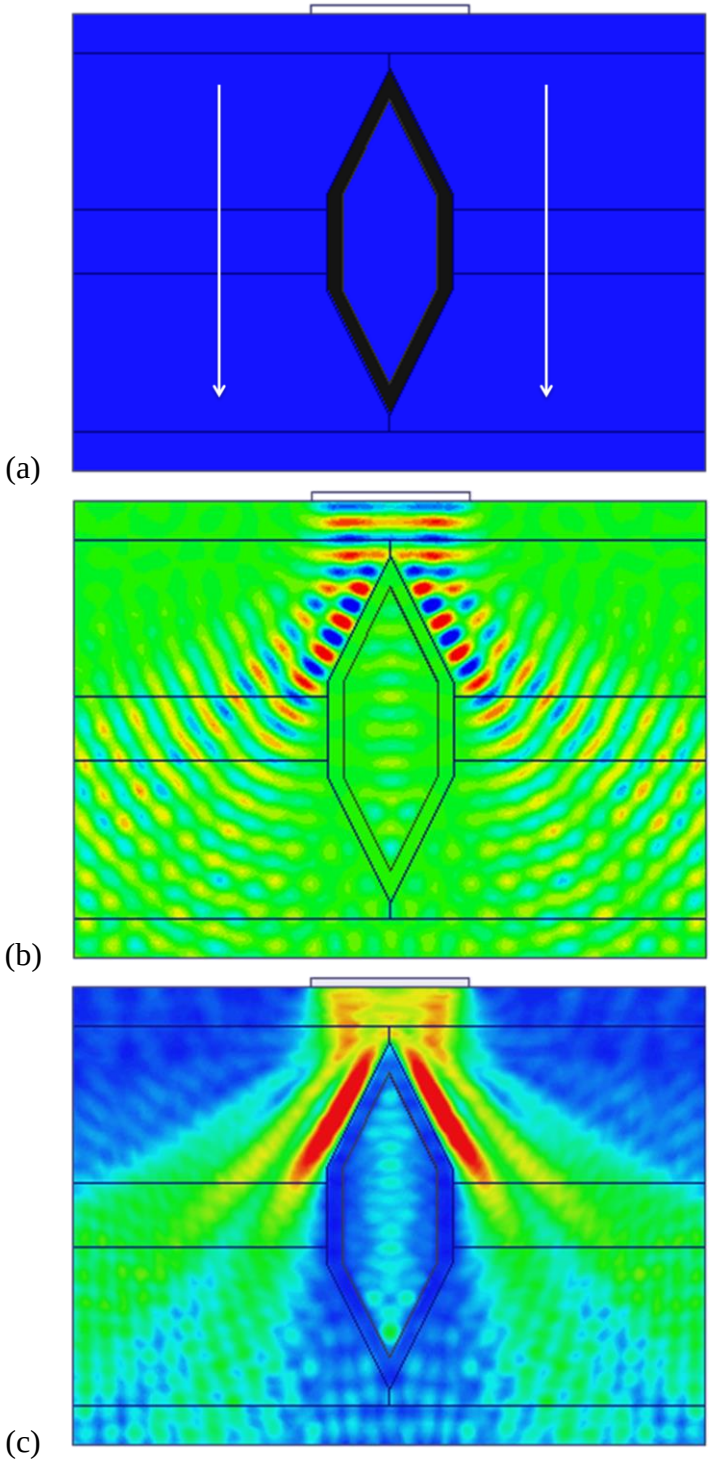

Figure 5.4: Uncloaked simulation setup and results. (a) shows the simulation setup, (b) shows the electric field normal to the surface, and (c) shows the magnitude of the electric field.

5.4 Realized Surface Wave Beam Splitter

A significant challenge of transformation electromagnetics structures is fabricating structures with the desired material properties. Two-dimensional surfaces are much easier to construct, and printed circuit fabrication is frequently used. A rigorous analysis of the properties of a printed circuit structure with no vias has been performed [26, 27]. A broadband, highly anisotropic unit cell has also been analyzed [67], and this type of unit cell is used here to create the beam splitter.

5.3.1 Unit Cell Design

Multiple methods have been studied to generate impedance surfaces, and in this paper a ring-mushroom unit cell is used as described in Section 3.3. The advantage of the ring-mushroom unit cell is that it can achieve highly anisotropic surface impedance over a broad bandwidth, and larger anisotropy allows increased beam shift angles. The rectangular ring creates anisotropy and the mushroom is small to prevent a band gap where surface waves cannot propagate. Our design used a 1.27mm thick Rogers 3010 substrate, and for simulation the design dielectric constant of 11.2 was used. A unit cell is illustrated in Figure 5.5. The high impedance direction is along the short side and is due to the patch geometry. The unit cell is 6mm in the low impedance direction to simplify fabrication. The unit cell would have had similar properties if it were 2x2mm with the same patch geometry, but by extending the low impedance direction, comparable surface properties are achieved and three times less unit cells can be used to create a surface.

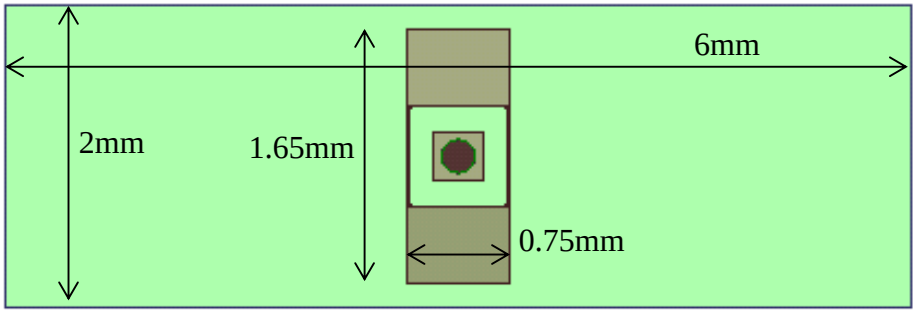

Figure 5.5: Unit cell dimensions. The unit cell is anisotropic with side lengths of 2mm and 6mm. A rectangular patch is centered in the cell. A via is represented by the circular area in the center of the unit cell.

A photograph of the unit cell patch is shown in Figure 5.6. The patch is rotated with respect to Figure 5.5. A plated via is in the center of the cell and is white due to light coming from the back of the structure. The dimensions of the unit cell are shown in Figure 5.6, and these were used to simulate the structure in Ansys HFSS version 15. The eigenmode solver was used to simulate an infinite lattice of cells, and the dispersion results are shown in Figure 5.7. In the eigenmode solver the phase velocity angle is set and the low and high impedance curves are the results of a wave traveling along the principal axes of the unit cell. The 45 degrees curve is a surface wave with phase velocity that bisects the principal axes at 45 degrees.

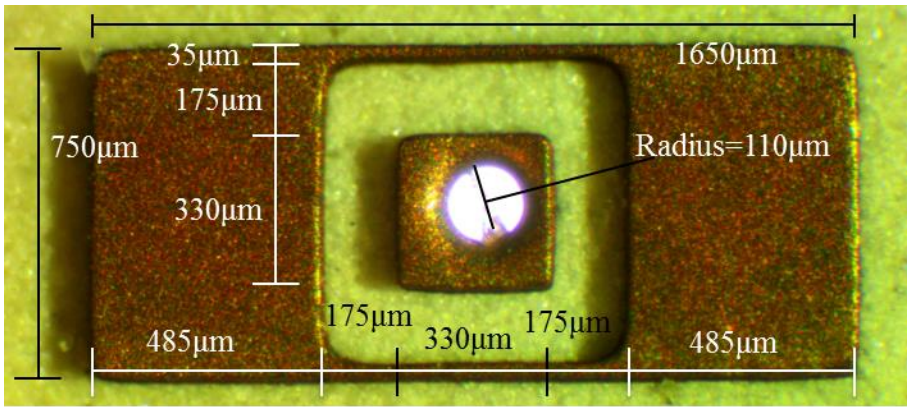

Figure 5.6: Photograph of a unit cell patch with measurements. The photograph is a zoomed-in and rotated version of the patch shown in Figure 5.1.

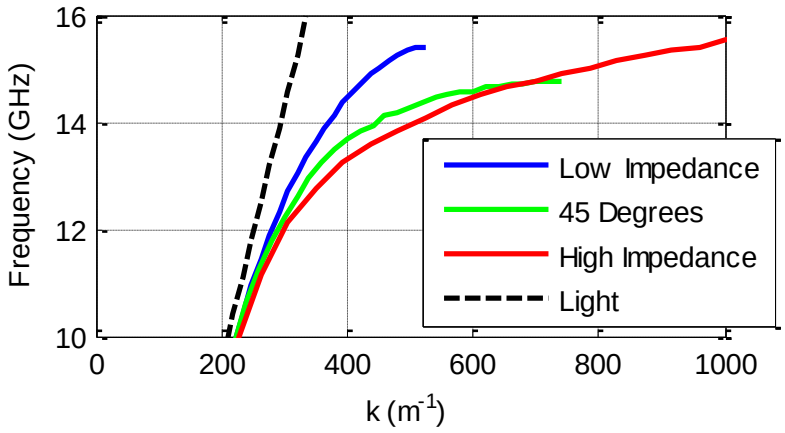

Figure 5.7: Dispersion diagram for ring-mushroom unit cell.

Figure 5.8 shows the frequency dependent surface impedance of the unit cell. For TM-like surface waves the impedance can be calculated from the dispersion relation as follows:

$$Z = Z_0 \sqrt{1 - \frac{k^2}{k_0^2}} \,. \tag{5.6}$$

Below 10 GHz the unit cell is nearly isotropic with surface impedance trending towards zero. The impedance of the 45 degree wave should lie between the low and high impedance directions, but at about 14.7 GHz this impedance rises above the high impedance direction. This is a region where the unit cell cannot be used. In experiment, it was difficult to get results above 14.1 GHz. At this frequency the dispersion of the 45 degree curve is also starting to deviate from an ideal tensor impedance boundary condition.

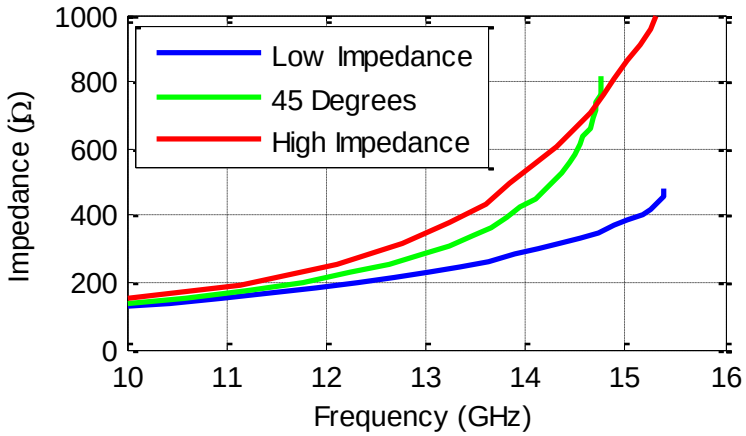

Figure 5.8: Impedance vs. frequency for ring-mushroom unit cell.

5.3.2 Beam Shift Design and Measurement

A surface was constructed using two adjacent sections that shift beams in opposite directions as illustrated in Figure 5.9. The total size of the surface was 406.4×254mm. The long dimension was split so that each half shifted surface waves in opposite directions. Parallel incidence on the surface results in the beam splitting while series incidence causes shifting in one direction followed by a shift in the opposite direction. Series beam shifting is possible in either direction, but for parallel incidence the beam is only split for one incidence direction.

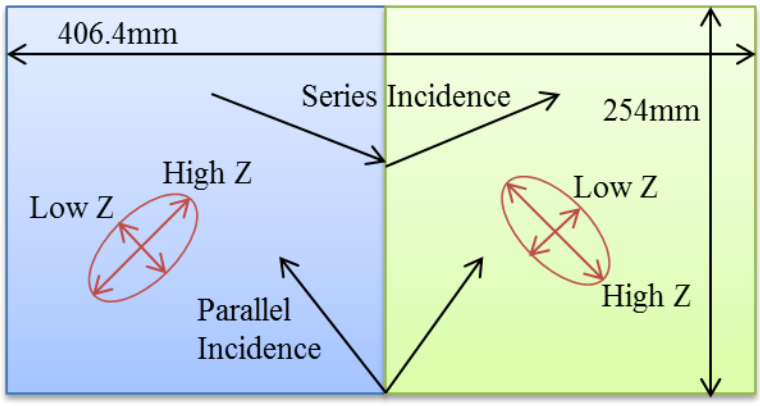

Figure 5.9: Fabricated structure setup.

The unit cells were oriented 45 degrees with respect to the board as shown in Figure 5.10. This orientation allows the shift angle to be the same for parallel and series incidence. Due to their shape and rotation, the unit cells must be truncated at the boundary between the beam shifters. This truncation causes some deviation from the desired surface properties in this region, but experiments show that it does not significantly impact the results. Had it been necessary, a unit cell which does not need to be rotated could have been used but potentially at the cost of performance and bandwidth.

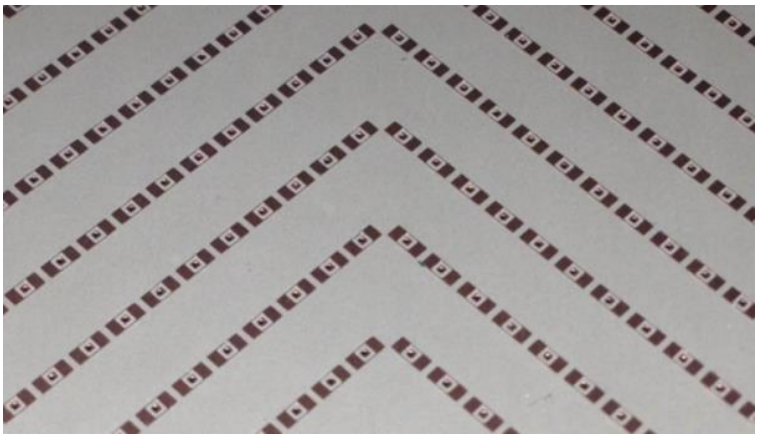

Figure 5.10: Photograph of beam shifter setup. The dimension of the photographed section is approximately 35x20mm.

The near field profile was measured by scanning a vertical probe 2mm above the surface. Data was taken at 2mm increments using an Agilent E5071C vector network analyzer. Magnetic radar absorbing material was placed around the edge of the substrate. Normalized field results are shown in Figure 5.11. The measured area is slightly smaller than the total board size, and the boundary between the beam shift sections is shown as a dotted line. The beam has phase fronts which are predominantly vertical and shifts downwards and then back upwards in the two sections. Some radiation is excited at the boundary and causes loss in surface wave power. The feed also excites radiation outside of the main beam which can be seen throughout the surface. The feed was constructed using a linear array of eight, in-phase, end-launch SMA connectors attached to a dielectric substrate. The elements were spaced at 1cm

increments and launched a main beam forward with side lobes at other angles.

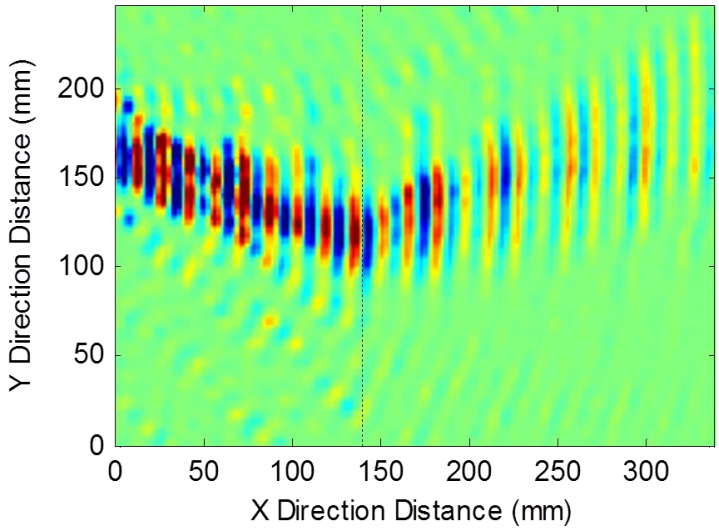

Figure 5.11: Measured normalized near field for series incidence at 13.5 GHz. The dotted line marks the break between the beam shifters.

From the near field measurements the beam shift angle can be obtained by hand by measuring the distance of the shift and the distance traveled. These measurements are plotted in Figure 5.12. The simulated response is calculated from the HFSS eigenmode simulation. The phase velocity is oriented 45 degrees with respect to the unit cell. The Poynting vector was obtained from the simulated fields and the beam shift angle is the difference between the phase velocity direction and Poynting vector. The simulated results show the same trend as the measured value. Differences may be due to manufacturing variability of the unit cells and the difficulty of determining the beam shift lengths when measuring by hand. Above 14.1 GHz the surface is difficult to measure because surface impedance goes up with frequency. At higher impedances the surface wave is more closely bound to the surface. The measurement probe is located 2mm above the surface and a significant amount of power is below this height and in the substrate. Plane waves can also be excited above the substrate, and above 14.1 GHz, more plane waves are measured than surface waves.

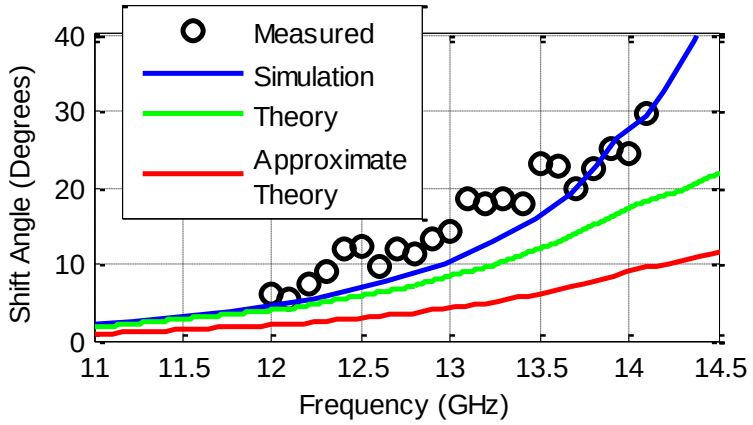

Figure 5.12: Beam shift angle results. The theory curve is solved from [66] and the approximate theory is from (5.5).

The theory curve in Figure 5.12 uses the analysis performed in [66]. Z_{xx} and Z_{yy} are taken from simulation (as plotted in Figure 5.8), and the orientation is set to 45°. From these assumptions the shift angle can be solved and this angle is plotted in Figure 5.12. At low frequencies the theory closely matches the simulation but it deviates at higher frequencies. At higher frequencies the spatial dispersion of the structure is significant and the tensor impedance boundary condition no longer accurately models the surface. This phenomenon has been discussed for a similar unit cell [26, 27]. In this case, the surface exhibits larger beam shifts than the theory predicts. The approximate theory is solved from (5.5) and significantly underestimates the beam shift angle across the entire frequency range.

5.3.3 Surface Scattering

A surface scattering setup was used in parallel incidence. An H-plane sectoral horn was placed at the boundary between the beam shifters. A metal cylinder (radius = 3.7cm) was placed on top of the surface and the surface profile was measured using the same near field scanning setup. The results from the beam splitting setup are shown in Figure 5.13. In Figure 5.14, a grounded 1.575mm thick slab of Rogers 5880 (ε_r = 2.2) was measured with the same metal cylinder present. The area beneath the cylinder could not be measured and is shown in black. The radius of the black region is 0.5cm larger

than the radius of the cylinder to ensure that the probe did not contact the cylinder. The phase fronts exiting the horn were not completely straight but the horn was preferred because it had less side lobes than the SMA splitter used for the series beam shift. In Figure 5.13 the incident beam is split and minimal surface wave power is scattered by the cylinder. Conversely, in Figure 5.14 the surface is isotropic and the beam directly hits the cylinder and scatters in all directions. The wavelength is longer on the isotropic surface because the structure has lower surface impedance. As discussed for the series beam shift, the shift angle is frequency dependent. At 13.5 GHz, as shown in Figure 5.13, the incident beam mostly avoids the scattering object. However, at lower frequencies the shift angle decreases (as plotted in Figure 5.12). As the shift angle decreases the beams are directed more closely towards the scattering cylinder until the limit where the shift angle is zero and a single beam travels directly at the cylinder as shown in Figure 5.14.

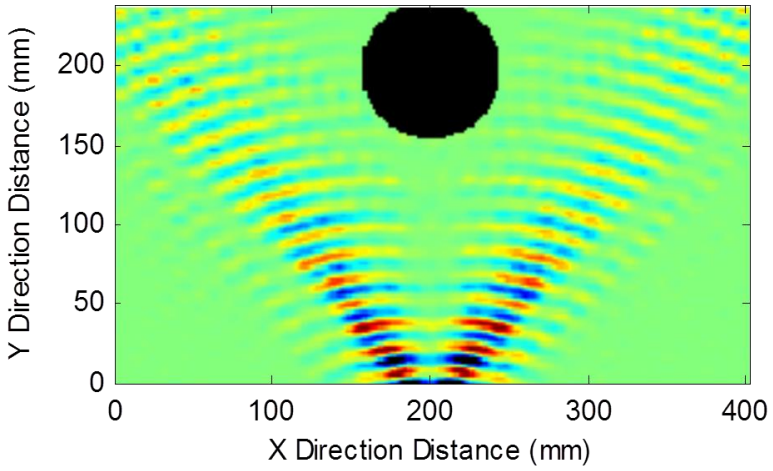

Figure 5.13: Measured field results for beam splitting surface at 13.5 GHz.

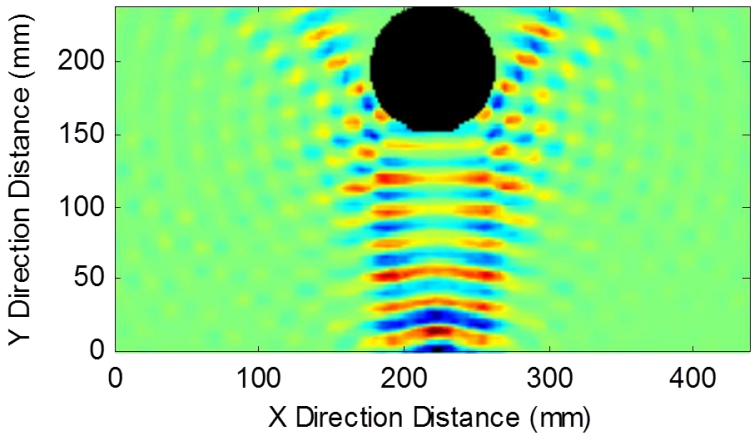

Figure 5.14: Measured field results for isotropic impedance surface at 13.5 GHz.

5.5 Conclusion

A surface was created that reduces scattering from an object by sending incident power in different directions. This type of structure could be used to shield regions on a surface from surface waves incident externally, or to prevent interference between two antennas on the same substrate. Similar patterning methods could be used for other applications such as reducing the radar cross section of an object or guiding power in a desired direction.

Chapter 5 is based on and mostly a reprint of the following papers: R. Quarfoth, D. Sievenpiper, "Surface Wave Scattering Reduction Using Beam Shifters", *IEEE Antennas and Wireless Propagation Letters*, vol.13, pp. 963-966, 2014; R. Quarfoth, D. Sievenpiper, "Anisotropic Surface Impedance Cloak", *IEEE Antennas and Propagation Symposium Digest*, Chicago, IL, USA, July 8-14, 2012.

Chapter 6 Manipulation of Scattering Pattern Using Impedance Surfaces

6.1 Overview

Electromagnetic is relevant to multiple applications including imaging, communications, radar, and antenna design. The scattering characteristics of an object are predominantly determined by its shape and material. In this study, the scattering profile of a shape is altered by patterning anisotropic impedance surfaces onto the material. The scattered radiation from a rectangular object is altered as illustrated in Figure 6.1. When a rectangular surface is illuminated by a plane wave normal to one edge, it scatters the wave backwards towards the source. By patterning the object with impedance surfaces, this backwards radiation can be changed to a different angle.

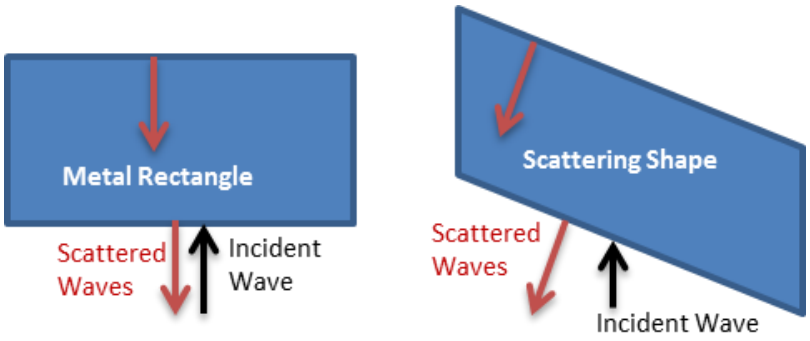

Figure 6.1: Scattering manipulation.

Various methods have been used to change the scattering pattern of an object. Transformation electromagnetics allows precise control of propagation and scattering of waves [58, 68]. Volumetric metamaterials were used to surround a cylindrical region and cloak it [59, 69]. Transformation media have also been used to rotate

electromagnetic fields [62, 70, 71], and shift beams [60, 61], along with many other applications. However, bulk metamaterials are generally electrically thick, narrow bandwidth, heavy, and difficult to fabricate. Thin metasurfaces are advantageous because they are light and easily fabricated. Surface impedance structures have been used to reduce the scattering cross section of various shapes [11, 72]. These mantle cloak structures work best on dielectrics (as opposed to metal), and cannot be easily applied to electrically large metallic structures.

Impedance surfaces are an electromagnetic boundary condition that defines the relationship between electric and magnetic fields within the surface. Electrically thin surfaces can be modeled as impedance surfaces, and this allows electrically large surfaces to be modeled efficiently. Impedance surfaces have been used to alter the scattering of a coated metal cylinder [73], and further work has provided a method to coat arbitrary three-dimensional shape with impedance surfaces [74]. Various numerical and analytical techniques have also been studied for scattering from anisotropic impedance surfaces [75-77]. Impedance surfaces have also been used for antennas [1, 7, 8], lenses [3, 78], transformation structures [66, 79], waveguides [14, 80], coatings for horns [10], and for surface wave suppression [28].

In this investigation, a rectangular metallic object is coated with a lossless anisotropic impedance surface, and the scattering is compared to an equivalent metal rectangle. The impedance surfaces that are used are called hard and soft surfaces, which have been analyzed previously [81, 82]. Hard surfaces support both transverse magnetic (TM) and transverse electric (TE) surface modes, while soft surface support neither. Hard and soft surfaces have been used in multiple ways to alter scattering properties [83-85]. In this case, the hard and soft surfaces are used in a novel setup where a false edge is created in the surface that scatters the incident wave as opposed to the real edges of the metal rectangle. The surface is patterned in two sequential sections where the incident region is a hard surface and the transmitted region is a soft surface. By patterning an angled discontinuity between the two regions, the incident wave scatters at an angle, and not back towards the source. This effect is achieved for both incident polarizations.

6.2 Scattering Design

A side view of the scattering setup is shown in Figure 6.2. A finite rectangular surface is located in the XY plane, and a plane wave is incident on the surface at an angle θ. The rectangular surface is used because it has a simple scattering pattern with a single main lobe in the backwards direction. The surface is assumed to have thickness much less than the wavelength. The incident mode can have two polarizations, and any other polarization is a superposition of the two. The TM_i polarization has magnetic field normal to the plane of incidence, and the TE_i polarization has electric field normal to the plane of incidence. In each case, the subscript labels the modes as related to the incident wave.

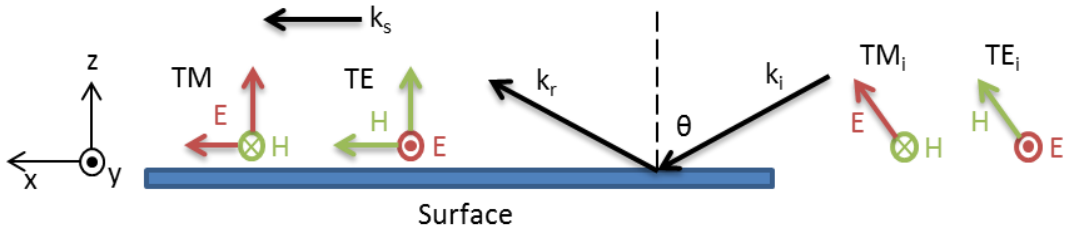

Figure 6.2: Mode polarizations of incident radiation and surface waves.

For each incident polarization, a corresponding surface wave is excited with similar field polarizations. However, these surface waves are distinct from the incident plane wave, and they are also illustrated in Figure 6.2. Surface wave modes are excited on the surface due to the incident radiation. On metals these are the standard surface currents that exist in the presence of electromagnetic fields. On textured surfaces, surface waves propagate bound to the surface [28]. TM surface wave modes have magnetic field perpendicular to the direction of propagation, and TE modes have electric field perpendicular to the direction of propagation. The orientation of the electric and magnetic field components are the same in the respective surface wave modes and incident plane waves. However, the relative magnitude and phase of each field component are not the same. For surface modes the subscript is removed, and we will subsequently refer to both the incident polarization and the corresponding surface mode

generally as TM or TE with no subscript.

For a flat metal surface, a significant portion of the incident wave is geometrically reflected, and this generates large scattering in the forward direction. In this study we are primarily concerned with the scattering in the backwards direction towards the source. Along with the geometrical reflection, the TM and TE polarizations scatter from the back and front of the surface respectively as shown in Figure 6.3. This edge scattering is what predominantly contributes to the backwards scattering pattern. A perfect magnetic conductor would have the opposite setup with TM scattering off the front and TE scattering off the back.

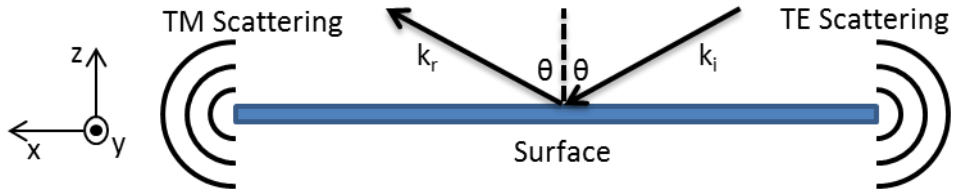

Figure 6.3: Scattering from metal rectangle. For an incident plane wave, TE-polarized waves scatter from the front and TM waves scatter from the back.

The plane wave is incident at an elevation of θ as seen in Figure 6.2 and Figure 6.3. In the azimuthal direction the wave is incident at an angle ϕ=0 as seen in Figure 6.4.

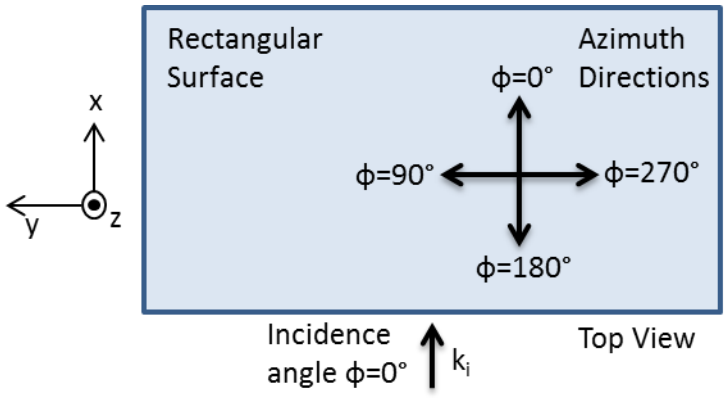

Figure 6.4: Top view of scattering setup.

The rectangular metal surface has maximum backwards scattering ($90° \leq \phi \leq 270°$) at $\phi = 180°$. For each polarization, the surface can be patterned in order to redirect

this backwards scattered lobe. A false edge is created by patterning a discontinuity in surface impedance at an angle so that the scattering occurs at this angle instead of back towards the source. The ideal setup for each polarization is shown in Figure 6.5. For TM waves the front edge is perfect electric conductor (PEC) and the back perfect magnetic conductor (PMC) so that neither edge scatters the incident wave. The boundary between the two regions is at an angle, ψ, and the scattered waves are maximum at $\phi = 180°-2\psi$. This new scattering peak is due to the geometric reflection from the false edge as illustrated in Figure 6.5. For TE waves, the ideal setup is reversed with PMC in front and PEC at the back.

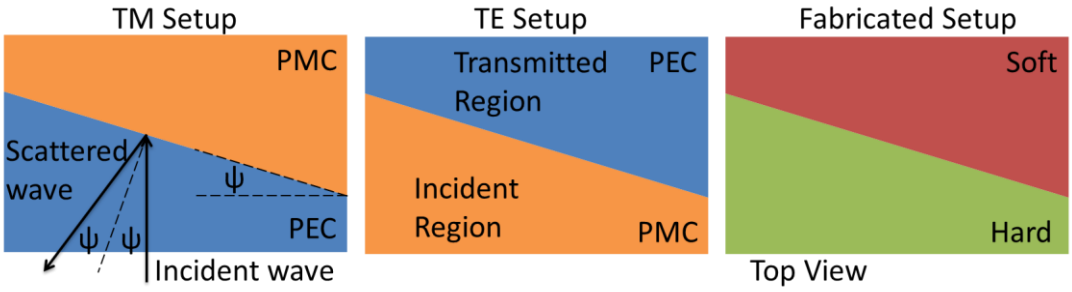

Figure 6.5: Ideal setup to prevent scattered radiation back towards the source.

The ideal isotropic setups cannot be achieved simultaneously, but an anisotropic setup can be created using hard and soft surfaces as shown in Figure 6.5. Hard surfaces allow both TM and TE waves to propagate. The incident region uses a hard surface so that the incident wave does not reflect from the front edge of the structure. The hard surface will also support bound surface waves as illustrated in Figure 6.2. Therefore, the soft surface patterned in the transmitted regions serves two purposes. First, the soft surface prevents reflection off the back edge of the rectangle, and second, the soft surface reflects surface waves propagating from the incident region. The surface waves reflect at an angle due to the angled boundary between the incident and transmitted regions.

Real hard and soft surfaces are anisotropic and are not exactly modeled by PEC and PMC. Section 6.3 discusses the unit cells used to make the hard and soft surface and

presents simulations showing the material properties of these materials. The ideal (using PEC and PMC as illustrated in Figure 6.5) scattering structure was simulated using Ansys HFSS version 15. The surface was 400mm wide and 200mm long, and the boundary between PEC and PMC regions had angle of $\psi = 21.8°$. The surface was excited by a near-grazing plane wave at an elevation of $\theta=70°$. The backwards directivity at $\theta=70°$ is plotted in Figure 6.6.

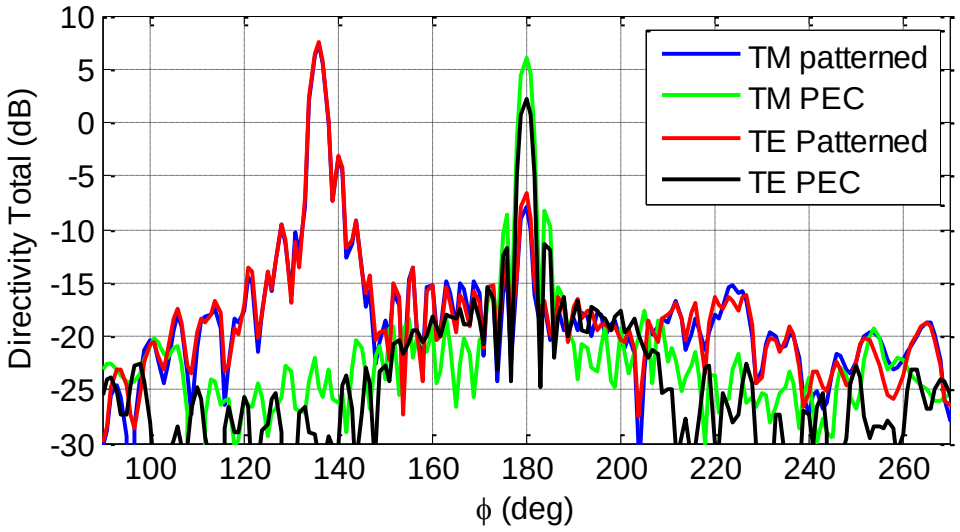

Figure 6.6: Backward scattering of ideal setup.

As expected, the PEC surface reflects each incident wave strongly back towards the source at $\phi=180°$. The patterned surfaces have relatively low scattering at $\phi=180°$ (around -7dB). Instead, the largest scattering peak is located at 136 degrees, which $180°-2\psi$, as predicted by geometrical reflection. By changing the angle of the boundary between PEC and PMC, the scattered lobe can be moved to other angles. The directivity at $\phi=180°$ is reduced for each polarization by more than 10 dB.

6.3 Unit Cell Design and Simulation

In the idealized simulation of the structure, the PEC and PMC regions are both isotropic. In a realized version this is not possible, and each region is instead created with anisotropic impedance surfaces. Anisotropic impedance surfaces can be built by

using periodic structures [7, 52]. The unit cell geometries are shown in Figure 6.7. Dimensions of the cells are chosen for optimized results near 15 GHz. In each case, the substrate is grounded Rogers 5880 with thickness 1.575mm. Each unit cell has an identical copper patch that is rotated in the two cells. Periodic dipole patches on a grounded dielectric have been used previously to create hard and soft surfaces [43, 86]. In this case the transmitted region unit cell has a plated metal via in order to suppress surface wave propagation [28]. The plane wave is incident in the *x*-direction to the unit cells, and for this orientation the incident and transmitted cells will be hard and soft respectively. For waves incident in the *y*-direction, the incident and transmitted regions switch to become soft and hard respectively. This is due to the anisotropy of the unit cell.

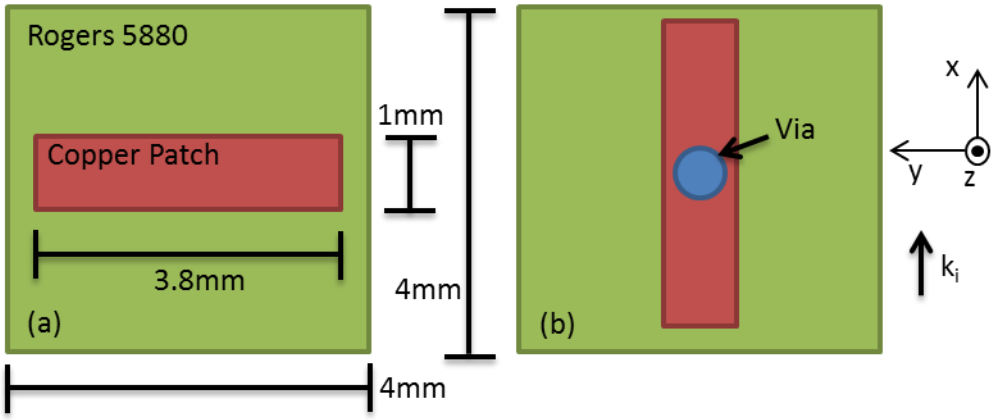

Figure 6.7: Top View of unit cell geometries. (a) shows the unit cell for the incident region and (b) shows the unit cell for the transmitted region.

The properties of the unit cells were simulated using HFSS. Normal incidence reflection and surface wave propagation were both simulated in order to ensure that the scattering characteristics are correct for incidence angles from normal to grazing. The presence of the via does not have an effect on normal incidence reflection. The simulated reflection phase of each unit cell is shown in Figure 6.8. The blue curve shows the reflection for the electric field parallel to the long dimension of the patch. This is the orientation for the incidence region under TE illumination and the transmitted region under TM illumination.. At 15.4 GHz, the unit cell has a reflection

phase of 0 degrees which implies that it acts as PMC around this frequency range. The range where the reflection phase is between -90 degrees and 90 degrees is from 12.4-18.3 GHz. The red curve shows the reflection phase for electric field parallel to the short dimension of the patch. This is the setup for the incidence region under TM illumination and the transmitted region under TE illumination. At 15.4 GHz, the reflection phase is 111 degrees. From 12.4-18.3 GHz, the reflection phase varies from 128 degrees to 92 degrees. PEC has a phase delay of 180 degrees. The phase delay of the red curve would be closer to 180 degrees if a thinner substrate was used, but at the cost of narrower bandwidth (of the PMC reflection). Measurement results presented in Section 6.4 show that these properties are sufficient to obtain good scattering results.

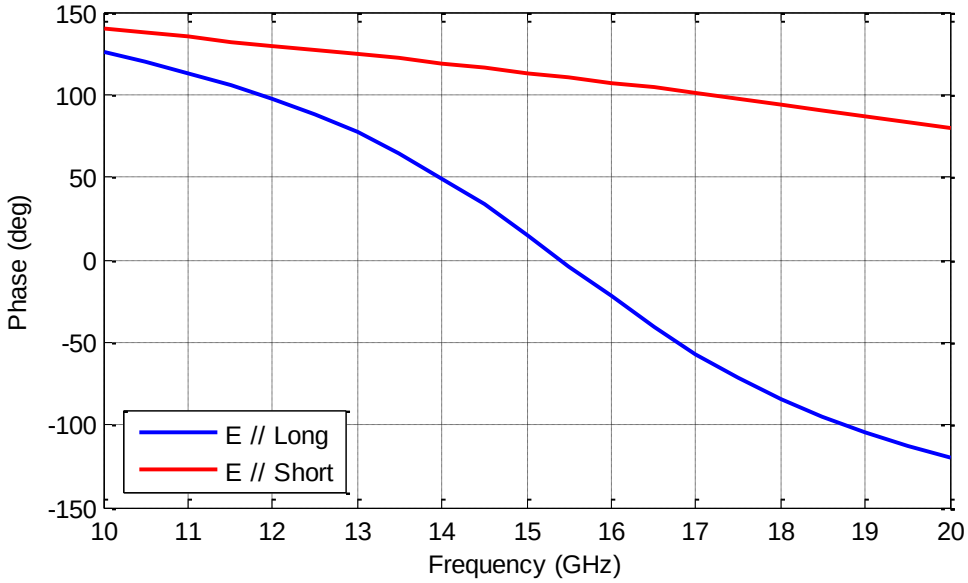

Figure 6.8: Reflection phase of unit cells. In the blue curve the electric field is parallel to the long patch dimension. The red curve has electric field parallel to the short dimension of the patch.

Surface wave propagation on each unit cell was simulated using the Eigenmode solver of HFSS. The results for the incident region unit cell are shown in Figure 6.9. For both TM and TE modes, the desired index value is one, and this represents PEC and PMC respectively. When the index is one, reflection off the front edge is minimized for both polarizations. As the index deviates from one, reflection increases. The effective

surface index can be directly related to the surface impedance [7]. The simulated TM mode has low index over a broad bandwidth. The TE mode has a cutoff at 15.2 GHz. Bound surface wave moves are not supported below this frequency, and the surface impedance is not defined. However, leaky modes are supported below cutoff, and modes in this region have effective index below one. The TE mode has an index of one at cutoff, and the index quickly rises with frequency.

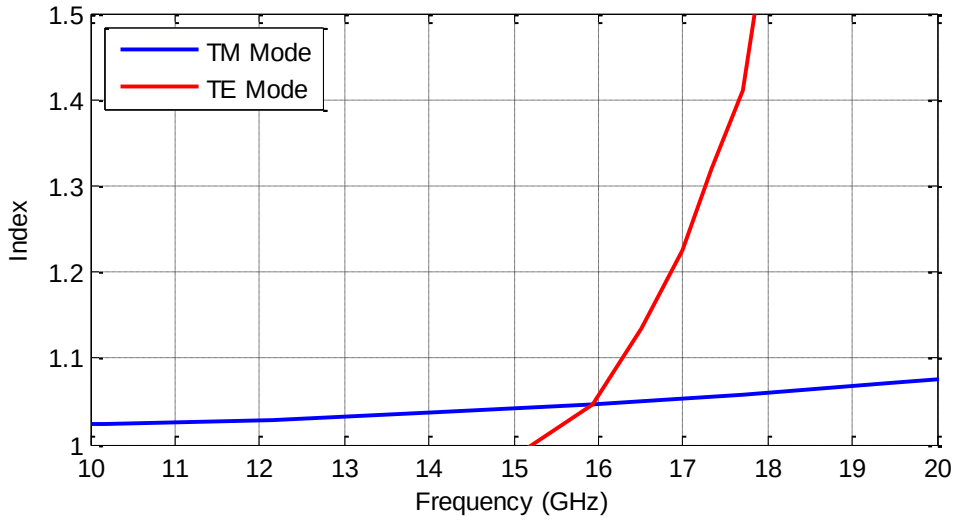

Figure 6.9: Surface index of TM and TE surface waves on incident region.

The dispersion characteristics of the transmitted-region unit cell are shown in Figure 6.10. The dispersion of both TM and TE modes are shown along with the dispersion of light in a vacuum. Bound surface waves only exist below the light line. A surface wave bandgap exists between the top of the TM mode at 11.8 GHz and the cutoff of the TE mode at 23 GHz. Surface propagation cannot occur within the bandgap, so surface waves from the incident region will be reflected from the transmitted region for both TM and TE modes. Since the boundary is angled, these reflected surface waves will not scatter back towards the source. Along with surface wave scattering, the incident plane wave scatters directly from discontinuity between the incident and transmitted regions.

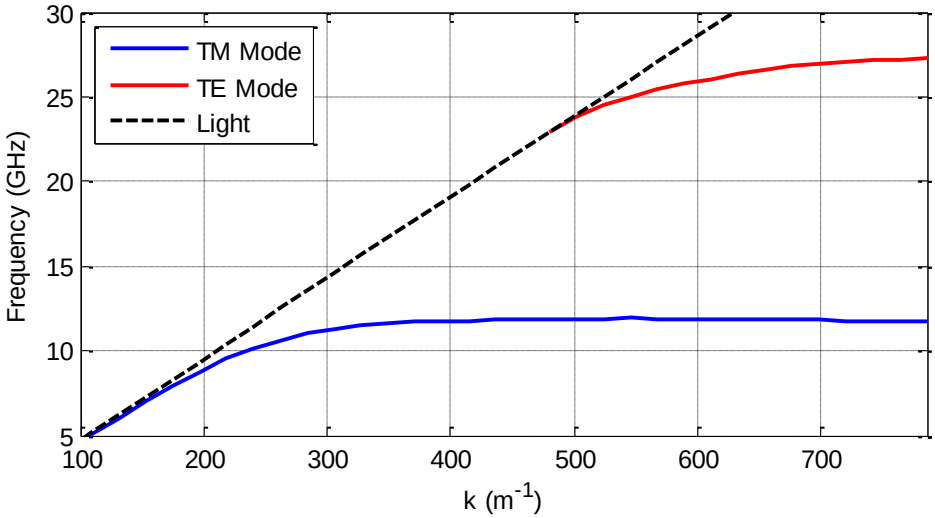

Figure 6.10: Unit cell dispersion of transmitted section.

6.4 Scattering Measurement

A surface was fabricated using the design discussed in Section 6.2 and the unit cells discussed in Section 6.3. The surface was 400×200mm (100×50 unit cells), and the angled discontinuity was at $\psi = 21.8°$. Unit cells were patterned above and below a ground plane, and the substrate was Rogers 5880 with a thickness of 1.575mm (making a total surface thickness of 3.15mm). Simulation showed that for TM incidence only the top surface of the rectangle needed to be patterned. However, for TE incidence, the surface needed to be patterned on both top and bottom in order to maximally reduce the backwards scattering. A photograph of the fabricated surface is shown in Figure 6.11.

(a)

(b)

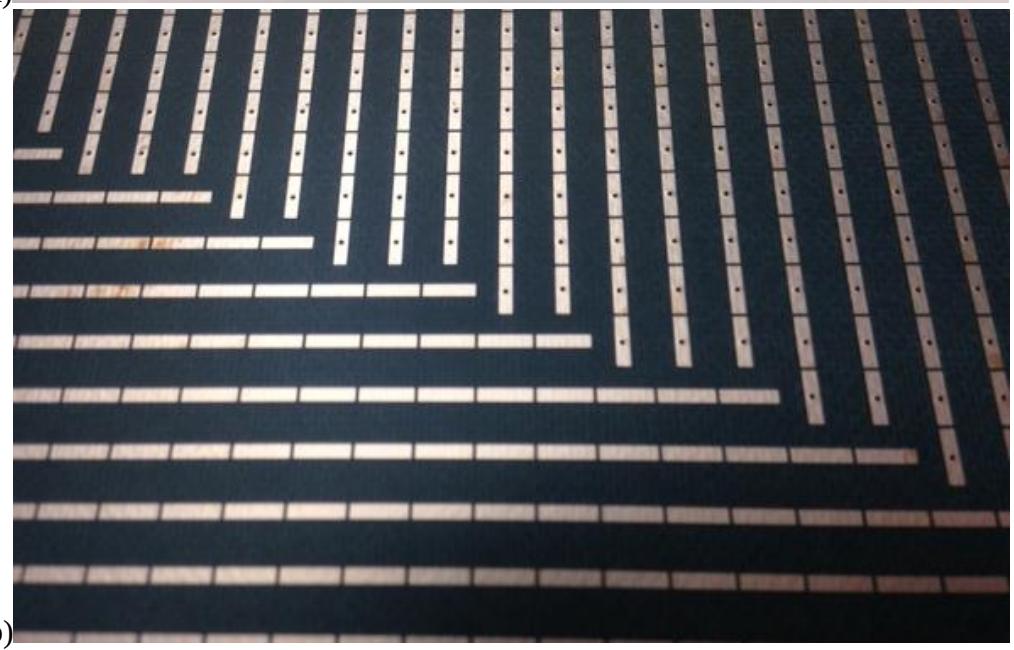

Figure 6.11: Fabricated patterned rectangular surface. (a) shows a full view of the surface and (b) shows a zoomed-in version.

The structure was measured under TM and TE illumination. Two K_U band pyramidal horns were used as sources and S21 between the horns was measured using an Agilent E5071C VNA. The operating band of each horn was 12.4-18 GHz with a TE_{10} cutoff at 9.5 GHz and a TE_{20} cutoff at 19.0 GHz. The measurement was performed in an anechoic chamber. Microwave absorbing foam was placed between the two horns in order to prevent direct coupling as seen in Figure 6.12. Without this foam, significant

coupling occurred for the TE polarization. Each horn was placed at an incident angle of $\theta = 70°$ and $\phi = 180°$. The surface was mounted on a pedestal which rotated with respect to the horns. At each rotation, the scattering transmission was measured. Note that this is a different setup from the results in Figure 6.6 where the directivity of scattered radiation was simulated using a fixed source and sample.

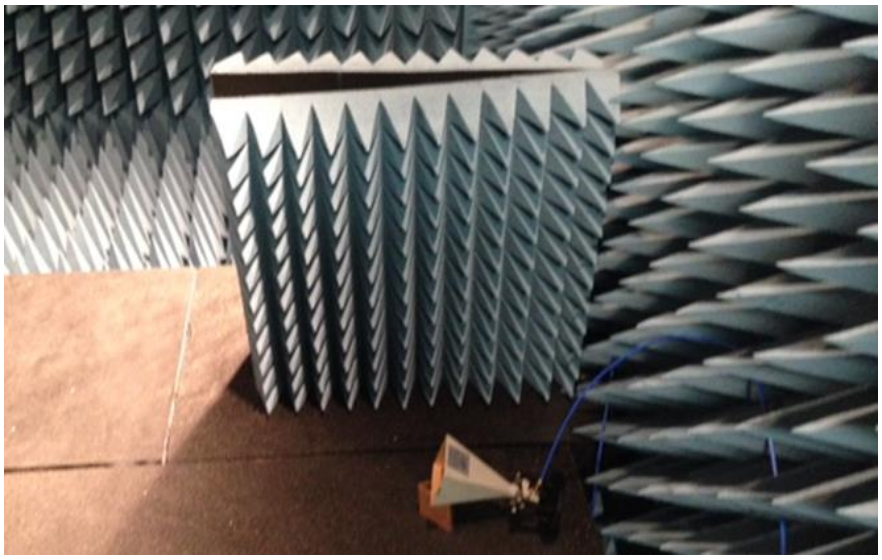

Figure 6.12: Measurement Setup. A second identical horn antenna is located on the far side of the foam barrier. The absorbing foam is used to reduce coupling between the horns.

The measured TM and TE scattering at 15 GHz is shown in Figure 6.13. For each polarization, the patterned surface is compared to a metal surface of the same dimensions, and S21 is plotted with respect to the angle of the surface. At an angle of 180°, the incident wave is normal to the surface. At this angle, the metal has large scattering for both TM and TE illumination. At all other angles the metal has low scattering (note that at angles 90° and 270° the wave is incident normally to the short side of the rectangle). For the patterned surface, both TM and TE scattering is reduced by more than 10 dB at 180°. This was the goal of the design. A new scattering peak is located at 158° due to the angled boundary, where $158° = 180° - \psi$. In Figure 6.6 the plot is of the directivity of the scattered radiation, so the peak is at $180° - 2\psi$.

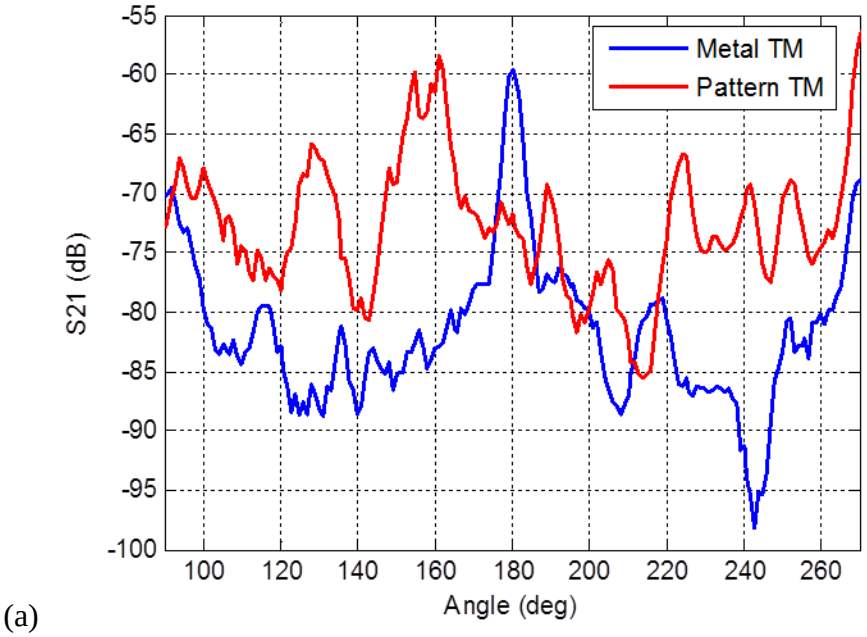

(a)

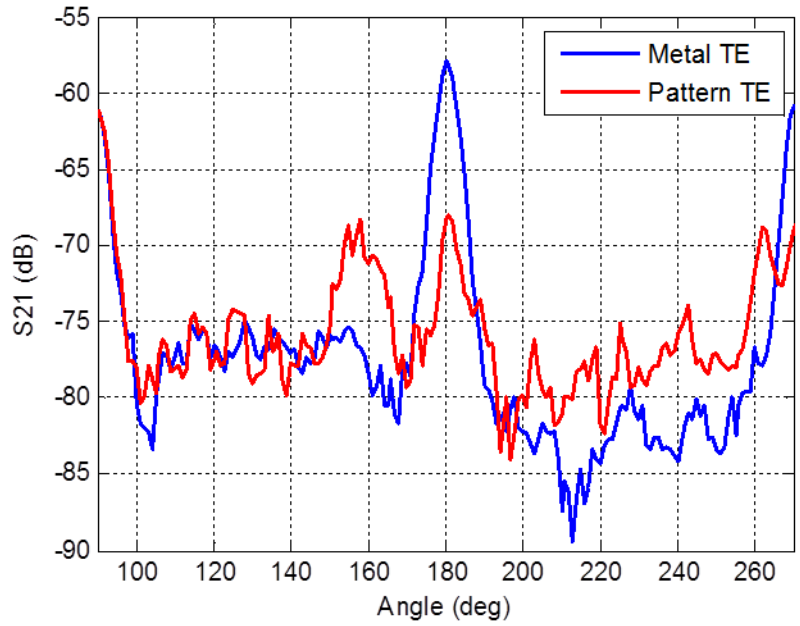

(b)

Figure 6.13: Measured scattering transmission vs. rotation angle of the surface. (a) shows the scattering for TM incidence and (b) shows the scattering for TE incidence. Only backwards scattering is shown.

For TM incidence, surface waves are supported in many directions along the surface and extra scattering peaks are generated due to reflections within the surface. For TE incidence, surface waves are only supported in the forward direction and only a single scattered peak is generated. The magnitude of the TE scattered peak is relatively lower because power is launched more strongly at other elevation angles. Measurements at a near-grazing elevation angle of $\theta = 80°$ were also performed (these results are not shown). The results were similar to the $\theta = 70°$ except the metal sheet has minimal reflection for TM incidence. This is because at grazing incidence, a metal sheet will not reflect the TM polarization at any elevation.

The transmission-reduction between the patterned and metal surfaces is shown in Figure 6.14. The vertical-axis shows the difference in S21 between the patterned surface and the metal surface in the normal-incidence orientation ($\theta = 70°$ and $\phi = 180°$). The peak reduction in scattering is around 15 GHz where reflection phase is near 180° for the PMC regions (as seen in Figure 6.8), and where the index equals one for the TE mode in the incident region (as seen in Figure 6.9). Above 19 GHz both TM and TE polarizations show increased scattering as compared to the metal surface. At 10 GHz, the reduction in TE scattering is approaching zero, while the TM mode still shows a reduction in scattering of nearly 10dB. However, as seen in Figure 6.13, a small scattered peak exists at 189° for TM illumination. At 15 GHz, this peak is more than 10 dB below the metal peak, but from 12 to 10 GHz, the peak rises to the same height as the metal peak. Accounting for this second scattering peak, the bandwidth of patterned surface is similar for TM and TE illumination. For each polarization, backwards scattering is reduced over multiple GHz around the design frequency of 15 GHz.

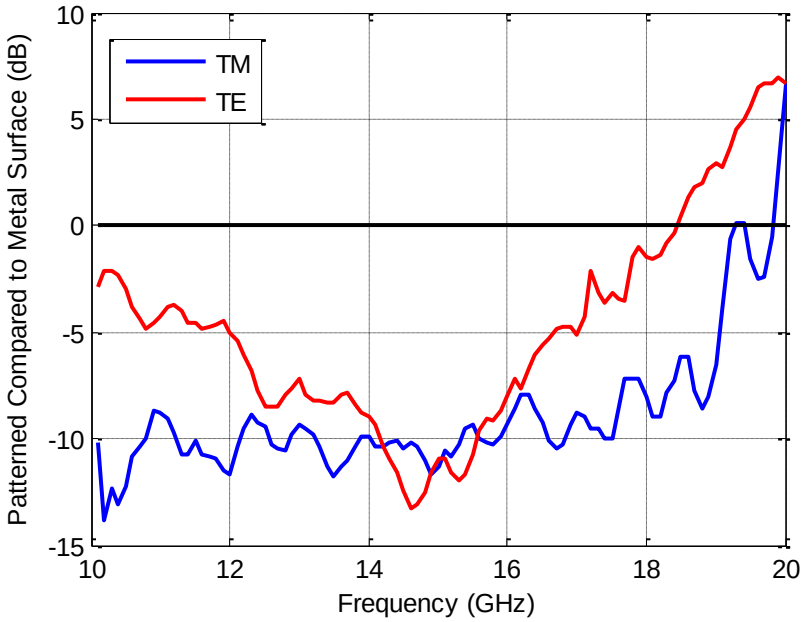

Figure 6.14: Measured reduction in backwards scattering. The scattering is the difference between the patterned surface and the metal surface.

6.5 Conclusion

A rectangular surface was patterned with anisotropic impedance surfaces in order to alter the backwards scattering as compared to a metal conductor. The effect was achieved by placing an angled boundary in the patterned surface that reflects incident waves in a different direction. The structure has two different regions on either side of the boundary. The incidence region was a hard surface and the transmitted region was a soft surface. Using reconfigurable or tunable structures, the surface could be electronically adjusted to reflect to different angles. Similarly, the frequency where the peak reduction occurs could be electronically controlled. This type of structure would allow a designer to set the scattering characteristics of the object based on the environment and adjust the characteristics dynamically.

Chapter 7 Conclusion

7.1 Summary of Work

This thesis presents an investigation into the theory and applications of anisotropic artificial impedance surfaces.

Chapter 2 reviews the fundamental properties of anisotropic impedance surfaces. The surfaces are modeled as a 2×2 boundary condition which relates the electric and magnetic fields on the surface. Periodic unit cells can be used to physically realize the surfaces, and the HFSS eigenmode simulator is used to analyze the properties. An example of rectangular and diamond unit cells are presented which show how the unit cell can be patterned to achieve a desired anisotropic tensor impedance.

Chapter 3 presents an in depth analysis of unit cell geometries. Multiple different designs are tested in order to observe the limitations of bandwidth and anistropy. A ring-mushroom unit cell gives the best performance. More generally it is shown that larger thickness and higher permittivity lead to improved performance. It is also discussed that anisotropic impedance surface must be used at frequencies where only a single mode is supported. Otherwise, modes interfere and give erroneous results.

Chapter 4 analyzes anisotropic surface impedance waveguides. It is shown that the surface can be patterned such that a confined waveguide mode is supported and propagates bound within this region. The dispersion relation of surface wave waveguides is analyzed using a ray optics method and shown to match simulation and a fabricated structure. Analysis and measurements of a curved structure and bending losses is also performed.

Chapter 5 presents a surface wave beam splitter which can reduce the surface wave scattering from an object on the surface. The beam splitter is created from two adjacent beam shifters. A cloaking structure is also shown in simulation that splits apart

the surface wave and the recombines it in phase on the far side of a cloaked region.

Chapter 6 presents a surface patterning technique that has the ability to alter the scattering properties of an object. By patterning a rectangular surface with an artificial angled boundary, the backwards scattering from the surface can be significantly reduced.

7.2 Future Work

Current impedance surface applications generally use square, rectangular, or hexagonal unit cells because they are most easily patterned together to make large shapes. However, limiting a design to a single unit cell size can significantly reduce the range of obtainable surface impedances. By patterning with continuously varying unit cell dimensions, it may be possible to more accurately achieve a desired impedance profile across a surface. This would more easily allow structures where the impedance varies gradually and continuously across the surface. In these cases, the unit cell sizes and geometries could be changed with position in order to improve the pattern. In order to perform this patterning technique, algorithms are being developed that automatically pattern unit cells based on the impedance surface.

In this thesis, each design was static and operated in a single state. For practical implementations, impedance surfaces can be made reconfigurable or tunable by using switches, varactors, tunable materials, or other methods. This would allow each design to operate over different frequency bands or in different settings. For instance, the impedance surface waveguides could be switched to connect different elements on a surface at a different time. In the same way, the beam shifter could be tuned to different frequencies depending on the source of incoming radiation. For the radar scattering surface, the angle of scattered radiation could be changed if the surface is rotated or if the source changes position. However, in any case, the cost and design challenges of an active surface are generally increased as compared to the static and passive surface presented in this thesis.

Bibliography

[1] A. M. Patel and A. Grbic, "A Printed Leaky-Wave Antenna Based on a Sinusoidally-Modulated Reactance Surface," *Antennas and Propagation, IEEE Transactions on*, vol. 59, pp. 2087-2096, 2011.

[2] G. Minatti, F. Caminita, M. Casaletti, and S. Maci, "Spiral Leaky-Wave Antennas Based on Modulated Surface Impedance," *Antennas and Propagation, IEEE Transactions on*, vol. 59, pp. 4436-4444, 2011.

[3] M. Bosiljevac, M. Casaletti, F. Caminita, Z. Sipus, and S. Maci, "Non-Uniform Metasurface Luneburg Lens Antenna Design," *Antennas and Propagation, IEEE Transactions on*, vol. 60, pp. 4065-4073, 2012.

[4] A. Dhouibi, S. N. Burokur, A. de Lustrac, and A. Priou, "Compact Metamaterial-Based Substrate-Integrated Luneburg Lens Antenna," *Antennas and Wireless Propagation Letters, IEEE*, vol. 11, pp. 1504-1507, 2012.

[5] D. Gregoire and A. Kabakian, "Surface-Wave Waveguides," *Antennas and Wireless Propagation Letters, IEEE*, vol. PP, pp. 1-1, 2011.

[6] H. J. Bilow, "Guided waves on a planar tensor impedance surface," *Antennas and Propagation, IEEE Transactions on*, vol. 51, pp. 2788-2792, 2003.

[7] B. H. Fong, J. S. Colburn, J. J. Ottusch, J. L. Visher, and D. F. Sievenpiper, "Scalar and Tensor Holographic Artificial Impedance Surfaces," *Antennas and Propagation, IEEE Transactions on*, vol. 58, pp. 3212-3221, 2010.

[8] G. Minatti, S. Maci, P. De Vita, A. Freni, and M. Sabbadini, "A Circularly-Polarized Isoflux Antenna Based on Anisotropic Metasurface," *Antennas and Propagation, IEEE Transactions on*, vol. 60, pp. 4998-5009, 2012.

[9] W. Qi, C. P. Scarborough, D. H. Werner, E. Lier, and X. Wang, "Design Synthesis of Metasurfaces for Broadband Hybrid-Mode Horn Antennas With Enhanced Radiation Pattern and Polarization Characteristics," *Antennas and Propagation, IEEE Transactions on*, vol. 60, pp. 3594-3604, 2012.

[10] W. Qi, C. P. Scarborough, B. G. Martin, R. K. Shaw, D. H. Werner, E. Lier, and

X. Wang, "A Ku-Band Dual Polarization Hybrid-Mode Horn Antenna Enabled by Printed-Circuit-Board Metasurfaces," *Antennas and Propagation, IEEE Transactions on,* vol. 61, pp. 1089-1098, 2013.

[11] P.-Y. Chen and A. Alù, "Mantle cloaking using thin patterned metasurfaces," *Physical Review B,* vol. 84, p. 205110, 11/10/ 2011.

[12] A. Monti, J. Soric, A. Alu, F. Bilotti, A. Toscano, and L. Vegni, "Overcoming Mutual Blockage Between Neighboring Dipole Antennas Using a Low-Profile Patterned Metasurface," *Antennas and Wireless Propagation Letters, IEEE,* vol. 11, pp. 1414-1417, 2012.

[13] A. Monti, F. Bilotti, A. Toscano, J. Soric, and A. Alu, "Mantle cloak devices for TE and TM polarizations," in *Antennas and Propagation Society International Symposium (APSURSI), 2013 IEEE,* 2013, pp. 324-325.

[14] R. Quarfoth and D. Sievenpiper, "Artificial Tensor Impedance Surface Waveguides," *Antennas and Propagation, IEEE Transactions on,* vol. 61, pp. 3597-3606, 2013.

[15] R. Quarfoth and D. Sievenpiper, "Anisotropic surface impedance cloak," in *Antennas and Propagation Society International Symposium (APSURSI), 2012 IEEE,* 2012, pp. 1-2.

[16] C. L. Holloway, E. F. Kuester, J. A. Gordon, J. O'Hara, J. Booth, and D. R. Smith, "An Overview of the Theory and Applications of Metasurfaces: The Two-Dimensional Equivalents of Metamaterials," *Antennas and Propagation Magazine, IEEE,* vol. 54, pp. 10-35, 2012.

[17] S. Ramo, J. R. Whinnery, and T. V. Duzer, *Fields and Waves in Communication Electronics*, Second ed. New York: John Wiley & Sons, 1984, ch 9.

[18] S. W. Lee and W. R. Jones, "Surface Waves on Two-Dimensional Corrugated Structures," *Radio Science,* vol. 6, pp. 811-818, 1971.

[19] W. Rotman, "A Study of Single-Surface Corrugated Guides," *Proceedings of the IRE,* vol. 39, pp. 952-959, 1951.

[20] R. King, D. Thiel, and K. Park, "The synthesis of surface reactance using an artificial dielectric," *Antennas and Propagation, IEEE Transactions on,* vol. 31, pp. 471-476, 1983.

[21] M. G. Silveirinha, C. A. Fernandes, and J. R. Costa, "Electromagnetic Characterization of Textured Surfaces Formed by Metallic Pins," *Antennas and Propagation, IEEE Transactions on,* vol. 56, pp. 405-415, 2008.

[22] W. L. Barnes, S. C. Kitson, T. W. Preist, and J. R. Sambles, "Photonic surfaces for surface-plasmon polaritons," *J. Opt. Soc. Am. A,* vol. 14, pp. 1654-1661, 1997.

[23] Y. Liu, T. Zentgraf, G. Bartal, and X. Zhang, "Transformational Plasmon Optics," *Nano Letters,* vol. 10, pp. 1991-1997, 2010/06/09 2010.

[24] T. Zentgraf, Y. Liu, M. H. Mikkelsen, J. Valentine, and X. Zhang, "Plasmonic Luneburg and Eaton lenses," *Nat Nano,* vol. 6, pp. 151-155, 2011.

[25] S. Tricarico, F. Bilotti, A. Alù, and L. Vegni, "Plasmonic cloaking for irregular objects with anisotropic scattering properties," *Physical Review E,* vol. 81, p. 026602, 02/18/ 2010.

[26] A. M. Patel and A. Grbic, "Modeling and Analysis of Printed-Circuit Tensor Impedance Surfaces," *Antennas and Propagation, IEEE Transactions on,* vol. 61, pp. 211-220, 2013.

[27] A. M. Patel and A. Grbic, "Effective Surface Impedance of a Printed-Circuit Tensor Impedance Surface (PCTIS)," *Microwave Theory and Techniques, IEEE Transactions on,* vol. 61, pp. 1403-1413, 2013.

[28] D. Sievenpiper, Z. Lijun, R. F. J. Broas, N. G. Alexopolous, and E. Yablonovitch, "High-impedance electromagnetic surfaces with a forbidden frequency band," *Microwave Theory and Techniques, IEEE Transactions on,* vol. 47, pp. 2059-2074, 1999.

[29] D. F. Sievenpiper, J. H. Schaffner, H. J. Song, R. Y. Loo, and G. Tangonan, "Two-dimensional beam steering using an electrically tunable impedance surface," *Antennas and Propagation, IEEE Transactions on,* vol. 51, pp. 2713-2722, 2003.

[30] C. Mias and Y. Jyh Haur, "A Varactor-Tunable High Impedance Surface With a Resistive-Lumped-Element Biasing Grid," *Antennas and Propagation, IEEE Transactions on,* vol. 55, pp. 1955-1962, 2007.

[31] C. S. R. Kaipa, A. B. Yakovlev, S. I. Maslovski, and M. G. Silveirinha, "Mushroom-Type High-Impedance Surface With Loaded Vias: Homogenization Model and Ultra-Thin Design," *Antennas and Wireless Propagation Letters, IEEE,* vol. 10, pp. 1503-1506, 2011.

[32] D. J. Hoppe and Y. Rahmat-Samii, *Impedance boundary conditions in electromagnetics*. Washington, DC: Taylor & Francis, 1995.

[33] R. Quarfoth and D. Sievenpiper, "Simulation of anisotropic artificial impedance surface with rectangular and diamond lattices," in *Antennas and Propagation*

(APSURSI), 2011 IEEE International Symposium on, 2011, pp. 1498-1501.

[34] R. A. Shelby, D. R. Smith, and S. Schultz, "Experimental Verification of a Negative Index of Refraction," *Science,* vol. 292, pp. 77-79, 2001.

[35] C. G. Parazzoli, R. B. Greegor, K. Li, B. E. C. Koltenbah, and M. Tanielian, "Experimental Verification and Simulation of Negative Index of Refraction Using Snell's Law," *Physical Review Letters,* vol. 90, p. 107401, 03/11/ 2003.

[36] G. V. Eleftheriades, A. K. Iyer, and P. C. Kremer, "Planar negative refractive index media using periodically L-C loaded transmission lines," *Microwave Theory and Techniques, IEEE Transactions on,* vol. 50, pp. 2702-2712, 2002.

[37] A. Grbic and G. V. Eleftheriades, "Experimental verification of backward-wave radiation from a negative refractive index metamaterial," *Journal of Applied Physics,* vol. 92, pp. 5930-5935, 2002.

[38] C. Caloz, A. Sanada, and T. Itoh, "A novel composite right-/left-handed coupled-line directional coupler with arbitrary coupling level and broad bandwidth," *Microwave Theory and Techniques, IEEE Transactions on,* vol. 52, pp. 980-992, 2004.

[39] T. Tamir and K. Foon, "Varieties of leaky waves and their excitation along multilayered structures," *Quantum Electronics, IEEE Journal of,* vol. 22, pp. 544-551, 1986.

[40] A. B. Yakovlev and G. W. Hanson, "Leaky-wave dispersion behavior on a grounded ferrite slab waveguide," *Microwave and Wireless Components Letters, IEEE,* vol. 12, pp. 398-400, 2002.

[41] D. F. Sievenpiper, "Forward and backward leaky wave radiation with large effective aperture from an electronically tunable textured surface," *Antennas and Propagation, IEEE Transactions on,* vol. 53, pp. 236-247, 2005.

[42] A. B. Yakovlev, M. G. Silveirinha, O. Luukkonen, C. R. Simovski, I. S. Nefedov, and S. A. Tretyakov, "Characterization of Surface-Wave and Leaky-Wave Propagation on Wire-Medium Slabs and Mushroom Structures Based on Local and Nonlocal Homogenization Models," *Microwave Theory and Techniques, IEEE Transactions on,* vol. 57, pp. 2700-2714, 2009.

[43] S. Maci, M. Caiazzo, A. Cucini, and M. Casaletti, "A pole-zero matching method for EBG surfaces composed of a dipole FSS printed on a grounded dielectric slab," *Antennas and Propagation, IEEE Transactions on,* vol. 53, pp. 70-81, 2005.

[44] A. M. Patel and A. Grbic, "The Effects of Spatial Dispersion on Power Flow

Along a Printed-Circuit Tensor Impedance Surface," *Antennas and Propagation, IEEE Transactions on,* vol. 62, pp. 1464-1469, 2014.

[45] M. C. Simon, "Ray tracing formulas for monoaxial optical components," *Appl. Opt.,* vol. 22, pp. 354-360, 1983.

[46] Q.-T. Liang, "Simple ray tracing formulas for uniaxial optical crystals," *Appl. Opt.,* vol. 29, pp. 1008-1010, 1990.

[47] W.-Q. Zhang, "General ray-tracing formulas for crystal," *Appl. Opt.,* vol. 31, pp. 7328-7331, 1992.

[48] M. Sluijter, "Ray-optics analysis of inhomogenous optically anisotropic media," Ph.D., TNW Optics Research Group, Delft University of Technology, Koninklijke Philips Electronics N.V., 2010.

[49] B. E. A. Saleh and M. C. Teich, *Fundamentals of photonics*. New York: Wiley, 1991.

[50] Y. Satomura, M. Matsuhara, and N. Kumagai, "Analysis of Electromagnetic-Wave Modes in Anisotropic Slab Waveguide," *Microwave Theory and Techniques, IEEE Transactions on,* vol. 22, pp. 86-92, 1974.

[51] S. R. Seshadri, "Ray model for a planar anisotropic dielectric waveguide," *J. Opt. Soc. Am. A,* vol. 15, pp. 972-977, 1998.

[52] R. Quarfoth and D. Sievenpiper, "Broadband Unit Cell Design for Highly-Anisotropic Impedance Surfaces," *Antennas and Propagation, IEEE Transactions on,* vol. PP, pp. 1-1, 2014.

[53] E. A. J. Marcatili, "Bends in Optical Dielectric Guides," *Bell System Technical Journal,* vol. 48, pp. 2103-2132, 1969.

[54] A. W. Snyder, "Generalised Fresnel's law for loss due to curvature," *Electronics Letters,* vol. 9, pp. 609-610, 1973.

[55] A. W. Snyder and D. J. Mitchell, "Bending losses of multimode optical fibres," *Electronics Letters,* vol. 10, pp. 11-12, 1974.

[56] A. W. Snyder and J. Love, *Optical waveguide theory* vol. 190: Springer, 1983.

[57] M. Remouche, R. Mokdad, A. Chakari, and P. Meyrueis, "Intrinsic integrated optical temperature sensor based on waveguide bend loss," *Optics & Laser Technology,* vol. 39, pp. 1454-1460, 10// 2007.

[58] J. B. Pendry, D. Schurig, and D. R. Smith, "Controlling Electromagnetic Fields,"

Science, vol. 312, pp. 1780-1782, 2006.

[59] D. Schurig, J. J. Mock, B. J. Justice, S. A. Cummer, J. B. Pendry, A. F. Starr, and D. R. Smith, "Metamaterial Electromagnetic Cloak at Microwave Frequencies," *Science*, vol. 314, pp. 977-980, 2006.

[60] M. Rahm, S. A. Cummer, D. Schurig, J. B. Pendry, and D. R. Smith, "Optical Design of Reflectionless Complex Media by Finite Embedded Coordinate Transformations," *Physical Review Letters*, vol. 100, p. 063903, 2008.

[61] P. A. Huidobro, M. L. Nesterov, L. Martín-Moreno, and F. J. García-Vidal, "Transformation Optics for Plasmonics," *Nano Letters*, vol. 10, pp. 1985-1990, 2010/06/09 2010.

[62] H. Chen and C. T. Chan, "Electromagnetic wave manipulation by layered systems using the transformation media concept," *Physical Review B*, vol. 78, p. 054204, 2008.

[63] G. Gok and A. Grbic, "A Printed Beam-Shifting Slab Designed Using Tensor Transmission-Line Metamaterials," *Antennas and Propagation, IEEE Transactions on*, vol. 61, pp. 728-734, 2013.

[64] O. Siddiqui and G. V. Eleftheriades, "Resonance-cone focusing in a compensating bilayer of continuous hyperbolic microstrip grids," *Applied Physics Letters*, vol. 85, pp. 1292-1294, 2004.

[65] M. Selvanayagam and G. V. Eleftheriades, "Experimental Verification of the Effective Medium Properties of a Transmission-Line Metamaterial on a Skewed Lattice," *Antennas and Wireless Propagation Letters, IEEE*, vol. 10, pp. 1495-1498, 2011.

[66] A. M. Patel and A. Grbic, "Transformation Electromagnetics Devices Based on Printed-Circuit Tensor Impedance Surfaces," *Microwave Theory and Techniques, IEEE Transactions on*, vol. 62, pp. 1102-1111, 2014.

[67] R. Quarfoth and D. Sievenpiper, "Unit Cell for Highly-Anisotropic Tensor Impedance Surface," *Transactions on Antennas and Propagation*, vol. Accepted for Publication, 2014.

[68] U. Leonhardt, "Optical Conformal Mapping," *Science*, vol. 312, pp. 1777-1780, 2006.

[69] B. Kanté, D. Germain, and A. de Lustrac, "Experimental demonstration of a nonmagnetic metamaterial cloak at microwave frequencies," *Physical Review B*, vol. 80, p. 201104, 11/17/ 2009.

[70] H. Chen and C. T. Chan, "Transformation media that rotate electromagnetic fields," *Applied Physics Letters,* vol. 90, pp. -, 2007.

[71] J. Hao, Y. Yuan, L. Ran, T. Jiang, J. A. Kong, C. T. Chan, and L. Zhou, "Manipulating Electromagnetic Wave Polarizations by Anisotropic Metamaterials," *Physical Review Letters,* vol. 99, p. 063908, 08/10/ 2007.

[72] J. C. Soric, P. Y. Chen, A. Kerkhoff, D. Rainwater, K. Melin, and A. Alù, "Demonstration of an ultralow profile cloak for scattering suppression of a finite-length rod in free space," *New Journal of Physics,* vol. 15, p. 033037, 2013.

[73] J. S. Colburn, D. F. Sievenpiper, B. H. Fong, J. J. Ottusch, J. L. Visher, and P. R. Herz, "Advances in Artificial Impedance Surface Conformal Antennas," in *Antennas and Propagation Society International Symposium, 2007 IEEE*, 2007, pp. 3820-3823.

[74] D. J. Gregoire, "3-D Conformal Metasurfaces," *Antennas and Wireless Propagation Letters, IEEE,* vol. 12, pp. 233-236, 2013.

[75] G. Pelosi, G. Manara, and P. Nepa, "A UTD solution for the scattering by a wedge with anisotropic impedance faces: skew incidence case," *Antennas and Propagation, IEEE Transactions on,* vol. 46, pp. 579-588, 1998.

[76] G. Pelosi, G. Manara, and M. Fallai, "Physical optics expressions for the fields scattered from anisotropic impedance flat plates," *Microwave and Optical Technology Letters,* vol. 14, pp. 316-318, 1997.

[77] H. J. Bilow, "Scattering by an infinite wedge with tensor impedance boundary conditions-a moment method/physical optics solution for the currents," *Antennas and Propagation, IEEE Transactions on,* vol. 39, pp. 767-773, 1991.

[78] H. Ming, Y. Shiwen, G. Fei, R. Quarfoth, and D. Sievenpiper, "A 2-D Multibeam Half Maxwell Fish-Eye Lens Antenna Using High Impedance Surfaces," *Antennas and Wireless Propagation Letters, IEEE,* vol. 13, pp. 365-368, 2014.

[79] R. Quarfoth and D. Sievenpiper, "Surface Wave Scattering Reduction Using Beam Shifters," *Antennas and Wireless Propagation Letters, IEEE,* vol. 13, pp. 963-966, 2014.

[80] D. Gregoire and A. Kabakian, "Surface-Wave Waveguides," *Antennas and Wireless Propagation Letters, IEEE,* vol. 10, pp. 1512-1515, 2011.

[81] P. S. Kildal, "Definition of artificially soft and hard surfaces for electromagnetic waves," *Electronics Letters,* vol. 24, pp. 168-170, 1988.

[82] P. S. Kildal, "Artificially soft and hard surfaces in electromagnetics," *Antennas and Propagation, IEEE Transactions on*, vol. 38, pp. 1537-1544, 1990.

[83] P. S. Kildal, A. A. Kishk, and A. Tengs, "Reduction of forward scattering from cylindrical objects using hard surfaces," *Antennas and Propagation, IEEE Transactions on*, vol. 44, pp. 1509-1520, 1996.

[84] G. Manara, P. Nepa, and G. Pelosi, "High-frequency EM scattering by edges in artificially hard and soft surfaces illuminated at oblique incidence," *Antennas and Propagation, IEEE Transactions on*, vol. 48, pp. 790-800, 2000.

[85] M. Paquay, J. C. Iriarte, I. Ederra, R. Gonzalo, and P. de Maagt, "Thin AMC Structure for Radar Cross-Section Reduction," *Antennas and Propagation, IEEE Transactions on*, vol. 55, pp. 3630-3638, 2007.

[86] S. Maci and P. S. Kildal, "Hard and soft surfaces realized by FSS printed on a grounded dielectric slab," in *Antennas and Propagation Society International Symposium, 2004. IEEE*, 2004, pp. 285-288 Vol.1.